

©Copyright 2021

Sarthak Piyushkumar Jariwala

# Structure-Property Relationships in Organic-Inorganic Halide Perovskite Solar Cells

Sarthak Piyushkumar Jariwala

A dissertation

submitted in partial fulfillment of the  
requirements for the degree of

Doctor of Philosophy

University of Washington

2021

Reading Committee:

David S. Ginger, Chair

John Devin Mackenzie

Peter J. Pauzauskie

Program Authorized to Offer Degree:

Materials Science and Engineering

University of Washington

**Abstract**

Structure-Property Relationships in Organic-Inorganic Halide Perovskite Solar Cells

Sarthak Piyushkumar Jariwala

Chair of the Supervisory Committee:

Professor David S. Ginger

Department of Chemistry

Over the past 100 years, there has been a complete disregard for the environmental impact of unregulated burning of fossil fuels. This has led to an increase in the greenhouse gas emissions, atmospheric CO<sub>2</sub>, global temperature, and sea levels, leading to an unprecedented challenge of climate change and air pollution for our planet. To counteract these changes and achieve net-zero emissions target set by the Paris climate agreement, decarbonizing electricity generation is of utmost importance. Solar energy is one of the most abundant sources of energy on Earth and harnessing it contributes to less than 1/10<sup>th</sup> the CO<sub>2</sub> per kWh compared to fossil fuels. Therefore, solar energy will have to play a critical role in meeting the increasing energy demands. Promisingly, the cost of solar has drastically reduced by 10x over the last decade. To accelerate the solar deployment at a terra-watt scale (required to meet the growing energy demands); efficient, cheap and scalable solar energy is important. Halide perovskite solar cells

serve as a complementary technology to existing commercial solar cell technology such as Si, CdTe, CIGS, etc. to meet the growing energy demands. Their cheap and scalable deposition along with high power conversion efficiencies make them an ideal candidate for wide scale deployment. Over the past 12 years, perovskite solar cells have demonstrated rapid progress in their power conversion efficiencies (PCE) with current record PCE at 25.5%. However, the PCEs are still further away from theoretically achievable efficiencies. This investigates the reasons behind the current performance limitations. We identify that the microstructure has a significant effect on the performance of halide perovskite solar cells. Specifically, we identify non-radiative recombination occurring at the grain boundaries, within grains, and at the surfaces and interfaces as the primary performance limiters.

Firstly, we investigate the conflicting literature on the nature of grain boundaries and their impact on the performance of the halide perovskite solar cells. This has primarily emerged due to misidentification of grains and grain boundaries in halide perovskites. Prior to our work, the most common method for identifying grains and grain boundaries in halide perovskite literature was scanning electron microscopy (SEM). Using electron back scatter diffraction (EBSD), we demonstrate that using SEM leads to misidentification and overestimation of grain boundaries. Using EBSD, we also reveal grain structure and internal misorientation that is otherwise hidden. We report the presence of local crystal misorientation which is consistent with the presence of local strain that varies from one grain to the next. Using co-aligned confocal optical photoluminescence (PL) microscopy images on the same halide perovskite samples used for EBSD, we show that PL is anticorrelated with the local grain orientation spread. This suggests that grains with higher degrees of crystalline orientational heterogeneity (local strain) exhibit more non-radiative recombination. We also find that larger grains tend to have larger

grain orientation spread, consistent with higher degrees of strain and non-radiative recombination.

Next, we investigate the chemical impact of large A-site cation, such as dimethyl ammonium (DMA), on the metal halide perovskites. Large A-site cations have demonstrated significant improvements in the performance and long-term operational stability of the resulting perovskite solar cells. However, the chemical impact of adding large A-site cations is largely unknown. We use time-of-flight secondary-ion mass spectrometry (TOF-SIMS) to demonstrate that DMA is indeed incorporated in the film. We also demonstrate that there is a higher concentration of DMA at the surface compared to bulk of the film. Furthermore, using a combination of PL microscopy and photo-induced force microscopy (PiFM), we also demonstrate that incorporating DMA in the film leads to higher local spectral and chemical heterogeneity, compared to the control films. Lastly, we show that the spatial chemical composition variations arise primarily due to DMA incorporation and not due to higher Cs concentration in the DMA films. These results illustrate that while DMA incorporation is beneficial to operational stability and device performance, there is still room for process optimization to achieve local compositional homogeneity and further improve the device performance and operational stability.

Lastly, we control the surface recombination in the mixed-cation, mixed-halide perovskites, by passivating non-radiative defects with the polymerizable Lewis base (3-aminopropyl)trimethoxysilane (APTMS). We demonstrate average minority carrier lifetimes  $> 4$   $\mu\text{s}$  and high external photoluminescence quantum efficiencies ( $>20\%$ , corresponding to  $\sim 97\%$  of the maximum theoretical quasi-Fermi-level splitting) at low excitation fluence, a record for non-methylammonium based mixed-cation, mixed-halide perovskites. We extend the APTMS surface

passivation to higher bandgap double cation (Formamidinium, Cesium) compositions (1.7 eV, 1.75 eV and 1.8 eV) relevant for multijunction solar cells. Lastly, we demonstrate that the average surface recombination velocity (SRV) decreases from  $\sim 1000$  cm/s to  $\sim 10$  cm/s post APTMS passivation. These results demonstrate that surface-mediated recombination is the primary non-radiative loss pathway in many MA-free mixed-cation mixed-halide films with a range of different bandgaps, which is a problem observed for a wide range of perovskite active layers and reactive electrical contacts. Our study also provides insights to develop passivating molecules that help reduce surface recombination in methylammonium-free mixed-cation mixed-halide films and indicates that surface passivation and contact engineering will enable near-theoretical device efficiencies with these materials.

# TABLE OF CONTENTS

<i>List of Figures</i> .....	9
<i>Chapter 1. Introduction</i> .....	10
1.1. What are halide perovskites? .....	10
1.2. Halide perovskites as solar cells .....	11
References .....	12
<i>Chapter 2. Local Crystal Misorientation Influences Non-Radiative Recombination</i> .....	13
2.1. Overview .....	13
2.2. Introduction .....	13
2.3. Morphology and local crystal orientation measurements .....	15
2.4. Imaging the local orientation heterogeneity, grains and grain boundaries.....	16
2.5. Sub-grain boundaries and intra-grain misorientation .....	18
2.6. Correlation between local luminescence, orientation heterogeneity and grain area .....	21
2.7. Conclusion.....	23
Acknowledgements .....	24
References .....	24
<i>Chapter 3. Impact of Dimethylammonium on Local Chemical Composition in Halide Perovskites</i> .....	30
3.1. Overview .....	30
3.2. Introduction .....	30
3.3. Time-of-flight secondary-ion-mass spectrometry.....	31
3.4. Photoluminescence Microscopy .....	33
3.5. Photo-induced Force Microscopy .....	34
3.6. Conclusion.....	35
Acknowledgements .....	36
References .....	36
<i>Chapter 4. Reducing Surface Recombination Velocity of MA-free Mixed Cation Mixed Halide Perovskites via Surface Passivation</i> .....	41
4.1. Overview .....	41
4.2. Introduction .....	41
4.3. Surface passivation beyond MA based halide perovskites .....	43
4.4. Surface passivation for different bandgap MA-free perovskite .....	46
4.5. High resolution and angle-resolved X-ray photoelectron spectroscopy.....	47

<b>4.6. Surface recombination velocity (SRV)</b> .....	<b>49</b>
<b>4.7. Conclusion</b> .....	<b>51</b>
<b>Acknowledgements</b> .....	<b>52</b>
<b>References</b> .....	<b>52</b>
<i>Appendix A: Supplementary Information for Chapter 2</i> .....	<b>60</b>
<i>Appendix B: Supplementary Information for Chapter 3</i> .....	<b>81</b>
<i>Appendix C: Supplementary Information for Chapter 4</i> .....	<b>96</b>
<b>Curriculum Vitae</b> .....	<b>122</b>

## List of Figures

Figure 1.1. Schematic of halide perovskite unit cell structure showing A site occupied by methylammonium, B site occupied by lead, and X site occupied by Iodine. ....	10
Figure 2.1. Morphology and local crystal orientation measurements of CH <sub>3</sub> NH <sub>3</sub> PbI <sub>3</sub> thin films. ....	16
Figure 2.2. Imaging the local orientation heterogeneity, grains and grain boundaries in CH <sub>3</sub> NH <sub>3</sub> PbI <sub>3</sub> thin films using electron back scatter diffraction (EBSD). ....	17
Figure 2.3. Sub-grain boundaries and intra-grain misorientation. ....	19
Figure 2.4. Correlation between local luminescence, orientation heterogeneity and grain area in CH <sub>3</sub> NH <sub>3</sub> PbI <sub>3</sub> . ....	21
Figure 3.1. TOF-SIMS analysis of DMA10, Ctrl 67/33, and Ctrl 80/20. ....	32
Figure 3.2. Local PL spectral scans of (a) DMA10, (b) Ctrl 80/20, and (c) Ctrl 67/33 thin films. ....	33
Figure 3.3. Photo-induced force microscopy (PiFM) of DMA10 thin films. ....	34
Figure 4.1 – Surface passivation beyond MA based halide perovskites. ....	44
Figure 4.2- Surface passivation for different bandgap MA-free perovskite compositions and triple cation compositions. ....	46
Figure 4.3 - High resolution and angle-resolved X-ray photoelectron spectroscopy (XPS). ....	47
Figure 4.4 – Surface recombination velocity (SRV) extracted from the PL lifetime data on Cs <sub>17</sub> Br <sub>15</sub> films as discussed in the text. ....	49

# Chapter 1. Introduction

## 1.1. What are halide perovskites?

Perovskite is a crystal structure that make up a class of materials that have the molecular formula  $ABX_3$  and a network of  $BX_6$  corner sharing octahedra.<sup>1</sup> They have been widely investigated for various applications since their discovery in 1839 by Gustav Rose.<sup>1</sup> Recently, a group of perovskites called halide perovskites have garnered a lot of attention, primarily due to their optoelectronic properties.<sup>2-5</sup>

In halide perovskites, the A site is occupied by a monovalent cation (organic or inorganic), the B site is occupied by a divalent cation (Pb or Sn) and the X site is occupied by a halide (generally I, Br or Cl). Figure 1.1 shows the schematic of a halide perovskite unit cell. The figure shows the structure of a prototypical halide perovskite – methylammonium lead triiodide, where the A site is occupied by methylammonium organic cation, B site is occupied by lead and the X site is occupied by iodine.

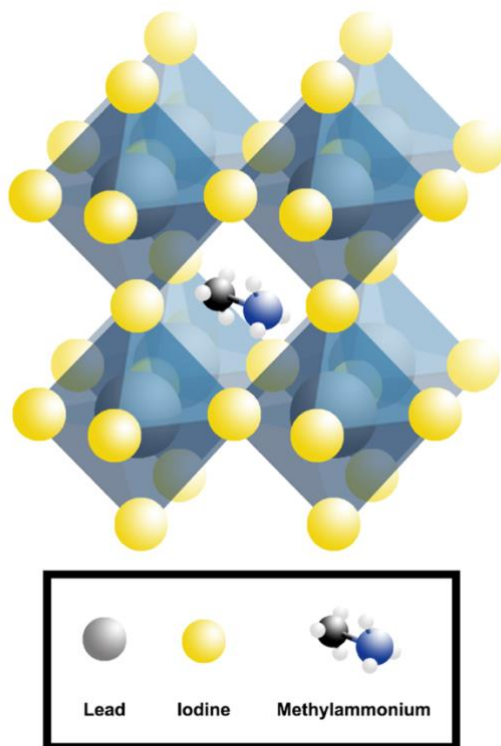


**Figure 1.1. Schematic of halide perovskite unit cell structure showing A site occupied by methylammonium, B site occupied by lead, and X site occupied by Iodine.**

## 1.2. Halide perovskites as solar cells

One of the reasons halide perovskites have garnered a lot of scientific attention is due to their remarkable optoelectronic properties. Halide perovskites have high absorption coefficients, long carrier diffusion lengths, high carrier lifetimes and mobilities, and tunable bandgap.<sup>2-4,6</sup>

In addition to the remarkable optoelectronic properties, they are also relatively easier to process. They can be deposited from a solution ink on various different substrates (rigid and flexible) as well as using various different processing conditions – spin coating, evaporation, roll-to-roll printing, etc.<sup>7,8</sup>

The combination of excellent optoelectronic properties and easy processing conditions make halide perovskites an ideal candidate for solar cell applications. The optoelectronic properties lead to a high performing solar cell and the easy processing conditions lead to lower cost of fabrication compared to current commercial counter parts. As such, halide perovskites have been investigated extensively for applications in solar cells, leading to rapid improvements in power conversion efficiencies (PCE) from 3.8% to 25.5% within a span of ~12 years.<sup>9</sup>

Due to their bandgap tunability,<sup>5,6</sup> halide perovskites can also be used in multi-junction solar cells with Silicon, CIGS and other perovskite solar cells.<sup>5</sup> Multi-junction solar cells allow for more efficient absorption of different parts of the incoming solar radiation.<sup>5</sup> The current PCE record for the Si/perovskite multi-junction solar cell is 29.5%, surpassing the crystalline Si single junction PCE.<sup>9</sup>

These PCEs for single and multi-junction perovskite solar cells are remarkable for a material that is polycrystalline, and solution processed at relatively low temperatures<sup>10</sup> (~100-150°C) compared to other high performing solar cell technologies such as Si and GaAs. However, the PCEs for both single and multi-junction perovskite solar cells are still further away from their theoretical maximum limits, ~33% for a single junction perovskite solar cell with a bandgap of ~1.4 eV and ~43% for multi-junction solar cells.<sup>5</sup>

This thesis aims to identify and address the various sources of non-radiative recombination that lead to performance bottlenecks in halide perovskite solar cells. Specifically, this thesis investigates and discusses the impact of local microstructure on the properties in halide perovskites. This thesis also proposes new ways for modifying the surfaces and interfaces to improve the performance. Lastly, in addition to the understanding, this thesis also proposes methods for a more rational design of halide perovskites, especially helpful for scaling up halide perovskite solar cell deposition.

## References

- (1) Akkerman, Q. A.; Manna, L. What Defines a Halide Perovskite? *ACS Energy Letters*. American Chemical Society 2020, pp 604–610. <https://doi.org/10.1021/acsenenergylett.0c00039>.
- (2) Stranks, S. D.; Snaith, H. J. Metal-Halide Perovskites for Photovoltaic and Light-Emitting Devices. *Nat. Nanotechnol.* **2015**, *10* (5), 391–402. <https://doi.org/10.1038/nnano.2015.90>.
- (3) Brenes, R.; Guo, D.; Osherov, A.; Noel, N. K.; Eames, C.; Hutter, E. M.; Pathak, S. K.; Niroui, F.; Friend, R. H.; Islam, M. S.; et al. Metal Halide Perovskite Polycrystalline Films Exhibiting Properties of Single Crystals. *Joule* **2017**, *1* (1), 155–167. <https://doi.org/10.1016/j.joule.2017.08.006>.
- (4) deQuilettes, D. W.; Koch, S.; Burke, S.; Paranj, R.; Shropshire, A. J.; Ziffer, M. E.; Ginger, D. S. Photoluminescence Lifetimes Exceeding 8 Ms and Quantum Yields Exceeding 30% in Hybrid Perovskite Thin Films by Ligand Passivation. *ACS Energy Lett.* **2016**, *1* (2), 438–444. <https://doi.org/10.1021/acsenenergylett.6b00236>.
- (5) Eperon, G. E.; Hörantner, M. T.; Snaith, H. J. Metal Halide Perovskite Tandem and Multiple-Junction Photovoltaics. *Nat. Rev. Chem.* **2017**, *1*, 0095. <https://doi.org/10.1038/s41570-017-0095>.
- (6) McMeekin, D. P.; Sadoughi, G.; Rehman, W.; Eperon, G. E.; Saliba, M.; Horantner, M. T.; Haghighirad, A.; Sakai, N.; Korte, L.; Rech, B.; et al. A Mixed-Cation Lead Mixed-Halide Perovskite Absorber for Tandem Solar Cells. *Science (80-. )*. **2016**, *351* (6269), 151–155. <https://doi.org/10.1126/science.aad5845>.
- (7) Dou, B.; Whitaker, J. B.; Bruening, K.; Moore, D. T.; Wheeler, L. M.; Ryter, J.; Breslin, N. J.; Berry, J. J.; Garner, S. M.; Barnes, F. S.; et al. Roll-to-Roll Printing of Perovskite Solar Cells. *ACS Energy Lett.* **2018**, *3* (10), 2558–2565. <https://doi.org/10.1021/acsenenergylett.8b01556>.
- (8) Park, N. G.; Zhu, K. Scalable Fabrication and Coating Methods for Perovskite Solar Cells and Solar Modules. *Nature Reviews Materials*. Nature Research May 1, 2020, pp 333–350. <https://doi.org/10.1038/s41578-019-0176-2>.
- (9) National Renewable Energy Laboratory Efficiency Chart 2020 <https://www.nrel.gov/pv/assets/pdfs/best-research-cell-efficiencies.20200406.pdf> (accessed Apr 24, 2020).
- (10) Zhang, W.; Saliba, M.; Moore, D. T.; Pathak, S. K.; Hörantner, M. T.; Stergiopoulos, T.; Stranks, S. D.; Eperon, G. E.; Alexander-Webber, J. A.; Abate, A.; et al. Ultrasoother Organic-Inorganic Perovskite Thin-Film Formation and Crystallization for Efficient Planar Heterojunction Solar Cells. *Nat. Commun.* **2015**, *6*. <https://doi.org/10.1038/ncomms7142>.

# Chapter 2. Local Crystal Misorientation Influences Non-Radiative Recombination

*Adapted with permission from Sarthak Jariwala, Hongyu Sun, Gede W. P. Adhyaksa, Andries Lof, Loreta A. Muscarella, Bruno Ehrler, Erik C. Garnett, David S. Ginger. "Local Crystal Misorientation Influences Non-Radiative Recombination in Halide Perovskites" Joule 2019. DOI-10.1016/j.joule.2019.09.001.*

## 2.1. Overview

We use ultrasensitive electron backscatter diffraction (EBSD) to map the local crystal orientations, grains, and grain boundaries in  $\text{CH}_3\text{NH}_3\text{PbI}_3$  (MAPI) perovskite thin films. Although the true grain structure is broadly consistent with the morphology visible in scanning electron microscopy (SEM), the inverse pole figure maps taken with EBSD reveal grain structure and internal misorientation that is otherwise hidden. Local crystal misorientation is consistent with the presence of local strain which varies from one grain to the next. We acquire co-aligned confocal optical photoluminescence (PL) microscopy images on the same MAPI samples used for EBSD. We correlate optical and EBSD data, showing that PL is anticorrelated with the local grain orientation spread, suggesting that grains with higher degrees of crystalline orientational heterogeneity (local strain) exhibit more non-radiative recombination. We find that larger grains tend to have larger grain orientation spread, consistent with higher degrees of strain and non-radiative recombination.

## 2.2. Introduction

Halide perovskite-based solar cells have experienced rapid gains in power conversion efficiency (PCE), with the current PCE record at 23.7% for single junction and 28% for Si-perovskite tandems.<sup>1</sup> Despite such high PCE for a material that is solution processed, the values are still well-below their realistically achievable PCE limits ( $\sim 30\%$  for single junction  $\text{CH}_3\text{NH}_3\text{PbI}_3$ <sup>2</sup> and  $\sim 32\%$  for two terminal Si-perovskite tandems<sup>3</sup>). Non-radiative recombination, both in the film<sup>4-7</sup> and at the interfaces,<sup>8,9</sup> remains a major barrier to approach the radiative efficiency limits in halide perovskites. Our group has recently demonstrated that with surface passivation halide perovskites can achieve over 90% internal photoluminescence quantum efficiency (PLQE) and a quasi-Fermi level splitting approaching 97% of the radiative efficiency limit.<sup>4,8</sup> These results put halide perovskites alongside GaAs as one of the most radiatively efficient semiconductors.<sup>10</sup> However, intrinsic films (without surface passivation) have a significant source of non-radiative recombination (with internal PLQE  $\sim 10\%$ ).<sup>4</sup> A significant portion of this non-radiative recombination is thought to occur at under-passivated surfaces and grain boundaries.<sup>4-6,11-13</sup>

Unfortunately, the casual conflation of grain boundaries with morphological structures in halide perovskites has generated confusion about the nature of grain boundaries.<sup>14,15</sup> This situation

has arisen because, currently, one of the most-used techniques to identify grains and grain boundaries in the halide perovskite community is scanning electron microscopy (SEM). However, while SEM provides information about the morphology of the film, conventional SEM does not provide any crystallographic information about the material. The crystallographic information is critical in the case of halide perovskites because domains as observed in the SEM may not accurately represent the grains and grain boundary terminations, leading to an overestimation of grain sizes.<sup>16</sup> Indeed, frustration with this topic has caused a leading solar cell researcher to tweet out “SEM does not obvious[ly] [provide] information about ‘grain size’ or ‘grain orientation’ for metal halide perovskite active layers”.<sup>17</sup>

Traditionally, grain sizes, grain boundaries, and local crystal orientations in thin-film materials are mapped using electron backscatter diffraction (EBSD). However, this method has been notoriously difficult to apply to the halide perovskites most relevant for photovoltaics applications due to beam-induced damage.<sup>16,18,19</sup> Compared to SEM imaging, EBSD requires higher doses (higher current and/or longer integration time) to acquire sufficient contrast in the Kikuchi diffraction lines generated from backscattered electrons.<sup>16</sup> Therefore, the use of traditional EBSD detectors leads to significant beam-induced damage when characterizing halide perovskite solar cell materials.<sup>16</sup> Recently, Leonhard *et al.* reported that using low-vacuum mode with water pressures of 0.1-1 mbar in the sample chamber can minimize beam-induced damage and prevent surface charging due to ionization of the water molecules by the electrons during EBSD.<sup>20</sup> Some of us recently demonstrated the potential for a new solid-state EBSD detector to enable EBSD maps with high sensitivity, fast readout and without appreciable beam damage to the crystal structure.<sup>21</sup>

Understanding grain orientation and grain boundary properties has been critical to the development of many photovoltaic semiconductor technologies such as CdTe, GaAs, Cu(In<sub>1-x</sub>Ga<sub>x</sub>)Se<sub>2</sub>, multicrystalline Si, and InP.<sup>22-29</sup> However, the role of grain orientation and grain boundary properties in halide perovskite semiconductors has remained poorly understood<sup>30</sup> despite the local optoelectronic heterogeneity observed at the microscale in these materials.<sup>12,13,31,32</sup> Here, we measure the local crystal orientation in solution-processed halide perovskite thin films using EBSD and demonstrate that the SEM morphology is not sufficient to characterize grain structure in these films. More importantly, we investigate the impact of grain-to-grain orientation heterogeneity and sub-grain orientation heterogeneity on local optoelectronic properties. We report the presence of local crystal misorientation leading to local strain within the grains and grain-to-grain orientation spread leading to strain heterogeneity within the film. Furthermore, we use crystallographic identification to unequivocally demonstrate and locate the sub-grain boundaries within individual grains. Lastly, we correlate EBSD and confocal photoluminescence measurements to measure the impact of local grain and sub-grain orientation heterogeneity on local photoluminescence. We observe higher non-radiative recombination in regions with higher orientation heterogeneity and lower non-radiative recombination in regions with lower orientation heterogeneity. Our results provide direct evidence for the impact of local crystal misorientation on the optoelectronic properties in halide perovskite thin films and point the way towards optimization of grain structure for improved photovoltaic performance.

## 2.3. Morphology and local crystal orientation measurements

Using a state of the art solid-state EBSD detector,<sup>21</sup> we optimized the beam current to be 100 pA at 6 kV accelerating voltage with a pixel integration time of 100 ms. We measure the Kikuchi diffraction patterns generated from the backscattered electrons using a traditional EBSD geometry with the electron beam hitting the sample at 70° with respect to the sample surface normal. Kikuchi diffraction lines generated at local Bragg angles contain the information about the local crystal orientation.<sup>33,34</sup> We scan across the sample and collect these Kikuchi patterns at every pixel and generate a local crystal orientation map of CH<sub>3</sub>NH<sub>3</sub>PbI<sub>3</sub> thin film.

Figure 2.1a shows an SEM image of a representative CH<sub>3</sub>NH<sub>3</sub>PbI<sub>3</sub> thin film grown by lead acetate and methylammonium based precursors with hypophosphorous acid additives (a recipe used for CH<sub>3</sub>NH<sub>3</sub>PbI<sub>3</sub>-based photovoltaics, see Experimental Procedures for details)<sup>35</sup> and corresponding sharp Kikuchi patterns obtained at 6 kV, 10 kV and 20 kV. Consistent with X-ray diffraction (XRD) (Appendix A Figure S1), the sharp Kikuchi patterns indicate that these films are crystalline. Moreover, these results demonstrate that we can acquire sharp patterns at the relatively low accelerating voltage of 6 kV (acquired for only 100 ms per pixel) confirming the high sensitivity and fast readout of this new EBSD detector. Figure 2.1b and 1c show the SEM image of a CH<sub>3</sub>NH<sub>3</sub>PbI<sub>3</sub> film and the corresponding Inverse Pole Figure (IPF) map generated from fitting the Kikuchi patterns to a tetragonal CH<sub>3</sub>NH<sub>3</sub>PbI<sub>3</sub> structure<sup>36,37</sup> (see Appendix A Note S1 for details and Appendix A Figure S2 for comparison of indexed results to other phases) at every pixel, with an IPF color key. An IPF map shows the projection of the sample coordinate system (xyz) in the crystal coordinate system (abc). We note that the films have strong orientation along the [110] direction along the sample z-axis as evident from the Pole Density Figure (Appendix A Figure S3). Importantly, these data provide direct evidence for the crystallographic parameters and existence of grain boundaries in these CH<sub>3</sub>NH<sub>3</sub>PbI<sub>3</sub> thin films.

Broadly, we see that the SEM image in Figure 2.1b, and the EBSD image in Figure 2.1c are in relatively good agreement. Most of the “grains” observed in SEM are indeed also present in the EBSD image (Appendix A Figure S4 and Figure S5). However, while the features observed in SEM are generally consistent with grain structure obtained from EBSD measurements (Appendix A Figure S4 and Figure S5), *we emphasize that the EBSD maps provide critical information missing from the SEM images*. For example, based on SEM morphology alone, the black arrow in the SEM image in Figure 2.1b would be assigned as going across a single “grain boundary”. However, from the corresponding IPF map (Figure 2.1c) we note that the film actually possesses 3 distinct boundaries separating 4 different local crystal orientation changes along the same arrow. Figure 2.1d depicts the changes in the local crystal orientation occurring across the arrow shown in Figure 2.1b and 1c (see Appendix A Figure S6 for higher resolution SEM image of Figure 2.1b and along the arrow). These results show that several large “grains” as seen in SEM image are composed of many smaller grains, similar to observations made using transmission electron microscope<sup>38,39</sup> and using EBSD in large grain (~50 μm) CH<sub>3</sub>NH<sub>3</sub>PbBr<sub>3</sub> samples.<sup>21</sup> Indeed, these differences between SEM and EBSD, perhaps provide another reason why efforts to relate morphological grain boundaries with carrier dynamics have not always found clear correlations.<sup>15</sup>

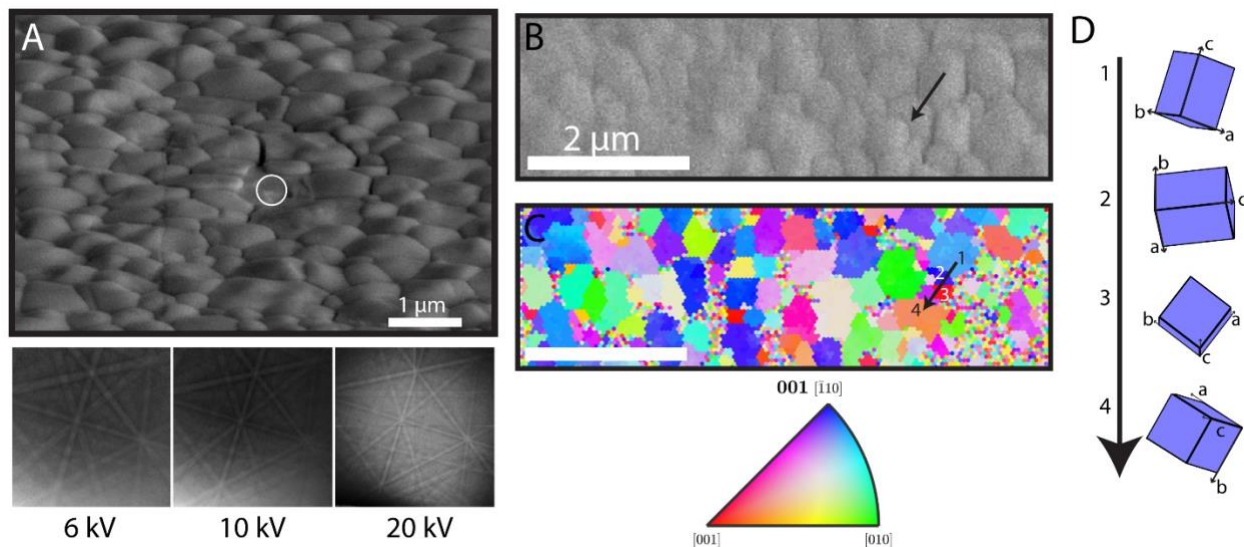


**Figure 2.1. Morphology and local crystal orientation measurements of  $\text{CH}_3\text{NH}_3\text{PbI}_3$  thin films. (A) Scanning electron microscope (SEM) image of  $\text{CH}_3\text{NH}_3\text{PbI}_3$  thin film tilted at  $45^\circ$  with representative sharp Kikuchi diffraction lines of a measurement point inside a grain (circled) collected in traditional electron backscatter diffraction (EBSD) geometry at 6 kV, 10 kV and 20 kV accelerating voltage. (B) SEM image and (C) Inverse Pole Figure (IPF) map generated from EBSD of a representative  $\text{CH}_3\text{NH}_3\text{PbI}_3$  film with IPF color key. The 001 (in bold) in the IPF color key indicates that the IPF map plotted is along the sample z-direction. (D) Depiction of changes in local crystal orientation along the black arrow in (B) and (C) as viewed normal to the sample. See Appendix A Figure S6 for a higher resolution SEM image of (B) and Figure S4 for other SEM image with IPF map.**

## 2.4. Imaging the local orientation heterogeneity, grains and grain boundaries

Figure 2.2a shows the inverse pole figure map of another typical  $\text{CH}_3\text{NH}_3\text{PbI}_3$  thin film. By assigning an appropriate threshold for misorientation ( $4^\circ$ , see Appendix A Figure S7 for results from different threshold values) we can assign each pixel in the inverse pole figure to a grain, and hence identify the grains and grain boundaries<sup>40</sup> (see Appendix A Note S1 and Figure S8 for more details on grain detection). Figure 2.2b shows the crystal grains identified by this approach, along with their grain boundaries. These maps provide a quantifiable identification of the grains and their orientation, revealing boundaries not visible in the SEM morphology images (see Appendix A Figure S9 for SEM image of the region in Figure 2.2).

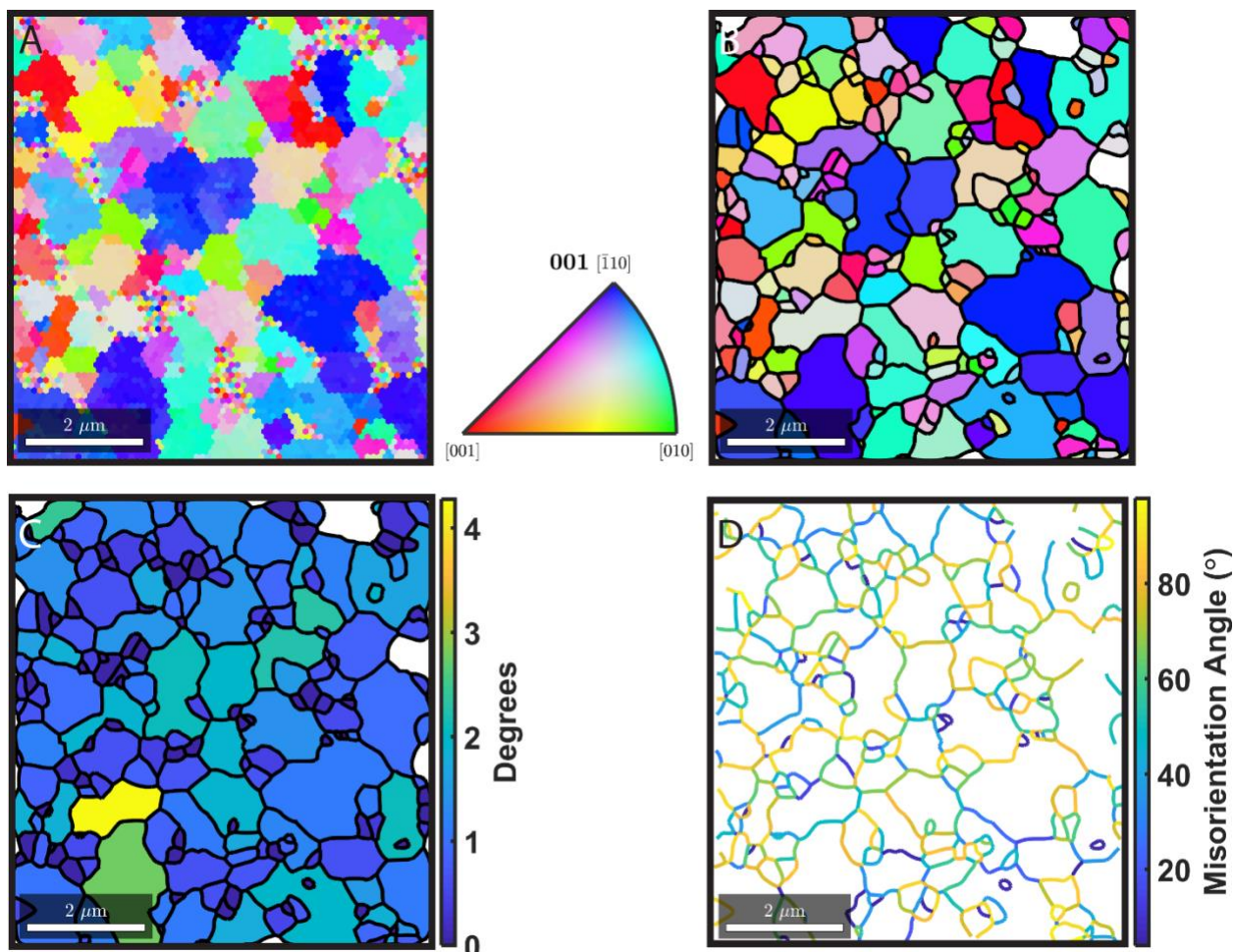


**Figure 2.2. Imaging the local orientation heterogeneity, grains and grain boundaries in CH<sub>3</sub>NH<sub>3</sub>PbI<sub>3</sub> thin films using electron back scatter diffraction (EBSD). (A) Inverse Pole Figure (IPF) map of CH<sub>3</sub>NH<sub>3</sub>PbI<sub>3</sub> generated using EBSD and IPF color key. (B) Grains identified from IPF map with a 4° orientation threshold and plotted with their mean orientation. (C) Plot of grain orientation spread (GOS) showing grain-to-grain heterogeneity in average local misorientation in the same film. (D) Grain boundary network with their respective misorientation angles showing the degree of misorientation between two neighboring grains. (B), (C) and (D) have the same orientation threshold (4°). See Appendix A Figure S9 for SEM image of the region.**

In addition to identifying grains and grain boundaries, the analysis of the IPF data in Figure 2.2 provides an additional level of insight regarding crystallographic misorientation within individual grains. For example, we observe local variations in crystal orientations within individual grains (Appendix A Figure S10) across the entire film that exceed the orientation noise in local crystallographic orientation obtained from fitting the Kikuchi pattern (see Appendix A Note S1 for details). Figure 2.2b plots the grains identified in Figure 2.2a, color coded according to their mean orientation.<sup>41,42</sup> The average deviation in orientation between each pixel (point) within a grain and the mean grain orientation of that grain is defined as the grain orientation spread (GOS).<sup>43</sup> Figure 2.2c plots the GOS values in the same region as Figure 2.2a and 2.2b of this representative CH<sub>3</sub>NH<sub>3</sub>PbI<sub>3</sub> thin film. Importantly, we observe a range of grain-to-grain orientational

heterogeneity in the film with GOS values as low as  $0^\circ$  (perfectly ordered) and as high as  $4.3^\circ$  of orientation spread within individual grains. These grain-to-grain local variations in crystal orientation are indicative of local strain distributions within the grains.<sup>43</sup> Higher GOS values indicate grains with higher strain, and lower GOS values indicate grains with lower strain.<sup>43</sup> We note that the misorientation within the grain and between neighboring points observed is not a consequence of beam induced degradation in the material (see Appendix A Figure S11). These results demonstrate the existence of potentially important local structural and strain heterogeneity in halide perovskite thin films stemming from the local crystal orientation variations. These results are consistent with, but provide better resolution, than those of Stranks *et al.*, who recently reported strain heterogeneity at long length scales in halide perovskite thin films based on  $\mu$ -XRD measurements.<sup>38</sup> Importantly, our results further demonstrate that the local strain heterogeneity observed in halide perovskite semiconductors originate from local crystal misorientation within grains. In most semiconductors, local lattice imperfections, such as local crystal orientation changes within grains observed here, can act as non-radiative recombination centers,<sup>44</sup> which in turn would have a significant influence on the performance of perovskite solar cells. We will explore this possibility in more detail below.

Alongside local crystal orientation heterogeneity, orientation imaging using EBSD also allows us to probe and understand the nature of grain boundaries in halide perovskites. Misorientation between two neighboring grains (grain boundary misorientation) can be quantified using the crystallographic misorientation angles and misorientation axes obtained using EBSD. The misorientation angle is the angle by which a grain is rotated, about the misorientation axis, such that the orientation of the transformed grain matches the neighboring grain after transformation. Figure 2.2d shows the grain boundary network and their respective misorientation angles between neighboring grains. The misorientation angle/axis statistics (Appendix A Figure S12 and Figure S13) demonstrate the presence of high angle grain boundaries with high frequency and strong preferred orientation of misorientation axis along the [110] direction. Importantly, Figure 2.2d shows that different grain boundaries have different misorientation and therefore, may have different properties. In other words, these films exhibit a range of different grain boundaries, which might be expected to exhibit different properties. As stated earlier, understanding grain boundary properties has been critical to the development of many other photovoltaic semiconductor technologies such as CdTe, GaAs, InP, and  $\text{Cu}(\text{In}_{1-x}\text{Ga}_x)\text{Se}_2$ ,<sup>22-29</sup> and indeed other materials, such as high temperature polycrystalline superconductors.<sup>45,46</sup> We anticipate that understanding the nature of the different grain boundaries identified by EBSD will be critical to understanding the properties of halide perovskite photovoltaics,<sup>21</sup> and we speculate that properties such as anisotropic charge carrier transport across grain boundaries observed in halide perovskites<sup>13,47-49</sup> could depend on grain boundary properties such as misorientation angle, type of boundary, and the boundary interface energy.

## 2.5. Sub-grain boundaries and intra-grain misorientation

Next, to investigate the structural heterogeneity at a sub-grain level in more detail, we examine crystal orientations within an individual grain. Due to high coefficient of thermal expansion anisotropy in tetragonal  $\text{CH}_3\text{NH}_3\text{PbI}_3$ , phase transition from cubic to tetragonal  $\text{CH}_3\text{NH}_3\text{PbI}_3$  during film formation can introduce a significant amount of local residual stresses in

the material.<sup>50,51</sup> These micro-stresses may be concentrated at the grain boundaries and sub-grain boundaries within the grain. Figure 2.3a shows the inverse pole figure of an individual grain from a  $\text{CH}_3\text{NH}_3\text{PbI}_3$  film with sub-grain boundaries. The grains are identified using  $4^\circ$  as the threshold, however, the grain represented in Figure 2.3 is not affected by different thresholds (see Figure S14). Sub-grain boundaries have been shown to influence charge carrier recombination in other semiconductor photovoltaic technologies like GaAs and InP.<sup>27,28</sup> Recently, using optical microscopy Li *et al.* suggested the presence of sub-grain special boundaries in large grain  $\text{NH}_2\text{CHNH}_2\text{PbI}_3$  thin films.<sup>49</sup> Here, we use crystallographic identification to unequivocally demonstrate the existence of sub-grain boundaries and precisely determine their location within the grain.

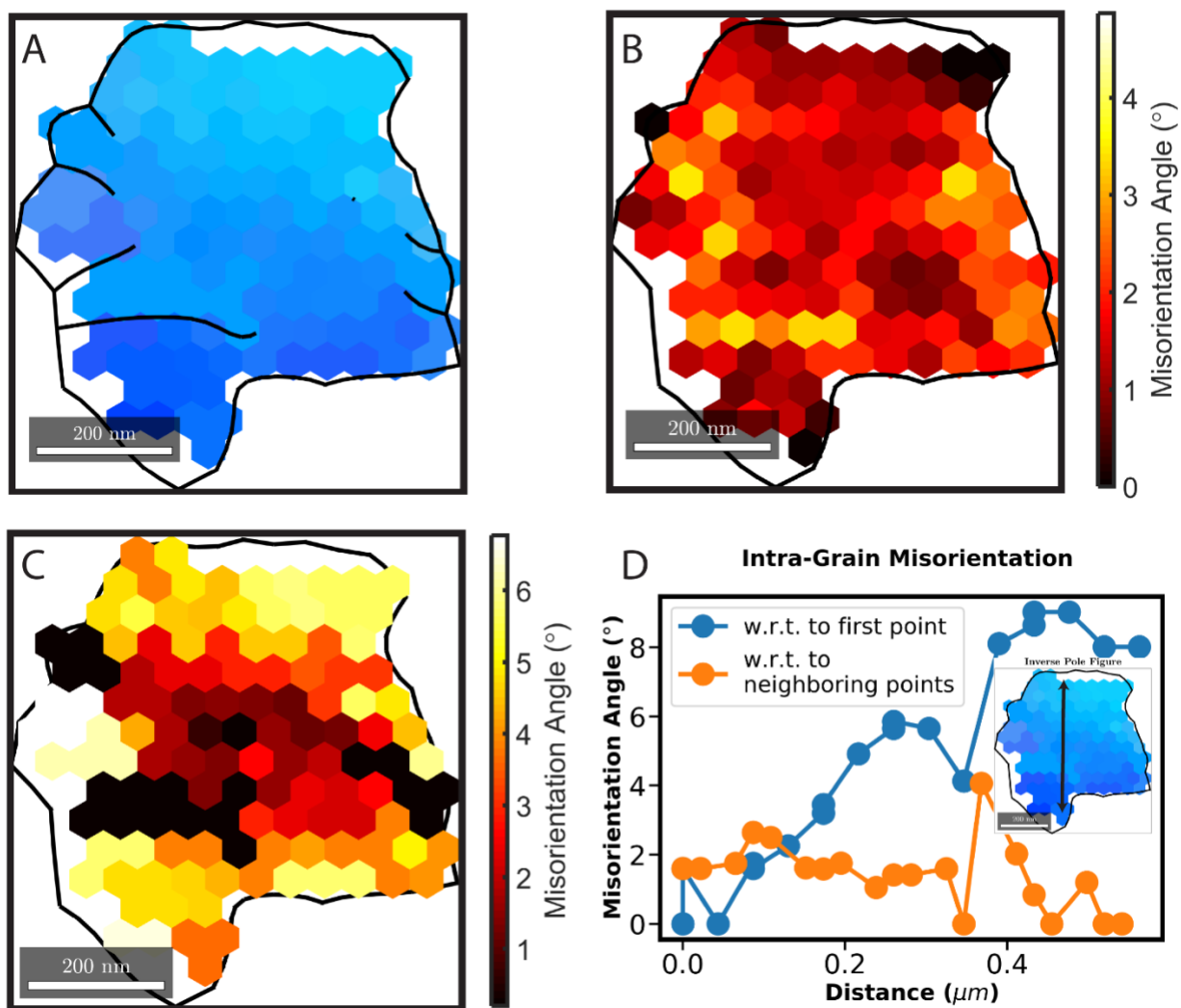


**Figure 2.3. Sub-grain boundaries and intra-grain misorientation. (A) Inverse Pole Figure (IPF) of an individual grain in a  $\text{CH}_3\text{NH}_3\text{PbI}_3$  thin film with sub-grain boundaries. The outer black lines represent the outer grain boundary (i.e. with other grains) and the inner black lines represent the sub-grain boundaries. The IPF color key is the same as Figure 2.1 and 2.2. The grains are identified using  $4^\circ$  as the threshold. (B) Kernel average misorientation**

**(KAM) showing the degree of misorientation between neighboring pixels within the grain. (C) Misorientation with respect to mean orientation of the grain showing the local orientation heterogeneity in the grain. (D) Plot of misorientation angle as a function of distance along the black arrow in the IPF in the inset. Blue circles denote the misorientation of each point with respect to the first point along the black arrow and orange circles denote the misorientation of each point with respect to its neighboring points along the arrow.**

As stated earlier, local variations in lattice orientation can manifest as residual strain within the material.<sup>50</sup> Here, we analyze local variations in lattice orientations to infer the local strain within an individual grain. Kernel average misorientation (KAM) provides the average misorientation between a measurement point and its neighboring points.<sup>43</sup> In our case, it provides the average misorientation between each point and its six neighboring points within the same grain. We note that the KAM is a kernel or an individual measurement property where each point in the grain has a local misorientation value whereas the previously described GOS is a grain property where the entire grain is assigned a local misorientation value. Figure 2.3b shows the KAM value calculated and plotted for each point within the grain. We observe KAM values as low as  $0^\circ$  and as high as  $4.87^\circ$  corresponding to low and high local misorientation regions respectively. We note that the range of KAM values ( $0$  to  $4.87^\circ$ ) observed here are *within* the same grain, demonstrating significant strain heterogeneity within an individual grain. Interestingly, the sub-grain boundaries (Figure 2.3a) are near regions with high KAM values (Figure 2.3b) consistent with the model that high misorientations within a grain will lead to sub-grain boundaries. Our observations show that local crystal misorientation generates the local strain heterogeneity observed within individual grains.

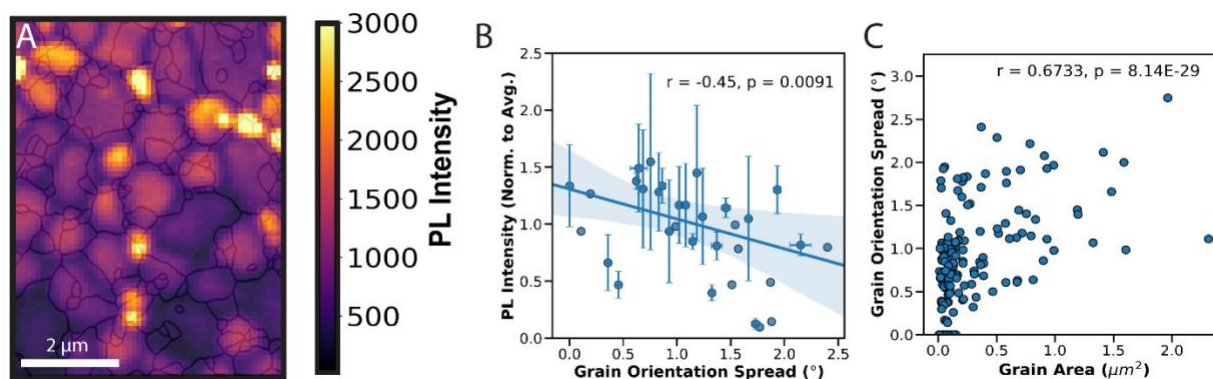
As evident from Figure 2.3a and 3b, the selected grain has a distribution of orientations within itself, exhibiting a GOS of  $3.41^\circ$ . Figure 2.3c shows the misorientation of individual measurement points within a grain with respect to the mean orientation of the grain. Regions near to the reference mean orientation have lower misorientation angle and vice-versa. We observe higher misorientation angles with respect to mean orientation closer to the grain boundaries suggesting a higher degree of lattice rotation or lattice bending near grain boundaries.

Figure 2.3d shows the plot of intra-grain misorientation angle as a function of distance within the grain, along the black arrow in the inset figure. Importantly, Figure 2.3d shows that the misorientation from one end of the grain to the other end can be as high as  $9^\circ$  (even though the grain boundaries were identified using a threshold of  $4^\circ$ ). This result could indicate the possibility of variations in carrier transport both across, and within, an individual grain if the strain affects the local carrier mobility. We note that the sub-grain heterogeneity present in the grain shown in Figure 2.3 is representative of the population (See Appendix A Figure S15 and Figure S16 for SEM image of an individual grain along with sub-grain heterogeneity characterization and sub-grain heterogeneity in more grains from different films, respectively).

## 2.6. Correlation between local luminescence, orientation heterogeneity and grain area

Finally, having quantified the local grain orientation spread, and hence the local strain, we use our high-resolution EBSD data set to explore whether grain-to-grain variations in near-surface strain (Appendix A Figure S17) could be sources of non-radiative recombination within the perovskite films. We expect the defects (and the strain) to be dominated by the surface, because surface passivated halide perovskite thin films have demonstrated single crystal like quality.<sup>4-6,52</sup> To this end, we overlay the grain-boundary network obtained from grain identification onto the confocal photoluminescence (PL) image obtained on the same region (Figure 2.4a). The grain boundary network and the confocal PL image were aligned using an image registration program and fiducial marks created using Atomic Force Microscope tip (see Appendix A Note S2 for details).

To look for any relationship between local orientation heterogeneity and local non-radiative recombination, we plot photoluminescence intensity as a function of grain orientation spread. Our group has previously demonstrated that confocal PL maps, when measured at excitation densities below the local trap density ( $\sim 10^{15} \text{ cm}^{-3}$  to  $\sim 10^{17} \text{ cm}^{-3}$ ),<sup>12,53-55</sup> can reflect the local trap distribution in the film.<sup>12,13</sup> Although carrier diffusion is still important,<sup>13,56</sup> under such conditions, high PL intensities correspond to regions with lower trap density, and low PL intensities to regions with higher trap density.<sup>13</sup>



**Figure 2.4. Correlation between local luminescence, orientation heterogeneity and grain area in CH<sub>3</sub>NH<sub>3</sub>PbI<sub>3</sub>. (A) Aligned confocal photoluminescence (PL) image and grain boundary network of the same region. (B) Plot of PL intensity as a function of Grain Orientation Spread (GOS) in MAPI showing negative correlation, with high statistical significance ( $p=0.0091$ ). The grains are binned in GOS intervals. The line represents a linear regression fit to the data with the shaded region representing a 95% confidence interval for the regression. Error bars represent the standard deviation of average PL intensity in a specific GOS interval. (C) Plot of grain orientation spread as a function of grain area showing positive correlation, with high statistical significance ( $p=8.14e-29$ ). See Appendix A Note S3 for discussion on p-value and statistical significance.**

Here, we measure confocal PL maps at low incident excitation fluences of  $\sim 0.2 \text{ μJ/cm}^2$  per pulse (at 470 nm with 1 MHz repetition rate) corresponding to an initial carrier excitation density

of  $\sim 10^{16} \text{ cm}^{-3}$  and time-averaged carrier density of  $\sim 10^{15} \text{ cm}^{-3}$ . Next, we measure the local crystal orientation across the same region using EBSD as demonstrated earlier. Using this approach, Figure 2.4b plots the normalized average PL intensity within a grain versus the grain orientation spread within the corresponding grain for more than 100 grains from different samples (see Appendix A Figure S18 for correlation plots from individual sample sets). We find a negative correlation between the grain orientation spread and PL intensity with high statistical significance ( $p$ -value = 0.0091, Appendix A Note S3 for more details on  $p$ -value). In other words, the larger the grain orientation spread, the lower the PL intensity of the local perovskite. This result provides a direct link between local intra-grain strain and local nonradiative defect density by showing that grains with higher grain orientation spreads have lower PL intensity and therefore, higher trap densities contributing to non-radiative recombination.

Figure 2.4c shows the relation between grain area and the corresponding orientation spread within the grain. We find a strong positive correlation between the grain area and grain orientation spread, with high statistical significance ( $p$ -value =  $8.14\text{e-}29$ ). We note that this conclusion does not depend on the threshold value chosen during grain detection. In other words, we observe strong positive correlation between grain area and grain orientation spread for all different grain threshold values (Appendix A Figure S19). This means that, in the case of the samples measured in this study, as the grain size increases the orientation spread (and hence, local strain) also increases. We note that at fluences used in this study (corresponding to trap densities in the film) we find very low anticorrelation ( $r = -0.2$ ) between PL intensity and grain area (Appendix A Figure S20), consistent with our previous observations.<sup>13</sup> Importantly, this result indicates that the correlation between PL and grain orientation spread shown in Figure 2.4b is *not* solely due to the relation between grain size and PL, instead grain orientation spread appears to be more important than grain size.

Notably, an increase in grain orientation spread (and local strain) with increasing grain area might help explain why some of the smaller grain films in the literature have shown higher PCE, and why increasing *apparent* grain sizes, as imaged by SEM, has not always corroborated with increasing PCE.<sup>57</sup> Specifically, we speculate that smaller grain films studied to date may have less orientation spread and thus, lower strain compared to large grains.

However, we emphasize that these results do not indicate researchers should necessarily aim to create perovskite films with smaller grains for solar cell applications. Grain boundaries and surface traps act as centers for non-radiative recombination in many materials, including halide perovskites.<sup>5-7,12,13,21,53,58-65</sup> Instead, the point we are making is that local crystal orientation is also important, perhaps more so than grain size in some films. Ideally, we would want films with larger grain sizes and low orientation spread within a grain, i.e. highly oriented and low strain. Promisingly, Choi and co-workers recently demonstrated that perovskite thin films with higher degrees of orientation can be achieved at the lab scale.<sup>66,67</sup> As lab-scale deposition techniques are translated to large-scale deposition methods such as roll-to-roll printing, spray coating and slot die coating,<sup>68,69</sup> our results, and the general methods herein, provide insight for optimizing deposition conditions, and suggest a need for orientation and strain engineering.<sup>70</sup>

## 2.7. Conclusion

In conclusion, we demonstrate local crystal orientation maps of archetypal  $\text{CH}_3\text{NH}_3\text{PbI}_3$  perovskite thin films, most commonly investigated for solar cell applications, generated using the state of the art EBSD detector with high sensitivity and fast readout. We show that while SEM morphology is generally consistent with EBSD, there are features in the film that are only visible in EBSD and therefore, SEM morphology alone is insufficient to identify grains and grain boundaries. In addition to providing true grain sizes for halide perovskites, orientation imaging using EBSD also allows us to probe the crystallographic nature of the film. We observe local crystal orientation heterogeneity within individual grains throughout the thin film and we find that the orientation heterogeneity varies from grain-to-grain. Our results demonstrate that although a grain is defined as a unit of microstructure with a single orientation, in reality, in perovskites a grain has an average orientation with significant orientational spread or heterogeneity which contributes to the local strain within the grain. We propose that such orientational heterogeneity within grains could be a result of heterogeneous nucleation and growth, variations in local concentration gradients<sup>71</sup> and/or phase transitions post-annealing.<sup>37,50,51,72,73</sup> Next, by studying the crystallographic nature of grain boundaries, we show that there are a range of different grain boundary misorientations and therefore, different grain boundaries will have different properties such as carrier transport, interface energy, etc. Using EBSD, we also demonstrate the presence of sub-grain boundaries formed near regions of high local crystal misorientation. We observed misorientations as high as  $9^\circ$  from one end of the grain to another. Finally, we use correlated confocal PL microscopy and EBSD to understand the relationship between local crystal orientation heterogeneity and local non-radiative recombination, as it relates directly to photovoltaic performance. We observe low PL intensity (high non-radiative recombination) in regions with high grain orientation spreads (high strain regions) and high PL intensity (low non-radiative recombination) in regions with low grain orientation spreads (low strain regions). Furthermore, we observe that the orientation spread increases with increasing grain sizes. Our results point towards the need to understand and control the local crystal orientation by engineering deposition protocols that provide large grains with low orientation heterogeneity (lower strain). These results provide critical insight into the interplay between local crystal orientation heterogeneity and local non-radiative recombination and furthers our understanding of the local structure-function interplay in halide perovskite thin films for photovoltaics.

See Appendix A on page 60 for experimental methods and supplementary information for chapter 2.

## Acknowledgements

This paper is primarily based on research supported by the DOE DE-SC0013957. S.J. acknowledges support from the University of Washington Clean Energy Institute and the National Science Foundation Research Traineeship under Award NSF DGE-1633216. D.S.G acknowledges support from the University of Washington, Department of Chemistry Kwiram Endowment. G.W.P.A. was supported by TKI Urban Energy, “COMPASS” (TEID215022). E.C.G. and G.W.P.A. received funding from the European Research Council grant No. 337328 “NanoEnabledPV”. E.C.G. and H.S. were supported by the Dutch Science Foundation (NWO) through the Joint Solar Program III. L.A.M. and B.E. were supported by the Dutch Science Foundation (NWO) through the project No. 680-47-553.

## References

- [1] National Renewable Energy Laboratory Efficiency Chart 2019 n.d. <https://www.nrel.gov/pv/assets/pdfs/pv-efficiency-chart.20190103.pdf> (accessed February 1, 2019).
- [2] Pazos-Outón, L.M., Xiao, T.P., and Yablonovitch, E. (2018). Fundamental Efficiency Limit of Lead Iodide Perovskite Solar Cells. *J. Phys. Chem. Lett.* *9*, 1703–1711.
- [3] Hörantner, M.T., and Snaith, H.J. (2017). Predicting and optimising the energy yield of perovskite-on-silicon tandem solar cells under real world conditions. *Energy Environ. Sci.* *10*, 1983–1993.
- [4] Braly, I.L., Dequillettes, D.W., Pazos-Outón, L.M., Burke, S., Ziffer, M.E., Ginger, D.S., and Hillhouse, H.W. (2018). Hybrid perovskite films approaching the radiative limit with over 90% photoluminescence quantum efficiency. *Nat. Photonics* *12*, 355–361.
- [5] deQuillettes, D.W., Koch, S., Burke, S., Paranjji, R., Shropshire, A.J., Ziffer, M.E., and Ginger, D.S. (2016a). Photoluminescence Lifetimes Exceeding 8  $\mu$ s and Quantum Yields Exceeding 30% in Hybrid Perovskite Thin Films by Ligand Passivation. *ACS Energy Lett.* *1*, 438–444.
- [6] Brenes, R., Guo, D., Osherov, A., Noel, N.K., Eames, C., Hutter, E.M., Pathak, S.K., Niroui, F., Friend, R.H., Islam, M.S., et al. (2017). Metal Halide Perovskite Polycrystalline Films Exhibiting Properties of Single Crystals. *Joule* *1*, 155–167.
- [7] Stavrakas, C., Zhumekenov, A.A., Brenes, R., Abdi-Jalebi, M., Bulović, V., Bakr, O.M., Barnard, E.S., and Stranks, S.D. (2018). Probing buried recombination pathways in perovskite structures using 3D photoluminescence tomography. *Energy Environ. Sci.* *11*, 2846.
- [8] Wang, J., Fu, W., Jariwala, S., Sinha, I., Jen, A.K.-Y., and Ginger, D.S. (2018b). Reducing Surface Recombination Velocities at the Electrical Contacts Will Improve Perovskite Photovoltaics. *ACS Energy Lett.* *4*, 222–227.
- [9] Stolterfoht M, Caprioglio P, Wolff CM, Márquez JA, Nordmann J, Zhang S, et al. The perovskite/transport layer interfaces dominate non-radiative recombination in efficient

- perovskite solar cells. Preprint at <http://arxiv.org/abs/1810.01333> 2018.
- [10] Schnitzer, I., Yablonovitch, E., Caneau, C., and Gmitter, T.J. (1993). Ultrahigh spontaneous emission quantum efficiency, 99.7% internally and 72% externally, from AlGaAs/GaAs/AlGaAs double heterostructures. *Appl. Phys. Lett.* *62*, 131–133.
- [11] Abdi-Jalebi, M., Andaji-Garmaroudi, Z., Cacovich, S., Stavrakas, C., Philippe, B., Richter, J.M., Alsari, M., Booker, E.P., Hutter, E.M., Pearson, Andrew J., et al. (2018). Maximizing and stabilizing luminescence from halide perovskites with potassium passivation. *Nature* *555*, 497–501.
- [12] DeQuilettes, D.W., Vorpahl, S.M., Stranks, S.D., Nagaoka, H., Eperon, G.E., Ziffer, M.E., Snaith, H.J., and Ginger, D.S. (2015). Impact of microstructure on local carrier lifetime in perovskite solar cells. *Science* *348*, 683–686.
- [13] DeQuilettes, D.W., Jariwala, S., Burke, S., Ziffer, M.E., Wang, J.T.W., Snaith, H.J., and Ginger, D.S. (2017). Tracking Photoexcited Carriers in Hybrid Perovskite Semiconductors: Trap-Dominated Spatial Heterogeneity and Diffusion. *ACS Nano* *11*, 11488–11496.
- [14] Yun, J.S., Ho-Baillie, A., Huang, S., Woo, S.H., Heo, Y., Seidel, J., Huang, F., Cheng, Y.B., and Green, M.A. (2015). Benefit of grain boundaries in organic-inorganic halide planar perovskite solar cells. *J. Phys. Chem. Lett.* *6*, 875–880.
- [15] Yang, M., Zeng, Y., Li, Z., Kim, D., Jiang, C.-S., van de Lagemaat, J., and Zhu, K. (2017a). Do Grain Boundaries Dominate Non-Radiative Recombination in CH<sub>3</sub>NH<sub>3</sub>PbI<sub>3</sub> Perovskite Thin Films? *Phys. Chem. Chem. Phys.* *19*, 5043–5050.
- [16] Zhou, Y., Game, O.S., Pang, S., and Padture, N.P. (2015). Microstructures of Organometal Trihalide Perovskites for Solar Cells: Their Evolution from Solutions and Characterization. *J. Phys. Chem. Lett.* *6*, 4827–4839.
- [17] Dr. Joseph J. Berry, National Renewable Energy Laboratory [@joe\_jberry] (June 30, 2018) [Tweet] n.d. [https://twitter.com/joe\\_jberry/status/1013192769316139008](https://twitter.com/joe_jberry/status/1013192769316139008) (accessed February 12, 2019).
- [18] Xiao, C., Li, Z., Guthrey, H., Moseley, J., Yang, Y., Wozny, S., Moutinho, H., To, B., Berry, J.J., Gorman, B., et al. (2015). Mechanisms of Electron-Beam-Induced Damage in Perovskite Thin Films Revealed by Cathodoluminescence Spectroscopy. *J. Phys. Chem. C* *119*, 26904–26911.
- [19] Rothmann, M.U., Li, W., Zhu, Y., Liu, A., Ku, Z., Bach, U., Etheridge, J., and Cheng, Y.-B. (2018). Structural and Chemical Changes to CH<sub>3</sub>NH<sub>3</sub>PbI<sub>3</sub> Induced by Electron and Gallium Ion Beams. *Adv. Mater.* *30*, 1800629.
- [20] Leonhard, T., Schulz, A., Röhm, H., Wagner, S., Altermann, F.J., Rheinheimer, W., Hoffmann, M.J., and Colsmann, A. (2019). Probing the Microstructure of Methylammonium Lead Iodide Perovskite Solar Cells. *Energy Technol.*
- [21] Adhyaksa, G.W.P., Brittan, S., Āboliņš, H., Lof, A., Li, X., Keelor, J.D., Luo, Y., Duevski, T., Heeren, R.M.A., Ellis, S.R., et al. (2018). Understanding Detrimental and Beneficial Grain Boundary Effects in Halide Perovskites. *Adv. Mater.* *1804792*, 1–9.
- [22] Kawamura, M., Yamada, T., Suyama, N., Yamada, A., and Konagai, M. (2010). Grain boundary evaluation of Cu(In<sub>1-x</sub>Ga<sub>x</sub>)Se<sub>2</sub> solar cells. *Jpn. J. Appl. Phys.* *49*, 0623011–0623013.
- [23] Walls, J.M., Abbas, A., West, G.D., Bowers, J.W., Isherwood, P.J.M., Kaminski, P.M., Maniscalco, B., Sampath, W.S., and Barth, K.L. (2013). The effect of annealing

treatments on close spaced sublimated cadmium telluride thin film solar cells. In *Materials Research Society Symposium Proceedings*, (IEEE), pp. 147–152.

- [24] Stoffers, A., Cojocar-Mirédin, O., Seifert, W., Zaefferer, S., Riepe, S., and Raabe, D. (2015). Grain boundary segregation in multicrystalline silicon: Correlative characterization by EBSD, EBIC, and atom probe tomography. *Prog. Photovoltaics Res. Appl.* *23*, 1742–1753.
- [25] Poplawsky, J.D., Paudel, N.R., Li, C., Parish, C.M., Leonard, D., Yan, Y., and Pennycook, S.J. (2014). Direct Imaging of Cl- and Cu-Induced Short-Circuit Efficiency Changes in CdTe Solar Cells. *Adv. Energy Mater.* *4*, 1400454.
- [26] Nichterwitz, M., Abou-Ras, D., Sakurai, K., Bundesmann, J., Unold, T., Scheer, R., and Schock, H.W. (2009). Influence of grain boundaries on current collection in Cu(In,Ga)Se<sub>2</sub> thin-film solar cells. *Thin Solid Films* *517*, 2554–2557.
- [27] Brown, E., Sheng, C., Shimamura, K., Shimojo, F., and Nakano, A. (2015). Enhanced charge recombination due to surfaces and twin defects in GaAs nanostructures. *J. Appl. Phys.* *117*, 054307.
- [28] Woo, R.L., Xiao, R., Kobayashi, Y., Gao, L., Goel, N., Hudait, M.K., Mallouk, T.E., and Hicks, R.F. (2008). Effect of twinning on the photoluminescence and photoelectrochemical properties of indium phosphide nanowires grown on silicon (111). *Nano Lett.* *8*, 4664–4669.
- [29] Abou-Ras, D., and Pantleon, K. (2007). The impact of twinning on the local texture of chalcopyrite-type thin films. *Phys. Status Solidi - Rapid Res. Lett.* *1*, 187–189.
- [30] Saliba, M., Correa-Baena, J.-P., Grätzel, M., Hagfeldt, A., and Abate, A. (2018). Perovskite Solar Cells: From the Atomic Level to Film Quality and Device Performance. *Angew. Chemie Int. Ed.* *57*, 2554–2569.
- [31] Leblebici, S.Y., Leppert, L., Li, Y., Reyes-Lillo, S.E., Wickenburg, S., Wong, E., Lee, J., Melli, M., Ziegler, D., Angell, D.K., et al. (2016). Facet-dependent photovoltaic efficiency variations in single grains of hybrid halide perovskite. *Nat. Energy* *1*, 16093.
- [32] Guo, Z., Manser, J.S., Wan, Y., Kamat, P. V, and Huang, L. (2015). Spatial and temporal imaging of long-range charge transport in perovskite thin films by ultrafast microscopy. *Nat. Commun.* *6*.
- [33] Nishikawa, S., and Kikuchi, S. (1928). Diffraction of Cathode Rays by Mica. *Nature* *121*, 1019–1020.
- [34] Levine, E., Bell, W.L., and Thomas, G. (1966). Further applications of Kikuchi diffraction patterns; Kikuchi maps. *J. Appl. Phys.* *37*, 2141–2148.
- [35] Zhang, W., Saliba, M., Moore, D.T., Pathak, S.K., Hörantner, M.T., Stergiopoulos, T., Stranks, S.D., Eperon, G.E., Alexander-Webber, J.A., Abate, A., et al. (2015). Ultrasoft organic-inorganic perovskite thin-film formation and crystallization for efficient planar heterojunction solar cells. *Nat. Commun.* *6*.
- [36] Poglitsch, A., and Weber, D. (1987). Dynamic disorder in methylammoniumtrihalogenoplumbates (II) observed by millimeter-wave spectroscopy. *J. Chem. Phys.* *87*, 6373–6378.
- [37] Baikie, T., Fang, Y., Kadro, J.M., Schreyer, M., Wei, F., Mhaisalkar, S.G., Gratzel, M., and White, T.J. (2013). Synthesis and crystal chemistry of the hybrid perovskite (CH<sub>3</sub>NH<sub>3</sub>)PbI<sub>3</sub> for solid-state sensitised solar cell applications. *J. Mater. Chem. A* *1*, 5628.

- [38] Jones, T.W., Osherov, A., Alsari, M., Sponseller, M., Duck, B.C., Jung, Y.-K., Settens, C., Niroui, F., Brenes, R., Stan, C., et al. (2019). Lattice Strain Causes Non-Radiative Losses in Halide Perovskites. *Energy Environ. Sci.* *12*, 596–606
- [39] Rothmann, M.U., Li, W., Etheridge, J., and Cheng, Y.-B. (2017a). Microstructural Characterisations of Perovskite Solar Cells - From Grains to Interfaces: Techniques, Features, and Challenges. *Adv. Energy Mater.* *7*, 1700912.
- [40] Bachmann, F., Hielscher, R., and Schaeben, H. (2011). Grain detection from 2d and 3d EBSD data-Specification of the MTEX algorithm. *Ultramicroscopy* *111*, 1720–1733.
- [41] Kunze, K., Wright, S.I., Adams, B.L., and Dingley, D.J. (1993). Advances in automatic EBSD single orientation measurements. *Textures Microstruct.* *20*, 41–54.
- [42] Bachmann, F., Hielscher, R., Jupp, P.E., Pantleon, W., Schaeben, H., and Wegert, E. (2010). Inferential statistics of electron backscatter diffraction data from within individual crystalline grains. *J. Appl. Crystallogr.* *43*, 1338–1355.
- [43] Wright, S.I., Nowell, M.M., and Field, D.P. (2011). A review of strain analysis using electron backscatter diffraction. *Microsc. Microanal.* *17*, 316–329.
- [44] Stoneham, A.M. (1981). Non-radiative transitions in semiconductors. *Reports Prog. Phys.* *44*, 1251–1295.
- [45] Klie, R.F., Buban, J.P., Varela, M., Franceschetti, A., Jooss, C., Zhu, Y., Browning, N.D., Pantelides, S.T., and Pennycook, S.J. (2005). Enhanced current transport at grain boundaries in high-Tc superconductors. *Nature* *435*, 475–478.
- [46] Dimos, D., Chaudhari, P., and Mannhart, J. (1990). Superconducting transport properties of grain boundaries in YBa<sub>2</sub>Cu<sub>3</sub>O<sub>7</sub> bicrystals. *Phys. Rev. B* *41*, 4038–4049.
- [47] Snaider, J.M., Guo, Z., Wang, T., Yang, M., Yuan, L., Zhu, K., and Huang, L. (2018). Ultrafast Imaging of Carrier Transport across Grain Boundaries in Hybrid Perovskite Thin Films. *ACS Energy Lett.* *3*, 1402–1408.
- [48] Delor M, Weaver HL, Yu Q, Ginsberg NS. Universal imaging of material functionality through nanoscale tracking of energy flow. Preprint at <http://arxiv.org/abs/1805.09982> 2018.
- [49] Li, W., Yadavalli, S.K., Lizarazo-Ferro, D., Chen, M., Zhou, Y., Padture, N.P., and Zia, R. (2018). Subgrain special boundaries in halide perovskite thin films restrict carrier diffusion. *ACS Energy Lett.* *3*, 2669–2670.
- [50] Ramirez, C., Yadavalli, S.K., Garces, H.F., Zhou, Y., and Padture, N.P. (2018). Thermo-mechanical behavior of organic-inorganic halide perovskites for solar cells. *Scr. Mater.* *150*, 36–41.
- [51] Rolston, N., Bush, K.A., Printz, A.D., Gold-Parker, A., Ding, Y., Toney, M.F., McGehee, M.D., and Dauskardt, R.H. (2018). Engineering Stress in Perovskite Solar Cells to Improve Stability. *Adv. Energy Mater.* *8*, 1802139.
- [52] Noel, N.K., Abate, A., Stranks, S.D., Parrott, E.S., Burlakov, V.M., Goriely, A., and Snaith, H.J. (2014). Enhanced Photoluminescence and Solar Cell Performance via Lewis Base Passivation of Organic-Inorganic Lead Halide Perovskites. *ACS Nano* *8*, 9815–9821.
- [53] deQuilettes, D.W., Zhang, W., Burlakov, V.M., Graham, D.J., Leijtens, T., Osherov, A., Bulović, V., Snaith, H.J., Ginger, D.S., and Stranks, S.D. (2016c). Photo-induced halide redistribution in organic-inorganic perovskite films. *Nat. Commun.* *7*, 11683.

- [54] Stranks, S.D., Burlakov, V.M., Leijtens, T., Ball, J.M., Goriely, A., and Snaith, H.J. (2014). Recombination Kinetics in Organic-Inorganic Perovskites: Excitons, Free Charge, and Subgap States. *Phys. Rev. Appl.* 2.
- [55] Herz, L.M. (2016). Charge-Carrier Dynamics in Organic-Inorganic Metal Halide Perovskites. *Annu. Rev. Phys. Chem.* 67, 65–89.
- [56] Tian, W., Cui, R., Leng, J., Liu, J., Li, Y., Zhao, C., Zhang, J., Deng, W., Lian, T., and Jin, S. (2016). Limiting Perovskite Solar Cell Performance by Heterogeneous Carrier Extraction. *Angew. Chemie - Int. Ed.* 55, 13067–13071.
- [57] Wang, F., Bai, S., Tress, W., Hagfeldt, A., and Gao, F. (2018a). Defects engineering for high-performance perovskite solar cells. *Npj Flex. Electron.* 2, 22.
- [58] Simpson, M.J., Doughty, B., Das, S., Xiao, K., and Ma, Y.Z. (2017). Separating Bulk and Surface Contributions to Electronic Excited-State Processes in Hybrid Mixed Perovskite Thin Films via Multimodal All-Optical Imaging. *J. Phys. Chem. Lett.* 8, 3299–3305.
- [59] Yamashita, D., Handa, T., Ihara, T., Tahara, H., Shimazaki, A., Wakamiya, A., and Kanemitsu, Y. (2016). Charge Injection at the Heterointerface in Perovskite CH<sub>3</sub>NH<sub>3</sub>PbI<sub>3</sub> Solar Cells Studied by Simultaneous Microscopic Photoluminescence and Photocurrent Imaging Spectroscopy. *J. Phys. Chem. Lett.* 7, 3186–3191.
- [60] Eperon, G.E., Moerman, D., and Ginger, D.S. (2016). Anticorrelation between Local Photoluminescence and Photocurrent Suggests Variability in Contact to Active Layer in Perovskite Solar Cells. *ACS Nano* 10, 10258–10266.
- [61] Moerman, D., Eperon, G.E., Precht, J.T., and Ginger, D.S. (2017). Correlating Photoluminescence Heterogeneity with Local Electronic Properties in Methylammonium Lead Tribromide Perovskite Thin Films. *Chem. Mater.* 29, 5484–5492.
- [62] Brenes, R., Eames, C., Bulović, V., Islam, M.S., and Stranks, S.D. (2018). The Impact of Atmosphere on the Local Luminescence Properties of Metal Halide Perovskite Grains. *Adv. Mater.* 30, 1–8.
- [63] Bischak, C.G., Sanehira, E.M., Precht, J.T., Luther, J.M., and Ginsberg, N.S. (2015). Heterogeneous Charge Carrier Dynamics in Organic-Inorganic Hybrid Materials: Nanoscale Lateral and Depth-Dependent Variation of Recombination Rates in Methylammonium Lead Halide Perovskite Thin Films. *Nano Lett.* 15, 4799–4807.
- [64] Draguta, S., Thakur, S., Morozov, Y. V., Wang, Y., Manser, J.S., Kamat, P. V., and Kuno, M. (2016). Spatially Non-uniform Trap State Densities in Solution-Processed Hybrid Perovskite Thin Films. *J. Phys. Chem. Lett.* 7, 715–721.
- [65] Vrucinic, M., Matthiesen, C., Sadhanala, A., Divitini, G., Cacovich, S., Dutton, S.E., Ducati, C., Atature, M., Snaith, H., Friend, R.H., et al. (2015). Local Versus Long-Range Diffusion Effects of Photoexcited States on Radiative Recombination in Organic-Inorganic Lead Halide Perovskites. *Adv. Sci.* 2, 1–6.
- [66] Foley, B.J., Cuthriell, S., Yazdi, S., Chen, A.Z., Guthrie, S.M., Deng, X., Giri, G., Lee, S.-H., Xiao, K., Doughty, B., et al. (2018). Impact of Crystallographic Orientation Disorders on Electronic Heterogeneities in Metal Halide Perovskite Thin Films. *Nano Lett.* 18, 6271–6278.
- [67] Chen, A.Z., Foley, B.J., Ma, J.H., Alpert, M.R., Niezgoda, J.S., and Choi, J.J. (2017). Crystallographic orientation propagation in metal halide perovskite thin films. *J. Mater. Chem. A* 5, 7796–7800.
- [68] Dou, B., Whitaker, J.B., Bruening, K., Moore, D.T., Wheeler, L.M., Ryter, J., Breslin, N.J., Berry, J.J., Garner, S.M., Barnes, F.S., et al. (2018). Roll-to-Roll Printing of

- Perovskite Solar Cells. *ACS Energy Lett.* **3**, 2558–2565.
- [69] Yang, M., Li, Z., Reese, M.O., Reid, O.G., Kim, D.H., Siol, S., Klein, T.R., Yan, Y., Berry, J.J., Van Hest, M.F.A.M., et al. (2017). Perovskite ink with wide processing window for scalable high-efficiency solar cells. *Nat. Energy* **2**, 17038.
- [70] Zhu, C., Niu, X., Fu, Y., Li, N., Hu, C., Chen, Y., He, X., Na, G., Liu, P., Zai, H., et al. (2019). Strain engineering in perovskite solar cells and its impacts on carrier dynamics. *Nat. Commun.* **10**, 815.
- [71] Hu, Q., Zhao, L., Wu, J., Gao, K., Luo, D., Jiang, Y., Zhang, Z., Zhu, C., Schaible, E., Hexemer, A., et al. (2017). In situ dynamic observations of perovskite crystallisation and microstructure evolution intermediated from [PbI<sub>6</sub>]<sup>4-</sup> cage nanoparticles. *Nat. Commun.* **8**.
- [72] Vorpahl, S.M., Giridharagopal, R., Eperon, G.E., Hermes, I.M., Weber, S.A.L., and Ginger, D.S. (2018). Orientation of Ferroelectric Domains and Disappearance upon Heating Methylammonium Lead Triiodide Perovskite from Tetragonal to Cubic Phase. *ACS Appl. Energy Mater.* **1**, 1534–1539.
- [73] Rothmann, M.U., Li, W., Zhu, Y., Bach, U., Spiccia, L., Etheridge, J., and Cheng, Y.-B. (2017b). Direct observation of intrinsic twin domains in tetragonal CH<sub>3</sub>NH<sub>3</sub>PbI<sub>3</sub>. *Nat. Commun.* **8**, 14547.

# Chapter 3. Impact of Dimethylammonium on Local Chemical Composition in Halide Perovskites

## 3.1. Overview

Adding a large A-site cation, such as dimethylammonium (DMA), to the perovskite growth solution has been shown to improve performance and long-term operational stability of halide perovskite solar cells. To better understand the origins of these improvements, we explore the changes in film structure, composition, and optical properties of a  $\text{DMA}_{0.1}\text{FA}_{0.6}\text{Cs}_{0.3}\text{Pb}(\text{I}_{0.8}\text{Br}_{0.2})_3$  perovskite following addition of DMA to the perovskite growth solution. Using time of flight secondary ion mass spectrometry (TOF-SIMS) we show that DMA is indeed incorporated into the perovskite, with a much higher DMA concentration at the surface. Using a combination of PL microscopy and photo-induced force microscopy (PiFM), we demonstrate that incorporating DMA into the film leads to increased local heterogeneity in the local bandgap, and to clustering of the local formamidinium ( $\text{CH}_5\text{N}_2^+$ ) composition. Our results suggest that while current-DMA-additive based approaches do have benefits to operational stability and device performance, process optimization to achieve local compositional homogeneity could further improve the device performance and operational stability, bringing further gains to solar cells using DMA additives.

## 3.2. Introduction

Halide perovskite solar cells have demonstrated rapid improvements in power conversion efficiencies (PCE), with the current single junction cell record being 25.5%, the Si/perovskite tandem record at 29.5%, and the all-perovskite 2-terminal tandem at 24.3%.<sup>1</sup> Nevertheless, these efficiencies are still below the theoretical efficiency of (~32%) for a 1.5 eV single junction perovskite cell, or (~43%) for an ideal perovskite tandem. Many of these limitations are due to open circuit voltage losses in working cells,<sup>2-15</sup> especially in wide-bandgap perovskites needed for optimal tandem cells.<sup>6,7,11,16-20</sup>

As a result, researchers have tried many approaches to achieve stable, wide-bandgap perovskites, including both tuning the X site<sup>13,17,21</sup> (particularly with Br incorporation), as well as tuning the A-site.<sup>11,16,22-25</sup> Tuning the A-site can indirectly alter the bandgap by changing the octahedral tilt and thus, the electronic orbital overlap.<sup>11,16,22-24</sup> For instance, Stoddard *et al.* reported the use of a large organic cation such as guanidinium (GA) to increase the bandgap.<sup>16</sup> Rajagopal *et al.* reported the use of phenylethylammonium (PEA) to increase the bandgap as well as improve the relative quasi-fermi level splitting w.r.t the bandgap.<sup>11</sup> Recently, Palmstrom *et al.* demonstrated the use of another large organic cation, dimethylammonium (DMA), to increase the bandgap as well as the long-term operational stability of the resulting devices.<sup>24,25</sup>

Although tuning the A-site using large organic cations has demonstrated improvements in the device performance and operation stability,<sup>11,16,24,25</sup> the microscopic chemical origins of these performance changes remains largely unknown. Here, by “large organic cations”, we mean cations with a large enough ionic radii that would not form a 3D perovskite structure according to the empirical observations based on established Goldschmidt’s tolerance factor (between 0.8-1.0 for 3D perovskites).<sup>23,26,27</sup> Here, we investigate the local chemical impact of using DMA in a mixed cation and mixed halide system. We use a mixed cation, mixed halide system with DMA addition reported by Palmstrom and Eperon *et al.*,<sup>24,25</sup>  $\text{DMA}_{10}\text{FA}_{60}\text{Cs}_{30}\text{Pb}(\text{I}_{80}\text{Br}_{20})_3$ , referred to as DMA10 for brevity. We compare the DMA10 system to control systems without DMA,  $\text{FA}_{80}\text{Cs}_{20}\text{Pb}(\text{I}_{80}\text{Br}_{20})_3$  and  $\text{FA}_{67}\text{Cs}_{33}\text{Pb}(\text{I}_{80}\text{Br}_{20})_3$ , referred to as Ctrl 80/20 and Ctrl 67/33, respectively. Ctrl 80/20 has a bandgap of 1.65 eV and is the starting composition from where we tune the DMA incorporation to get DMA10.<sup>24</sup> Ctrl 67/33 has the same FA/Cs ratio as the DMA10 composition and serves as additional control to help investigate the impact of DMA on the A-site, ruling out any influence that could be due to increase in Cs in the solution or lower FA/Cs ratio, as in Ctrl 80/20 (see SI for details on sample fabrication and UV-Vis- Figure S1).

### 3.3. Time-of-flight secondary-ion-mass spectrometry

In order to understand the chemical composition of the DMA10 and control films, we perform time-of-flight secondary ion mass spectrometry (TOF-SIMS). TOF-SIMS has been used to investigate the chemical composition in various different perovskite compositions.<sup>13,28–31</sup> Since DMA10 and control films have identical molecular components, the samples cannot be easily differentiated based on the presence or absence of different peaks. To overcome this limitation, we, first, identify and label the relevant characteristic peaks from the raw TOF-SIMS spectra. Next, we use a dimensionality reduction method, principal component analysis (PCA), on the labelled TOF-SIMS spectra. PCA has been widely used for TOF-SIMS spectral decomposition<sup>32–35</sup> as well as for other dimensionality reduction problems.<sup>36</sup> Using PCA, we decompose the labelled TOF-SIMS spectra data from 31 different spectral dimensions to 3 principal components that explain over 99% of the observed variance in the spectral data for different samples (Figure S2). Figure 1a shows the first principal component vs the second principal component for DMA10 and control films. We note that all the DMA10 samples cluster together and separate from the different control samples clusters. This indicates that there are, indeed, chemical differences between the three different sample groups – DMA10, Ctrl 67/33, and Ctrl 80/20. In other words, adding DMA to the precursor solution leads to chemical variations in the resulting film. The largest variations between the DMA10 samples and the control samples occur along the first principal component (Figure 1a). The loadings plot (Figure S3) corresponding to the scores of the first principal component shows the highest loadings are for the  $m/z$  45.05, 46.06, and 73.08, which correspond to FA, DMA, and  $\text{C}_3\text{H}_9\text{N}_2^+$ . The higher loadings indicate that the variations observed along the first principal component are primarily due to the differences in these mass numbers.

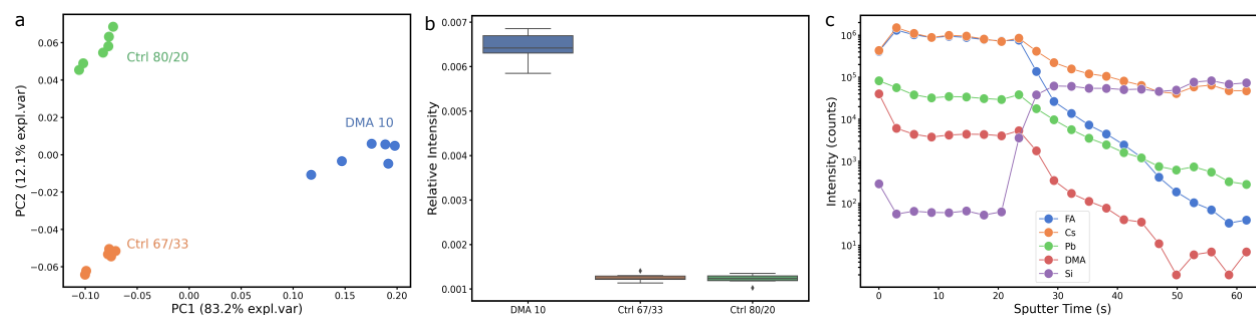


**Figure 3.1. TOF-SIMS analysis of halide perovskite films prepared with the compositions DMA<sub>10</sub>FA<sub>60</sub>Cs<sub>30</sub>Pb(I<sub>80</sub>Br<sub>20</sub>)<sub>3</sub> (DMA10), FA<sub>67</sub>Cs<sub>33</sub>Pb(I<sub>80</sub>Br<sub>20</sub>)<sub>3</sub> (Ctrl 67/33), and FA<sub>80</sub>Cs<sub>20</sub>Pb(I<sub>80</sub>Br<sub>20</sub>)<sub>3</sub> (Ctrl 80/20). a) Principal component analysis (PCA) of TOF-SIMS spectra data collected for DMA 10, Ctrl 67/33 and Ctrl 80/20 thin films. Plot of the first principal component vs the second principal component for the DMA10, Ctrl 67/33, and Ctrl 80/20 samples. b) Intensity of the  $m/z=46.06$  (DMA peak) relative to the total intensity counts from TOF-SIMS spectra for DMA10, Ctrl 67/33, and Ctrl 80/20. c) TOF-SIMS depth profile of the positive ions (FA, Cs, Pb, DMA, Si) in a representative DMA10 film.**

Figure 1b shows the normalized relative intensity for the 46.06  $m/z$ , which corresponds to DMA. We observe that the peak for  $m/z$  46.06 is only present in the DMA10 samples. Notably, the presence of this peak in the DMA10 samples but not the others, confirms that DMA is indeed incorporated into the film from the precursor solution: despite the larger size (2.72 Å, that would lead to tolerance factor greater than 1), DMA is present in the film. In addition, the TOF-SIMS signals show that intensity of  $m/z$  45.05 or FA (normalized to the total counts) qualitatively agrees with the amount of FA added to the precursor solution (Figure S5) *i.e.*, Ctrl 80/20 has higher FA than ctrl 67/33 and the DMA10 films (60% FA). The TOF-SIMS data also confirm the same qualitative trends in Cs intensity, with the relative Cs signals determined from TOF-SIMS tracking the concentrations in the precursor solutions (Figure S6).

To understand the chemical variations associated with DMA addition as function of depth in the thin film, we took TOF-SIMS depth profiles. Figure 1c shows a representative depth profile showing the intensity of the FA, Cs, Pb, and DMA ions in DMA-incorporated thin films. Increasing sputter time indicates increasing depth into the film. We observe that the DMA intensity is highest at the surface, and then decreases with increasing depth before reaching a relatively constant level in the bulk of the film. The FA and Cs intensities show the opposite trend from DMA: notably, their concentration is lowest at the surface, and increases as we probe past the surface layer, before reaching a relatively constant value throughout the bulk. We observe similar intensity depth profiles across different samples and regions (Figure S7). We note that despite a higher concentration of DMA at the surface, using XRD we do not observe a secondary 2D phase (Figure S8), consistent with previous reports of no secondary 2D phases at 10% DMA addition.<sup>24</sup> Finally, we also observe relatively constant intensity profiles across the depth for I and Br (Figure S9), indicating there is relatively little variation in halide distribution throughout the depth of the film. The intensity depth profiles for the positive ions along with the TOF-SIMS spectra data suggest that although DMA is incorporated throughout the film, the overall incorporation is non-uniform with a relatively higher concentration of DMA at the surface. The higher concentration at

the surface suggests that the higher performance for DMA-incorporated films observed by our co-authors could possibly originate in part due to surface passivation by DMA.

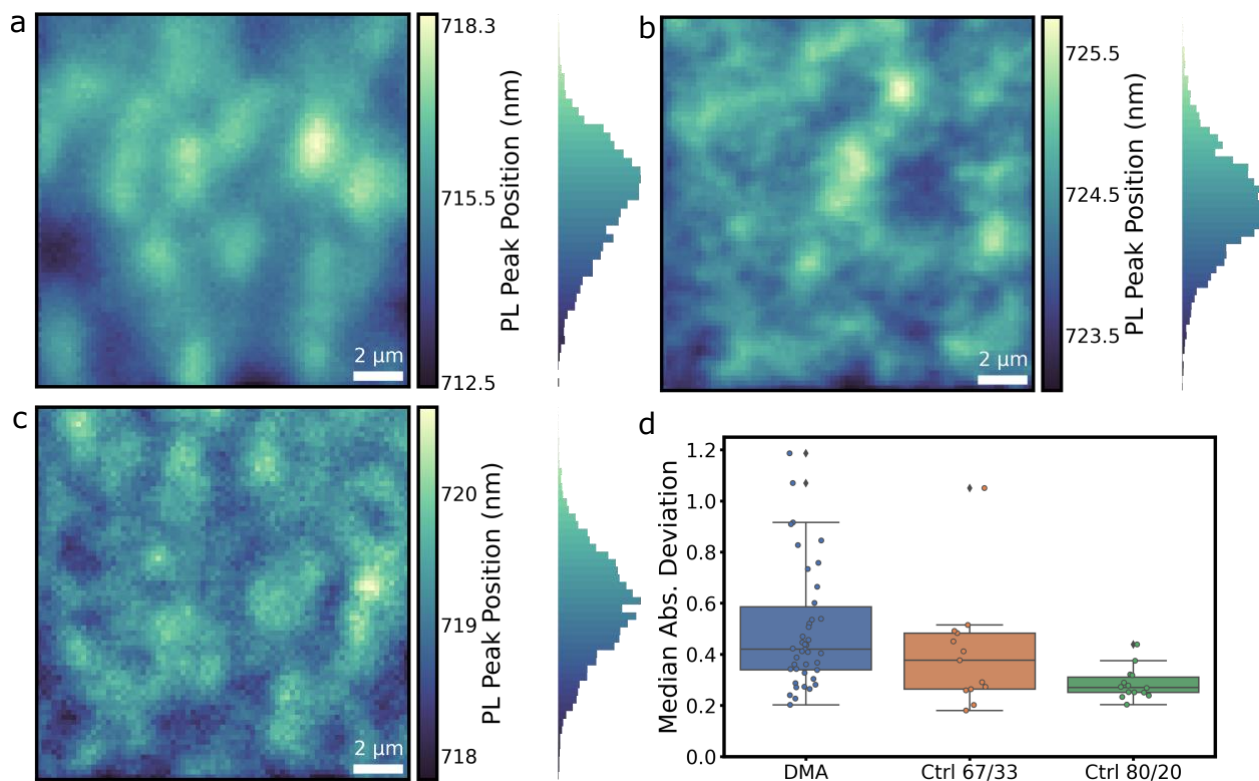


**Figure 3.2.** PL spectroscopy images of (a) DMA10, (b) Ctrl 80/20, and (c) Ctrl 67/33 thin films, local PL spectra were acquired at each pixel. The histograms in (a), (b), and (c) have the same scale as the z-scale in the respective images. (d) Box plot of median absolute deviation of the local PL spectra for DMA10 (n=42), Ctrl 67/33 (n=13), and Ctrl 80/20 (n=14) thin films. The boxes show quartiles of the data, and the whiskers extend to capture the rest of the distribution. The scatter points are individual data points.

### 3.4. Photoluminescence Microscopy

To investigate the microscopic origin of the performance improvements, we acquire local PL spectra on DMA10 and control thin films. Figures 2a-c show images of local PL peak position for representative DMA10, Ctrl 80/20, and Ctrl 67/33 thin films, respectively. We find that the DMA incorporated films have a higher variation in the local PL peak position (Figure 2a). The distinct regions of higher and lower PL peak position suggest that there are local compositional variations in the DMA-incorporated film. In contrast, we do not observe similarly large variations in the PL peak positions for the control films, Ctrl 80/20 (Figure 2b) and Ctrl 67/33 (Figure 2c). Furthermore, we quantify the variations in the local PL peak positions using the *median absolute deviation* metric, which provides the median of the absolute deviation of individual data points

from the sample median. Median absolute deviation is more robust against outliers compared to mean and standard deviation.<sup>37</sup> Figure 2d shows the median absolute deviation of the PL peak positions for different DMA incorporated and control thin films. DMA10 films have a 1.5x higher median absolute deviation compared to the control films, quantifying the higher local PL variations in individual DMA incorporated films compared to Ctrl 67/33 and Ctrl 80/20 thin films. This result is consistent with the visual observations made from Figures 2a-c and is strong evidence for the presence of underlying local compositional variations in the DMA10 thin films.

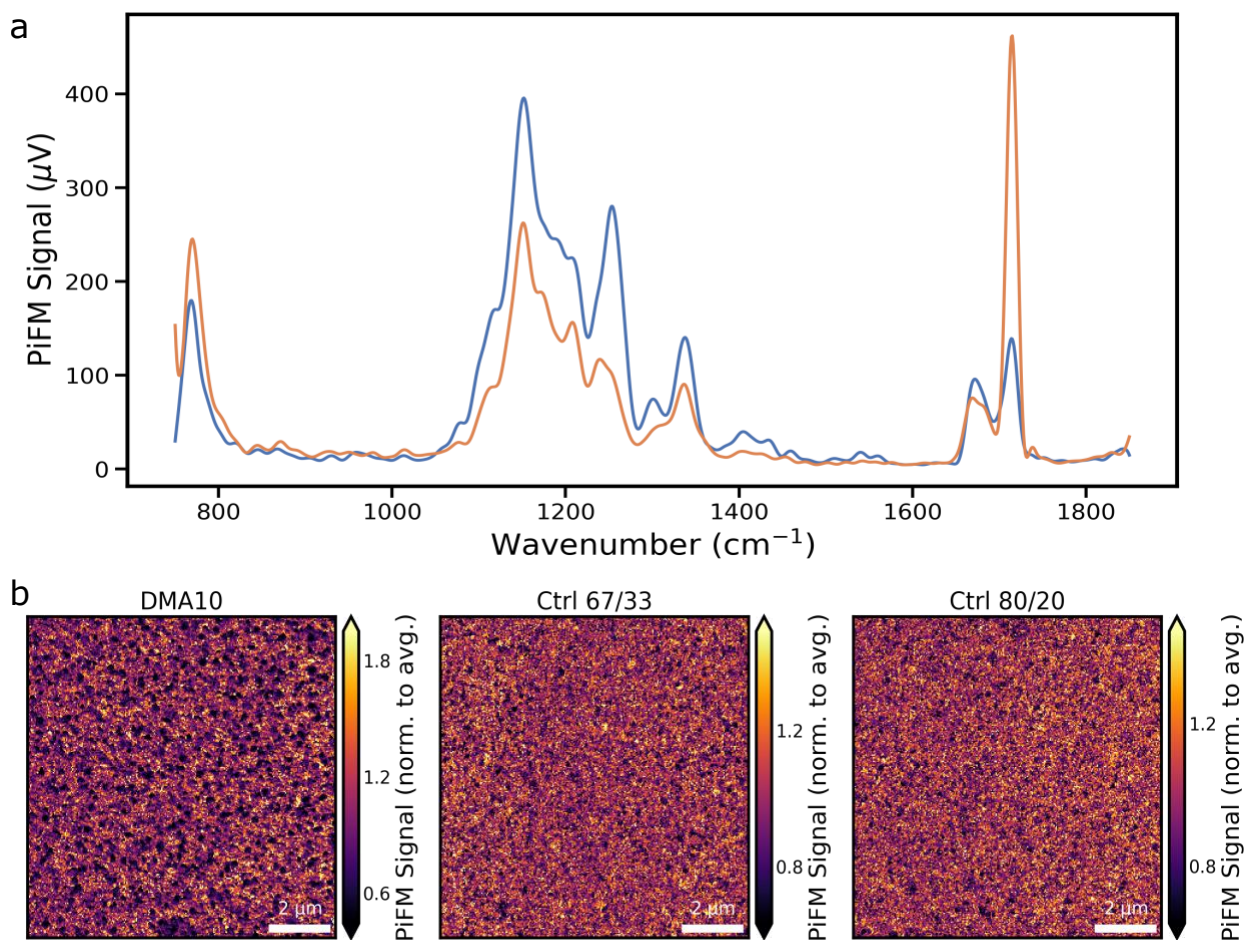


**Figure 3.3. Photo-induced force microscopy (PiFM) of DMA10 thin films. (a) PiFM spectra of two regions on a representative DMA10 thin film showing large variations in the peak at  $1714 \text{ cm}^{-1}$ , corresponding to FA. (b) PiFM image of DMA10, Ctrl 67/33 and Ctrl 80/20 films acquired at  $1714 \text{ cm}^{-1}$ , tracking local FA composition. The PiFM signal is normalized to the individual sample average.**

### 3.5. Photo-induced Force Microscopy

In order to confirm the presence of compositional heterogeneity, and compare the films with and without DMA, next we use photo-induced force microscopy (PiFM) to acquire nano-infrared (nanoIR) spectral maps of the films. PiFM uses a tunable IR laser to probe the local chemical vibrations in the material and has been used to study the local composition of organic and inorganic molecules.<sup>36,38–40</sup> Here, we aim to probe the local composition of the organic cations in the DMA10 film. Figure 3a shows the PiFM spectra for two different regions in a representative DMA10 film. From the PiFM spectra, we observe the largest variations in PiFM signal intensity at the 1714  $\text{cm}^{-1}$  wavenumber, corresponds to the C=N stretch in FA. We then use the 1714  $\text{cm}^{-1}$  FA peak to image the local FA composition in DMA10 and control films. Figure 3b shows the local FA composition for representative DMA10 and control thin films. We observe that the DMA10 films (Figure 3b) have distinct regions of high and low PiFM signal, corresponding to high and low FA concentration, respectively. The spatial variations in FA composition are greater in DMA10 thin films compared to the Ctrl 80/20 and Ctrl 67/33 thin films (Figure 3b). These observations are consistent across samples from different batches (Figure S10). Figure S11 shows a higher spatial resolution PiFM image at 1714  $\text{cm}^{-1}$  for a DMA10 film. We observe that there are entire domains with relatively lower FA signals than their neighboring regions, indicating a significant level of local FA heterogeneity introduced with DMA addition. We note that these local FA compositional variations observed in the DMA-incorporated samples are not simply due to the higher Cs loadings (Figure S12) in these films. We confirmed this conclusion by examining Ctrl 67/33 films which has an identical FA/Cs ratio and similar Cs loading to the DMA10 thin films; however, in these films we do not observe the same level of local FA heterogeneity as in the DMA10 samples (Figure S12). Together, these results indicate that the addition of DMA plays an important role in influencing the local chemical compositional heterogeneity. In other words, the addition of DMA leads to more heterogenous FA distribution in the thin film.

### 3.6. Conclusion

In conclusion, we show that the films cast from perovskite precursor solution containing DMA leads to DMA incorporation in the resulting thin film. We also demonstrate that DMA incorporation is heterogenous, with a significant preferential enrichment of DMA at the film surface. This result would suggest that the higher efficiencies and greater stabilities of the DMA-incorporated films reported in the literature<sup>24,25</sup> arise at least in part, due to surface passivation from the DMA. Furthermore, using local PL spectra data, we elucidate that there are micron-scale compositional heterogeneity in DMA-incorporated films, with the PL peak position and FWHM varying  $\sim 2x$  more in DMA-treated films. We confirmed this heterogeneity with PiFM nanoIR imaging, finding clusters with significantly reduced FA concentration in the DMA-incorporated films. Together, these results suggest that while the use of large A-site cation such as DMA improves the device performance and overall operational stability, these positive effects come with deleterious side-effects of increased compositional heterogeneity. Similar observations of heterogenous incorporation have also been reported by Fenning and co-workers for smaller alkali metal, such as Rb, incorporation at the A-site.<sup>41</sup> Our observations are promising for the use of DMA as an additive, as it indicates that there is room for improving the current processing conditions that leads to more homogeneous chemical composition in the DMA incorporated films, that could lead to further improvements in the device performance and operations stability.

See Appendix B on page 81 for experiment procedures, fabrication and characterization details, supplementary figures.

## Acknowledgements

This material is based on the work primarily supported by the U.S. Department of Energy's Office of Energy Efficiency and Renewable Energy (EERE) under the Solar Energy Technology Office (SETO), Award Number DE-EE0008747. Part of this work was conducted at the Molecular Analysis Facility, a National Nanotechnology Coordinated Infrastructure site at the University of Washington which is supported in part by the National Science Foundation (grant NNCI-1542101), the University of Washington, the Molecular Engineering & Sciences Institute, and the Clean Energy Institute. SJ thanks Dan Graham at Molecular Analysis Facility at the University of Washington for his help with TOF-SIMS data collection and analysis.

## References

- (1) National Renewable Energy Laboratory Efficiency Chart 2020 <https://www.nrel.gov/pv/assets/pdfs/best-research-cell-efficiencies.20200925.pdf> (accessed Oct 22, 2020).
- (2) Stolterfoht, M.; Caprioglio, P.; Wolff, C. M.; Márquez, J. A.; Nordmann, J.; Zhang, S.; Rothhardt, D.; Hörmann, U.; Redinger, A.; Kegelmann, L.; et al. The Perovskite/Transport Layer Interfaces Dominate Non-Radiative Recombination in Efficient Perovskite Solar Cells. Preprint at <Http://Arxiv.Org/Abs/1810.01333>. **2018**.
- (3) Stolterfoht, M.; Grischek, M.; Caprioglio, P.; Wolff, C. M.; Gutierrez-Partida, E.; Peña-Camargo, F.; Rothhardt, D.; Zhang, S.; Raoufi, M.; Wolansky, J.; et al. How To Quantify the Efficiency Potential of Neat Perovskite Films: Perovskite Semiconductors with an Implied Efficiency Exceeding 28%. *Adv. Mater.* **2020**, 2000080. <https://doi.org/10.1002/adma.202000080>.
- (4) Rajagopal, A.; Yang, Z.; Jo, S. B.; Braly, I. L.; Liang, P. W.; Hillhouse, H. W.; Jen, A. K. Y. Highly Efficient Perovskite–Perovskite Tandem Solar Cells Reaching 80% of the Theoretical Limit in Photovoltage. *Adv. Mater.* **2017**, 29 (34), 1–10. <https://doi.org/10.1002/adma.201702140>.
- (5) DeQuilettes, D. W.; Jariwala, S.; Burke, S.; Ziffer, M. E.; Wang, J. T. W.; Snaith, H. J.; Ginger, D. S. Tracking Photoexcited Carriers in Hybrid Perovskite Semiconductors: Trap-Dominated Spatial Heterogeneity and Diffusion. *ACS Nano* **2017**, 11 (11), 11488–11496. <https://doi.org/10.1021/acsnano.7b06242>.
- (6) Mahesh, S.; Ball, J. M.; Oliver, R. D. J.; Mcmeekin, D. P.; Nayak, P. K.; Johnston, M. B.; Snaith, H. J. Revealing the Origin of Voltage Loss in Mixed-Halide Perovskite Solar Cells †. *This J. is Cite this Energy Environ. Sci* **2020**, 13, 258. <https://doi.org/10.1039/c9ee02162k>.

- (7) Jariwala, S.; Burke, S.; Dunfield, S.; Shallcross, C.; Taddei, M.; Wang, J.; Eperon, G. E.; Armstrong, N. R.; Berry, J. J.; Ginger, D. S. Approaching the Limits of Optoelectronic Performance in Mixed Cation Mixed Halide Perovskites by Controlling Surface Recombination. **2020**.
- (8) Stolterfoht, M.; Caprioglio, P.; Wolff, C. M.; Márquez, J. A.; Nordmann, J.; Zhang, S.; Rothhardt, D.; Hörmann, U.; Amir, Y.; Redinger, A.; et al. The Impact of Energy Alignment and Interfacial Recombination on the Internal and External Open-Circuit Voltage of Perovskite Solar Cells. *Energy Environ. Sci.* **2019**, *12* (9), 2778–2788. <https://doi.org/10.1039/c9ee02020a>.
- (9) Wang, J.; Fu, W.; Jariwala, S.; Sinha, I.; Jen, A. K.-Y.; Ginger, D. S. Reducing Surface Recombination Velocities at the Electrical Contacts Will Improve Perovskite Photovoltaics. *ACS Energy Lett.* **2018**, *4*, 222–227. <https://doi.org/10.1021/acsenergylett.8b02058>.
- (10) Braly, I. L.; Dequilettes, D. W.; Pazos-Outón, L. M.; Burke, S.; Ziffer, M. E.; Ginger, D. S.; Hillhouse, H. W. Hybrid Perovskite Films Approaching the Radiative Limit with over 90% Photoluminescence Quantum Efficiency. *Nat. Photonics* **2018**, *12* (6), 355–361. <https://doi.org/10.1038/s41566-018-0154-z>.
- (11) Rajagopal, A.; Stoddard, R. J.; Jo, S. B.; Hillhouse, H. W.; Jen, A. K.-Y. Overcoming the Photovoltage Plateau in Large Bandgap Perovskite Photovoltaics. *Nano Lett.* **2018**, *18* (6), 3985–3993. <https://doi.org/10.1021/acs.nanolett.8b01480>.
- (12) Correa-Baena, J.-P.; Tress, W.; Domanski, K.; Anaraki, E. H.; Turren-Cruz, S.-H.; Roose, B.; Boix, P. P.; Grätzel, M.; Saliba, M.; Abate, A.; et al. Identifying and Suppressing Interfacial Recombination to Achieve High Open-Circuit Voltage in Perovskite Solar Cells. *Energy Environ. Sci.* **2017**, *10* (5), 1207–1212. <https://doi.org/10.1039/C7EE00421D>.
- (13) Xu, J.; Boyd, C. C.; Yu, Z. J.; Palmstrom, A. F.; Witter, D. J.; Larson, B. W.; France, R. M.; Werner, J.; Harvey, S. P.; Wolf, E. J.; et al. Triple-Halide Wide-Band Gap Perovskites with Suppressed Phase Segregation for Efficient Tandems. *Science (80- )*. **2020**, *367* (6482), 1097–1104. <https://doi.org/10.1126/science.aaz5074>.
- (14) Jariwala, S.; Sun, H.; Adhyaksa, G. W. P.; Lof, A.; Muscarella, L. A.; Ehrler, B.; Garnett, E. C.; Ginger, D. S. Local Crystal Misorientation Influences Non-Radiative Recombination in Halide Perovskites. *Joule* **2019**, *3* (12), 3048–3060. <https://doi.org/10.1016/j.joule.2019.09.001>.
- (15) DeQuilettes, D. W.; Vorpahl, S. M.; Stranks, S. D.; Nagaoka, H.; Eperon, G. E.; Ziffer, M. E.; Snaith, H. J.; Ginger, D. S. Impact of Microstructure on Local Carrier Lifetime in Perovskite Solar Cells. *Science (80- )*. **2015**, *348* (6235), 683–686. <https://doi.org/10.1126/science.aaa5333>.
- (16) Stoddard, R. J.; Rajagopal, A.; Palmer, R. L.; Braly, I. L.; Jen, A. K.-Y.; Hillhouse, H. W. Enhancing Defect Tolerance and Phase Stability of High-Bandgap Perovskites via Guanidinium Alloying. *ACS Energy Lett.* **2018**, *3* (6), 1261–1268. <https://doi.org/10.1021/acsenergylett.8b00576>.

- (17) Eperon, G. E.; Hörantner, M. T.; Snaith, H. J. Metal Halide Perovskite Tandem and Multiple-Junction Photovoltaics. *Nat. Rev. Chem.* **2017**, *1*, 0095. <https://doi.org/10.1038/s41570-017-0095>.
- (18) Barker, A. J.; Sadhanala, A.; Deschler, F.; Gandini, M.; Senanayak, S. P.; Pearce, P. M.; Mosconi, E.; Pearson, A. J.; Wu, Y.; Srimath Kandada, A. R.; et al. Defect-Assisted Photoinduced Halide Segregation in Mixed-Halide Perovskite Thin Films. *ACS Energy Lett.* **2017**, *2* (6), 1416–1424. <https://doi.org/10.1021/acseenergylett.7b00282>.
- (19) Slotcavage, D. J.; Karunadasa, H. I.; McGehee, M. D. Light-Induced Phase Segregation in Halide-Perovskite Absorbers. *ACS Energy Letters*. American Chemical Society December 9, 2016, pp 1199–1205. <https://doi.org/10.1021/acseenergylett.6b00495>.
- (20) Hoke, E. T.; Slotcavage, D. J.; Dohner, E. R.; Bowring, A. R.; Karunadasa, H. I.; McGehee, M. D. Reversible Photo-Induced Trap Formation in Mixed-Halide Hybrid Perovskites for Photovoltaics. *Chem. Sci.* **2015**, *6* (1), 613–617. <https://doi.org/10.1039/c4sc03141e>.
- (21) McMeekin, D. P.; Sadoughi, G.; Rehman, W.; Eperon, G. E.; Saliba, M.; Horantner, M. T.; Haghighirad, A.; Sakai, N.; Korte, L.; Rech, B.; et al. A Mixed-Cation Lead Mixed-Halide Perovskite Absorber for Tandem Solar Cells. *Science (80-. )*. **2016**, *351* (6269), 151–155. <https://doi.org/10.1126/science.aad5845>.
- (22) Saliba, M.; Matsui, T.; Seo, J. Y.; Domanski, K.; Correa-Baena, J. P.; Nazeeruddin, M. K.; Zakeeruddin, S. M.; Tress, W.; Abate, A.; Hagfeldt, A.; et al. Cesium-Containing Triple Cation Perovskite Solar Cells: Improved Stability, Reproducibility and High Efficiency. *Energy Environ. Sci.* **2016**, *9* (6), 1989–1997. <https://doi.org/10.1039/c5ee03874j>.
- (23) Saliba, M.; Matsui, T.; Domanski, K.; Seo, J. Y.; Ummadisingu, A.; Zakeeruddin, S. M.; Correa-Baena, J. P.; Tress, W. R.; Abate, A.; Hagfeldt, A.; et al. Incorporation of Rubidium Cations into Perovskite Solar Cells Improves Photovoltaic Performance. *Science (80-. )*. **2016**, *354* (6309), 206–209. <https://doi.org/10.1126/science.aah5557>.
- (24) Palmstrom, A. F.; Eperon, G. E.; Leijtens, T.; Prasanna, R.; Habisreutinger, S. N.; Nemeth, W.; Gaubing, E. A.; Dunfield, S. P.; Reese, M.; Nanayakkara, S.; et al. Enabling Flexible All-Perovskite Tandem Solar Cells. *Joule* **2019**, *3* (9), 2193–2204. <https://doi.org/10.1016/j.joule.2019.05.009>.
- (25) Eperon, G. E.; Stone, K. H.; Mundt, L. E.; Schloemer, T. H.; Habisreutinger, S. N.; Dunfield, S. P.; Schelhas, L. T.; Berry, J. J.; Moore, D. T. The Role of Dimethylammonium in Bandgap Modulation for Stable Halide Perovskites. *ACS Energy Lett.* **2020**, 1856–1864. <https://doi.org/10.1021/acseenergylett.0c00872>.
- (26) Goldschmidt, V. M. Die Gesetze Der Krystallochemie. *Naturwissenschaften* **1926**, *14* (21), 477–485. <https://doi.org/10.1007/BF01507527>.

- (27) Correa-Baena, J. P.; Saliba, M.; Buonassisi, T.; Grätzel, M.; Abate, A.; Tress, W.; Hagfeldt, A. Promises and Challenges of Perovskite Solar Cells. *Science*. American Association for the Advancement of Science November 10, 2017, pp 739–744. <https://doi.org/10.1126/science.aam6323>.
- (28) deQuilletes, D. W.; Zhang, W.; Burlakov, V. M.; Graham, D. J.; Leijtens, T.; Osherov, A.; Bulović, V.; Snaith, H. J.; Ginger, D. S.; Stranks, S. D. Photo-Induced Halide Redistribution in Organic–Inorganic Perovskite Films. *Nat. Commun.* **2016**, *7* (May), 11683. <https://doi.org/10.1038/ncomms11683>.
- (29) Schelhas, L. T.; Li, Z.; Christians, J. A.; Goyal, A.; Kairys, P.; Harvey, S. P.; Kim, D. H.; Stone, K. H.; Luther, J. M.; Zhu, K.; et al. Insights into Operational Stability and Processing of Halide Perovskite Active Layers †. **2019**. <https://doi.org/10.1039/c8ee03051k>.
- (30) Sanehira, E. M.; Marshall, A. R.; Christians, J. A.; Harvey, S. P.; Ciesielski, P. N.; Wheeler, L. M.; Schulz, P.; Lin, L. Y.; Beard, M. C.; Luther, J. M. Enhanced Mobility CsPbI<sub>3</sub> Quantum Dot Arrays for Record-Efficiency, High-Voltage Photovoltaic Cells. *Sci. Adv.* **2017**, *3* (10), eaao4204. <https://doi.org/10.1126/sciadv.aao4204>.
- (31) Harvey, S. P.; Li, Z.; Christians, J. A.; Zhu, K.; Luther, J. M.; Berry, J. J. Probing Perovskite Inhomogeneity beyond the Surface: TOF-SIMS Analysis of Halide Perovskite Photovoltaic Devices. *ACS Appl. Mater. Interfaces* **2018**, *10* (34), 28541–28552. <https://doi.org/10.1021/acsami.8b07937>.
- (32) Muramoto, S.; Graham, D. J.; Wagner, M. S.; Lee, T. G.; Moon, D. W.; Castner, D. G. ToF-SIMS Analysis of Adsorbed Proteins: Principal Component Analysis of the Primary Ion Species Effect on the Protein Fragmentation Patterns. *J. Phys. Chem. C* **2011**, *115* (49), 24247–24255. <https://doi.org/10.1021/jp208035x>.
- (33) Wagner, M. S.; Graham, D. J.; Castner, D. G. Simplifying the Interpretation of ToF-SIMS Spectra and Images Using Careful Application of Multivariate Analysis. *Appl. Surf. Sci.* **2006**, *252* (19), 6575–6581. <https://doi.org/10.1016/j.apsusc.2006.02.073>.
- (34) Wagner, M. S.; Tyler, B. J.; Castner, D. G. Interpretation of Static Time-of-Flight Secondary Ion Mass Spectra of Adsorbed Protein Films by Multivariate Pattern Recognition. *Anal. Chem.* **2002**, *74* (8), 1824–1835. <https://doi.org/10.1021/ac0111311>.
- (35) Tidwell, C. D.; Castner, D. G.; Golledge, S. L.; Ratner, B. D.; Meyer, K.; Hagenhoff, B.; Benninghoven, A. Static Time-of-Flight Secondary Ion Mass Spectrometry and x-Ray Photoelectron Spectroscopy Characterization of Adsorbed Albumin and Fibronectin Films. *Surf. Interface Anal.* **2001**, *31* (8), 724–733. <https://doi.org/10.1002/sia.1101>.
- (36) Kong, J.; Giridharagopal, R.; Harrison, J. S.; Ginger, D. S. Identifying Nanoscale Structure-Function Relationships Using Multimodal Atomic Force Microscopy, Dimensionality Reduction, and Regression Techniques. *J. Phys. Chem. Lett.* **2018**, *9* (12), 3307–3314. <https://doi.org/10.1021/acs.jpcllett.8b01003>.

- (37) Leys, C.; Ley, C.; Klein, O.; Bernard, P.; Licata, L. Detecting Outliers: Do Not Use Standard Deviation around the Mean, Use Absolute Deviation around the Median. *J. Exp. Soc. Psychol.* **2013**, *49* (4), 764–766. <https://doi.org/10.1016/j.jesp.2013.03.013>.
- (38) Bischak, C. G.; Flagg, L. Q.; Yan, K.; Rehman, T.; Davies, D. W.; Quezada, R. J.; Onorato, J. W.; Luscombe, C. K.; Diao, Y.; Li, C. Z.; et al. A Reversible Structural Phase Transition by Electrochemically-Driven Ion Injection into a Conjugated Polymer. *J. Am. Chem. Soc.* **2020**, *142* (16), 7434–7442. <https://doi.org/10.1021/jacs.9b12769>.
- (39) Jahng, J.; Fishman, D. A.; Park, S.; Nowak, D. B.; Morrison, W. A.; Wickramasinghe, H. K.; Potma, E. O. Linear and Nonlinear Optical Spectroscopy at the Nanoscale with Photoinduced Force Microscopy. *Acc. Chem. Res.* **2015**, *48* (10), 2671–2679. <https://doi.org/10.1021/acs.accounts.5b00327>.
- (40) Jahng, J.; Park, S.; Morrison, W. A.; Kwon, H.; Nowak, D.; Potma, E. O.; Lee, E. S. Nanoscale Spectroscopic Studies of Two Different Physical Origins of the Tip-Enhanced Force: Dipole and Thermal. **2017**.
- (41) Correa-Baena, J.-P.; Luo, Y.; Brenner, T. M.; Snaider, J.; Sun, S.; Li, X.; Jensen, M. A.; Titan, N.; Hartono, P.; Nienhaus, L.; et al. *Homogenized Halides and Alkali Cation Segregation in Alloyed Organic-Inorganic Perovskites Downloaded From*; 2019; Vol. 363.

# Chapter 4. Reducing Surface Recombination Velocity of MA-free Mixed Cation Mixed Halide Perovskites via Surface Passivation

## 4.1. Overview

We control surface recombination in the mixed-cation, mixed-halide perovskite,  $\text{FA}_{0.83}\text{Cs}_{0.17}\text{Pb}(\text{I}_{0.85}\text{Br}_{0.15})_3$  by passivating non-radiative defects with the polymerizable Lewis base (3-aminopropyl)trimethoxysilane (APTMS). We demonstrate average minority carrier lifetimes  $> 4 \mu\text{s}$ , nearly single exponential monomolecular PL decays, and high external photoluminescence quantum efficiencies ( $>20\%$ , corresponding to  $\sim 97\%$  of the maximum theoretical quasi-Fermi-level splitting) at low excitation fluence. We confirm both the composition and valence band edge position of the  $\text{FA}_{0.83}\text{Cs}_{0.17}\text{Pb}(\text{I}_{0.85}\text{Br}_{0.15})_3$  perovskite using multi-institution, cross-validated, XPS and UPS measurements. We extend the APTMS surface passivation to higher bandgap double cation (FA,Cs) compositions (1.7 eV, 1.75 eV and 1.8 eV) as well as the widely used triple cation (FA,MA,Cs) composition. Finally, we demonstrate that the average surface recombination velocity (SRV) decreases from  $\sim 1000 \text{ cm/s}$  to  $\sim 10 \text{ cm/s}$  post APTMS passivation for  $\text{FA}_{0.83}\text{Cs}_{0.17}\text{Pb}(\text{I}_{0.85}\text{Br}_{0.15})_3$ . Our results demonstrate that surface-mediated recombination is the primary non-radiative loss pathway in many MA-free mixed-cation mixed-halide films with a range of different bandgaps, which is a problem observed for a wide range of perovskite active layers and reactive electrical contacts. Our study also provides insights to develop passivating molecules that help reduce surface recombination in MA-free mixed-cation mixed-halide films and indicates that surface passivation and contact engineering will enable near-theoretical device efficiencies with these materials.

## 4.2. Introduction

Over the last decade, halide perovskites have made rapid gains in power conversion efficiency (PCE), with the current single-junction PCE record at 25.5% and the perovskite/Si 2-terminal tandem at 29.2%.<sup>1</sup> Much of this improvement in materials performance can be attributed to cation and anion engineering<sup>2–11</sup> on the A and X site of the  $\text{ABX}_3$  perovskite structure, respectively. However, despite the wide range of cation combinations available, the majority of the best performing single-junction and tandem perovskite solar cells reported to date incorporate some fraction of methylammonium (MA) in the A-site.<sup>2,3,5,6,11–16</sup> While MA-incorporation may help with performance, it has also been linked to instability at elevated temperatures due to methylamine sublimation.<sup>17,18</sup> Although new encapsulation strategies can enable stable MA

incorporated devices,<sup>19–21</sup> few high-performing devices in the literature have explored completely MA-free compositions, though there are increasing efforts focusing in that direction.<sup>8,22</sup>

Regardless of the perovskite composition, non-radiative recombination occurring at the surfaces and interfaces (both grain boundaries and the contact layer/perovskite interface) is one of the factors preventing devices from attaining near-theoretical efficiencies.<sup>23–30</sup> Surface passivation<sup>15,23,26,31–33</sup> and interfacial surface and strain engineering<sup>13,14,24,34–38</sup> have been proposed as ways to reduce non-radiative recombination. In these 3D perovskites, termination of the lattice along any low index face, at the surface of the crystal, at interfaces with electrical contacts, or at misaligned crystal (grain) boundaries, all expose under-coordinated metal sites, halide vacancies, and in general, regions which depart from the bulk stoichiometry and which are energetically distinct (providing potential mid-gap states) and potential recombination sites. Lewis bases of varying strengths can provide mitigation and passivation of these interfacial states.<sup>15,27,31,32</sup>

For instance, surface passivation with tri-octyl phosphine oxide (TOPO) on the archetypal  $\text{CH}_3\text{NH}_3\text{PbI}_3$  has demonstrated quasi-Fermi level splitting (QFLS) >97% of the radiative limit, rivaling that of GaAs,<sup>26</sup> and surface recombination velocities (SRV) <10 cm/s.<sup>23</sup> This suggests that non-radiative recombination at the surfaces can be mitigated with appropriate surface passivation. However, we have found that TOPO passivation is not as effective for FA-containing perovskites as it is for  $\text{CH}_3\text{NH}_3\text{PbI}_3$  (Figure S1, S2). We speculate these differences may be due to different surface terminations for MA and MA-free compositions, and/or the result of intrinsically different kinds of surface defects/near surface strain predominating due to the different compositions or growth mechanisms. For instance, it could be that halide vacancies dominate MAPI, and a mixture of halide vacancies or ammonium vacancies exist in MA-Free compositions.<sup>39–46</sup> These differences could play a role in deciding which surface passivating molecules have the most impact. Moreover, as shown previously, TOPO and many readily available surface-passivating molecules such as ODT (octadecanethiol) are labile and can be removed from the surface after deposition.<sup>31</sup>

Consequently, there is a need to develop passivation strategies that both works well across perovskite compositions and are also compatible with processing at scale. Ideally, these strategies should target molecules which simultaneously: (1) passivate surface defects, enabling ideal radiative performance of the semiconductor; (2) remain stable to subsequent vacuum or solution processing (perhaps by crosslinking); (3) are in principle scalable; and (4) permit effective charge extraction. However, since there is limited proof-of-concept for even meeting criteria (1), (2), and (3) simultaneously, here, we address meeting those criteria. Specifically, herein we explore the use of (3-aminopropyl) trimethoxy silane (APTMS), a Lewis base that can be cross-linked and polymerized in the presence of moisture<sup>47–49</sup>, to passivate 4 different FA-Cs/I-Br Pb perovskites with bandgaps ranging from 1.63 to 1.80 eV as well as the widely used triple cation perovskite ( $\text{FA}_{0.83}\text{MA}_{0.17}\text{Cs}_{0.05}\text{Pb}(\text{I}_{0.83}\text{Br}_{0.17})_3$ ). We demonstrate an enhancement in photoluminescence quantum efficiency (PLQE), photoluminescence (PL) lifetimes, and concomitantly low SRV at interfaces, indicating the ability of this agent to passivate defects in a range of perovskite compositions. Moreover, for the case of 1.63 eV-bandgap FA-Cs/I-Br perovskite, we demonstrate a ~10x average PL lifetime improvement and a champion PL lifetime of 4.3  $\mu\text{s}$ . Together with the increase in PL lifetime, we also observe an increase in the external PLQE to a record 20.1% at 70  $\text{mW}/\text{cm}^2$  for APTMS surface passivated films. This PLQE corresponds to QFLS that is ~97% of the maximum QFLS obtained using the Shockley-Queisser (SQ) model. We note that such high

PLQE and QFLS have not previously been reported in MA-free mixed-halide 3-D perovskites. Furthermore, we use X-ray photoelectron spectroscopy (XPS) and glow discharge optical emission spectroscopy (GDOES) to demonstrate that APTMS interacts as a surface modifier with terminal amines acting as a combination of Lewis base and protonated amine. Lastly, we investigate the impact of passivation on the SRV in FA-Cs/I-Br films. We demonstrate that APTMS-passivated films can achieve SRVs  $<10$  cm/s compared to control films with  $\sim 1000$  cm/s. These results suggest that non-MA based perovskite compositions can achieve higher performance by tailoring the surface chemistry to minimize non-radiative recombination.

### 4.3. Surface passivation beyond MA based halide perovskites

To start, we fabricate 400 nm thick films of  $\text{FA}_{0.83}\text{Cs}_{0.17}\text{Pb}(\text{I}_{0.85}\text{Br}_{0.15})_3$  (hereafter referred to as Cs17Br15 for brevity) on glass using a method adopted from Kim *et al.* (see Appendix C for more details).<sup>22</sup> We confirm the perovskite structure using X-ray diffraction (XRD) (Figure S3) and bandgap of 1.63 eV using UV-Vis (Figure S4). Moreover, using XPS, we show that the near-surface film composition is identical (within error margins) to the solution stoichiometry with a slight ( $\pm 2\%$ ) excess of  $\text{PbI}_2$  at the surface (Table S1). Additionally, using UV photoelectron spectroscopy (UPS) and XPS, we determine the ionization potential (IP) for the Cs17Br15 composition to be 5.64 eV, from which we extrapolate the electron affinity (EA) of 4.01 eV (Figure 4.1a). Importantly, we also verified that these surface composition and band edge positions are reproducible both after shipping, and upon fabricating devices at multiple institutions, providing cross validation of sample shipping, fabrication, and XPS/UPS measurement protocols (see APPENDIX C for more details on multi-institutional cross verification and shipping).

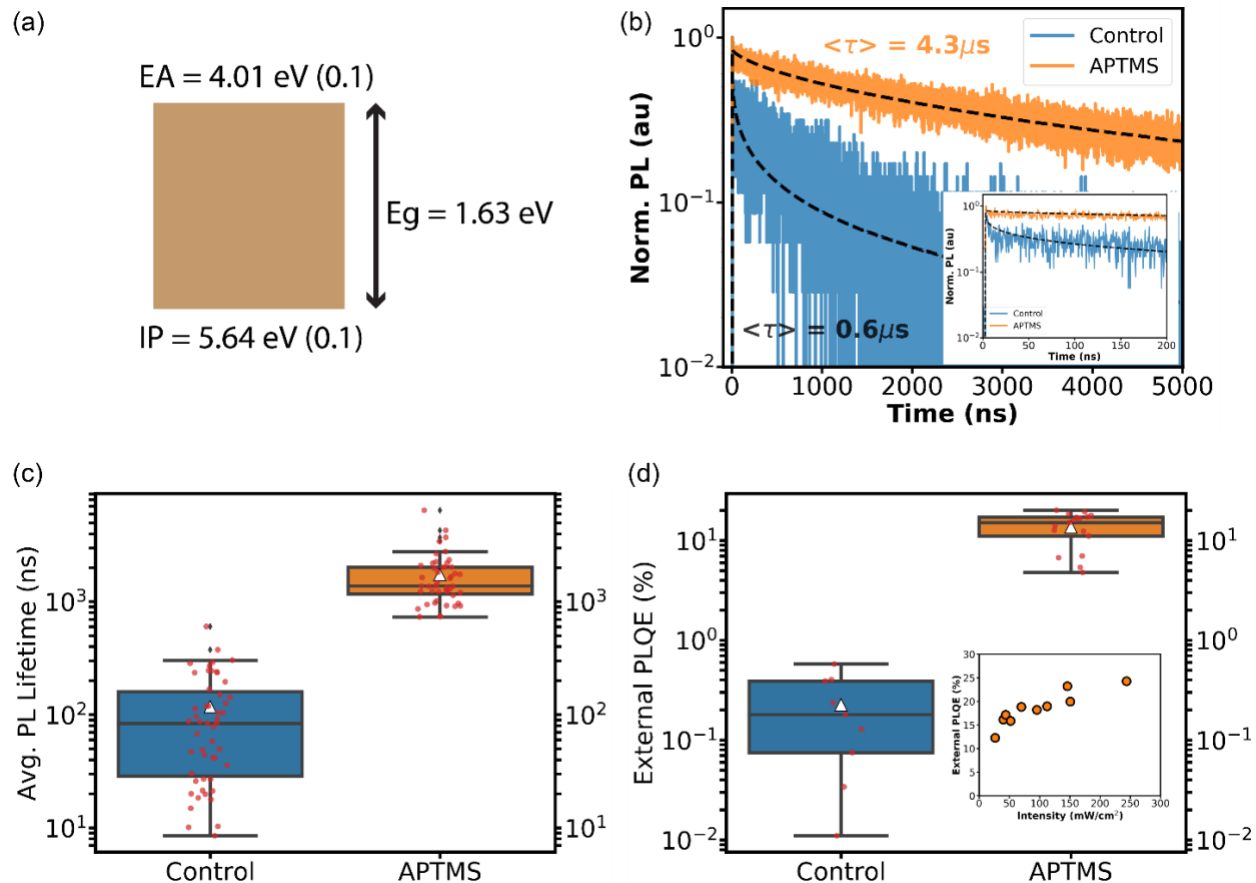


**Figure 4.1 – Surface passivation beyond MA based halide perovskites. (a) Valence band maximum and conduction band minimum for Cs<sub>17</sub>Br<sub>15</sub> perovskite showing electron affinity (EA) and ionization potential (IP). See Figure S5 for valence band photoemission spectra. (b) Time-resolved PL decay of a control and APTMS surface-passivated Cs<sub>17</sub>Br<sub>15</sub> perovskite film. The dashed black lines denote the fitted PL lifetime according to Equation S2. The inset shows the early time decays for the control and APTMS passivated film. (c) Boxplot of average PL lifetime ( $\langle \tau \rangle$ ) for control (n=51) and APTMS passivated Cs<sub>17</sub>Br<sub>15</sub> films (n=47). (d) Boxplot of external PLQE for control (n=9) and APTMS passivated Cs<sub>17</sub>Br<sub>15</sub> films (n=17) measured at 70 mW/cm<sup>2</sup> using a 532 nm CW laser. The inset shows the external PLQE measured as a function of intensity for a typical APTMS passivated Cs<sub>17</sub>Br<sub>15</sub> film. APTMS passivated samples retain high PLQE at low illumination intensities, even as low as ~0.01 suns (Figure S6). The boxes in (c) and (d) shows the quartiles of the data and the whiskers extend to capture the rest of the distribution. The white triangle denotes the average of the distribution in both (c) and (d). The red scatter points are the individual data points.**

In order to passivate the surface of the Cs<sub>17</sub>Br<sub>15</sub> films, we expose them to APTMS vapor in a controlled environment (see SI) and study the impact on PL. Figure 4.1b shows the PL decay of a control and APTMS surface passivated Cs<sub>17</sub>Br<sub>15</sub> film acquired using a 470 nm pulsed laser excitation at 50 nJ/cm<sup>2</sup> per pulse (a relatively low fluence, where the trap density is often higher than the photocarrier density<sup>28,50</sup>). To analyze the data, we fit the time resolved PL decays to the stretched exponential decay function (see Appendix C for further details). Before surface passivation, the PL lifetimes (average  $\langle \tau \rangle$ ) of the control samples are hundreds of ns (control<sub>avg</sub> =

117 ns), indicating the good quality of our control Cs17Br15 thin films.<sup>22</sup> After APTMS surface passivation, we observe a ~15x improvement in PL lifetime ( $\text{APTMS}_{\text{avg}} = 1.75 \mu\text{s}$ ), as shown by the average lifetime box plots for 50 separate Cs17Br15 films from different batches in Figure 4.1c. We observe an improvement in average PL lifetime ( $\langle\tau\rangle$ ) from 0.6  $\mu\text{s}$  for the champion control Cs17Br15 film to 4.3  $\mu\text{s}$  for the champion APTMS passivated film. As expected, the characteristic lifetime ( $\tau_c$ ) also increases from 0.056  $\mu\text{s}$  for the control to 2.95  $\mu\text{s}$  for the surface passivated film and  $\beta$  also increases from 0.29 to 0.62. These data show the APTMS surface treatment modifies surface mediated non-radiative recombination and also suggest that the relaxation rate becomes more homogeneous with APTMS passivation, as the increase in the  $\beta$  value is indicative of more mono-exponential, less distributed, kinetics. Along with the increase in the PL lifetimes, we also observe an increase in the external PLQE with APTMS passivation. Figure 4.1d shows the external PLQE for films before and after passivation measured at an incident excitation intensity of 70  $\text{mW}/\text{cm}^2$  using a 532 nm CW laser (see Appendix C for details). On average, we observe a ~60x increase in the external PLQE from 0.23% for the control to 13.64% for the passivated film, with the highest external PLQE of 20.1% at 70  $\text{mW}/\text{cm}^2$  for APTMS passivated Cs17Br15 films. To our knowledge, this is the highest reported external PLQE for MA-free mixed-cation mixed-halide perovskites. We further note that the APTMS-passivated Cs17Br15 films retain high PLQE at low illumination intensities (Figure 4.1d inset), even as low as ~0.01 suns (Figure S6). Additionally, external PLQE can be used to evaluate QFLS within the film according to the equation by Ross.<sup>51</sup> Our group<sup>26</sup> and others<sup>52-54</sup> have used it to evaluate QFLS in semiconductor thin films. Using the Ross equation, we calculate a 1.31 eV QFLS, i.e. ~97% of the theoretical SQ limit (see SI), obtained at 70  $\text{mW}/\text{cm}^2$  (~1 sun condition) for APTMS passivated Cs17Br15 (see Appendix C for details). This result further demonstrates that with surface passivation, FA-Cs/I-Br based perovskites can achieve similar thin-film optoelectronic qualities without the need for MA inclusion.<sup>26,27</sup> These results also then indicate that the use of MA may impact the surface defect type and density and thus, the overall nonradiative recombination rate for typical thin-film processing routes.

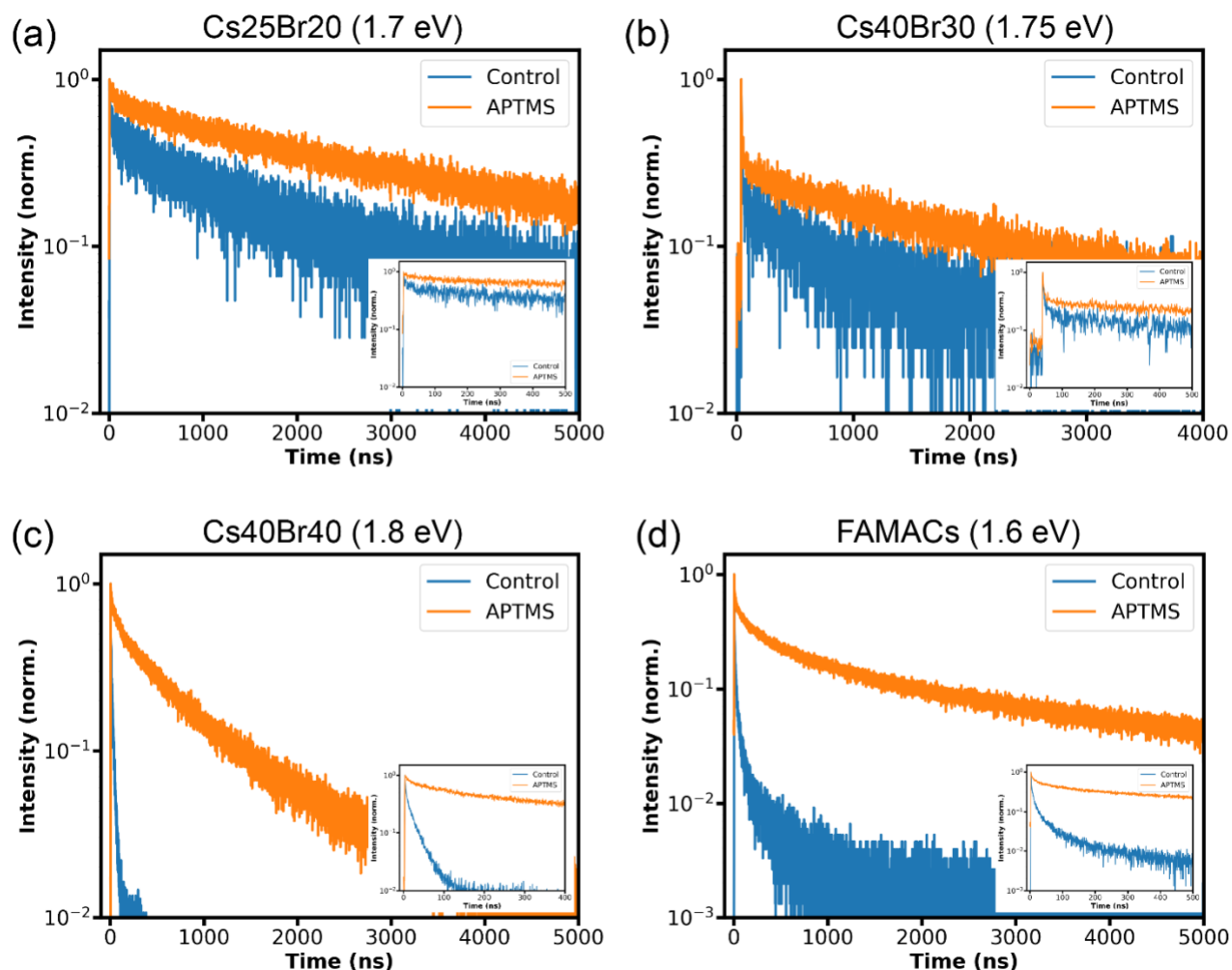


**Figure 4.2-** Surface passivation for different bandgap MA-free perovskite compositions and triple cation compositions. Time-resolved PL decay of control and APTMS passivated (a) Cs<sub>25</sub>Br<sub>20</sub> (~1.7 eV), (b) Cs<sub>40</sub>Br<sub>30</sub> (~1.75 eV), (c) Cs<sub>40</sub>Br<sub>40</sub> (~1.8 eV), and (d) (FA<sub>0.83</sub>MA<sub>0.17</sub>)<sub>0.95</sub>Cs<sub>0.05</sub>Pb(I<sub>0.83</sub>Br<sub>0.17</sub>)<sub>3</sub> or FAMACs-IBr (~1.6 eV) perovskite thin films.

## 4.4. Surface passivation for different bandgap MA-free perovskite

Next, we investigate the effects of surface passivation on the widely used triple-cation mixed-halide perovskite,<sup>2</sup> (FA<sub>0.83</sub>MA<sub>0.17</sub>)<sub>0.95</sub>Cs<sub>0.05</sub>Pb(I<sub>0.83</sub>Br<sub>0.17</sub>)<sub>3</sub>, (hereafter FAMACs/I-Br) and other higher bandgap perovskite thin films (without MA) potentially relevant for Si/perovskite tandems and perovskite/perovskite tandems (1.7 eV, 1.75 eV, 1.81 eV).<sup>55</sup> We tune the Cs and Br composition to tune the bandgap using a method adopted from Bush *et al.*<sup>56</sup> (see Appendix C for details). More specifically, we fabricate FA<sub>0.75</sub>Cs<sub>0.25</sub>Pb(I<sub>0.80</sub>Br<sub>0.20</sub>)<sub>3</sub> [Cs<sub>25</sub>Br<sub>20</sub>] (E<sub>g</sub> ~1.7 eV), FA<sub>0.60</sub>Cs<sub>0.40</sub>Pb(I<sub>0.70</sub>Br<sub>0.30</sub>)<sub>3</sub> [Cs<sub>40</sub>Br<sub>30</sub>] (E<sub>g</sub> ~1.75 eV), and FA<sub>0.60</sub>Cs<sub>0.40</sub>Pb(I<sub>0.60</sub>Br<sub>0.40</sub>)<sub>3</sub> [Cs<sub>40</sub>Br<sub>40</sub>] (E<sub>g</sub> ~1.81 eV) thin films and confirm the bandgap and structure of the fabricated films using UV-Vis (Figure S4) and XRD (Figure S3), respectively. Figures 4.2 a, b, and c show the PL decay

before passivation (control) and after APTMS passivation for Cs25Br20, Cs40Br30, and Cs40Br40 films, respectively. Figure 4.2d shows the PL decay for the FAMACs/I-Br before and after surface passivation. We observe an increase in the PL lifetime and the integrated PL intensity (Figure S7, S8) upon APTMS treatment for all the different bandgaps and compositions (see Note S1 for additional discussion). For Cs25Br20 thin films ( $E_g \sim 1.7\text{eV}$ ), we find that at  $\sim 1$  sun intensity the highest external PLQE increases by over 10X from 0.23% for control to 3.5% for APTMS passivated (Figure S9), which is one of the highest for FACs mixed halide films compared to literature.<sup>57</sup> Moreover, the increase in PL lifetime tends to track with the increase in silane deposition time (Figure S10) and can also be achieved through solution processing (Figure S11). We also note that silane passivation works on archetypal  $\text{CH}_3\text{NH}_3\text{PbI}_3$  (Figure S12). These results further demonstrate the versatility of the silane deposition for passivation. We also note that after depositing a transport layer on top of APTMS, the passivated film retains PL improvements relative to control film (Figure S13), suggesting that the perovskite film continues to benefit from the APTMS passivation after subsequent processing.

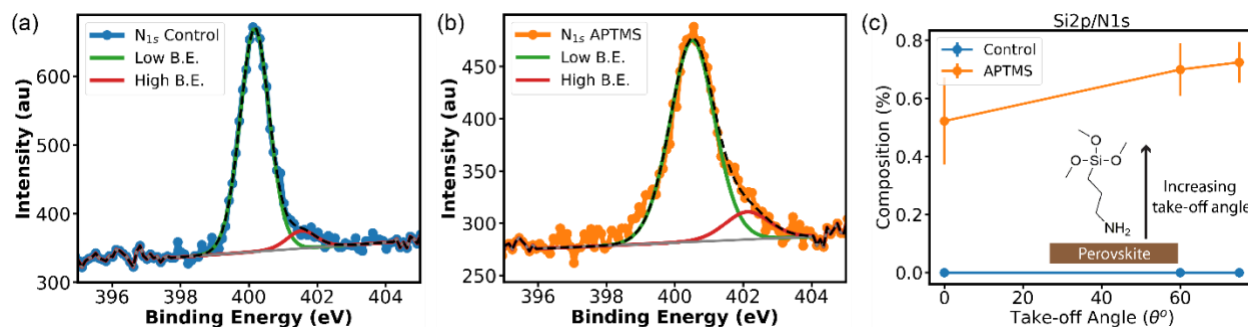


**Figure 4.3 - High resolution and angle-resolved X-ray photoelectron spectroscopy (XPS).** High-resolution XPS of N 1s for (a) Cs17Br15 control and (b) APTMS passivated film. The dashed black line represents the envelope of the signal and the gray line represents the background. (c)  $\text{Si}_{2p}/\text{N}_{1s}$  ratio as a function of different photoelectron take-off angle for control and APTMS passivated Cs17Br15 films. Increasing take-off angles represent more surface sensitivity. Error bars represent the standard deviation of the composition. The inset shows the schematic of APTMS orientation on perovskite surface.

## 4.5. High resolution and angle-resolved X-ray photoelectron spectroscopy

In order to better understand the general interaction between APTMS/silane and the perovskite surface, we use X-ray photoelectron spectroscopy (XPS). XPS provides information about the elements present, and their oxidation state, simultaneously. The XPS results, show an increase in the Si and O concentrations after APTMS passivation of Cs17Br15 films (Figure S14), consistent with the presence of APTMS on the surface. We also acquired elemental depth profiles using glow discharge optical emission spectroscopy (GDOES), which further confirm the presence of APTMS on the surface and demonstrate that APTMS acts primarily at the surface and does not permeate the film at detectable levels (Figure S15). Moreover, SEM images (Figure S16) show that the general morphology of the perovskite remains largely unchanged. However, it is

noteworthy that the silane layer does tend to reduce the SEM image clarity, so we cannot definitively exclude the possibility that some APTMS interacts preferentially with the domain/grain boundaries. Indeed, it is possible that exposure to the APTMS may help “clean out” grain boundaries, as has been proposed by Shallcross *et al.* during experiments on electrochemical etching of halide perovskites,<sup>58</sup> thus alleviating non-radiative recombination occurring at the grain boundaries. Nevertheless, the effect, dramatically increasing the PL lifetime and PLQY, is consistent with reduction of non-radiative recombination.

To further probe the interaction between APTMS and the perovskite, we acquire high-resolution XPS spectra for APTMS-passivated and control Cs17Br15 films. Figure 4.3a and 4.3b shows the spectra of N1s for the control and APTMS treated film, fitted with a low binding energy (LBE) and a high binding energy (HBE) N 1s peak. Both peak width broadening, and position shift are observed after the APTMS treatment, indicating that the N chemical bonding environment has changed. We attribute the control sample LBE and HBE N 1s peak to C-NH<sub>2</sub> and C=NH<sub>2</sub><sup>+</sup>, respectively.<sup>59</sup> On the other hand, the N 1s signal in silane-treated surfaces can be assigned to a variety of overlapping amine/ammonium species interactions.<sup>60</sup> Here, in APTMS passivated films, we attribute the LBE N 1s peak to the free amine and H-bond donor and the HBE N1s to a range of different species such as Lewis base, H-bond acceptor, and protonated amine; as suggested by Shallcross *et al.*<sup>60</sup> The binding energies are summarized in Table S2. We observe a higher fraction of the electron deficient HBE N 1s in APTMS treated sample (12.15%) compared to control sample (7.32%). In other words, there is 1.6x more HBE N 1s contribution to the overall N 1s signal for APTMS treated films, compared to the control N 1s signal. We attribute this increase in the contribution of the HBE N 1s peak to the APTMS treatment acting as a combination of Lewis base and protonated amine on Cs17Br15 films, as also observed in other silane/metal interactions.<sup>60</sup>

Next, to further understand the interaction between the APTMS and the surface of the perovskite film, we use angle resolved XPS to investigate the composition as a function of depth, allowing us to discern the average orientation of the silanes on the surface of the perovskite film. In this technique, the elemental composition is measured as a function of different photo-electron take-off angles, allowing depth resolution. Higher take-off angles represent more surface sensitivity (probing decreased film depth) and lower take-off angles represent more bulk sensitivity (probing increased film depth). Figure 4.3c shows the compositional ratio of Si<sub>2p</sub>/N<sub>1s</sub> as a function of take-off angle for APTMS passivated Cs17Br15 films. We observe an increase in the Si<sub>2p</sub>/N<sub>1s</sub> signal as a function of increasing take-off angle (decreasing film depth). In other words, we probe more Si<sub>2p</sub> signals, as opposed to N<sub>1s</sub>, at the very surface of the APTMS passivated Cs17Br15 films. As discussed above, the N<sub>1s</sub> signal after APTMS passivation originates mainly from the amine-perovskite interactions (Figure 4.3b), rather than from the FA species in the bulk perovskite (Figure 4.3a), such a Si<sub>2p</sub>/N<sub>1s</sub> depth profile indicates that the overall silane orientation is more upright with the terminal amines in the silane interacting with the defects at the surface (Figure 4.3b inset). In addition, as we move to grazing angles (decreasing film depth, increasing take-off angle), we observe a decrease in the N<sub>1s</sub>/C<sub>1s</sub> signal (Figure S17). Together, these N, C, and Si trends suggest both that the silane films are relatively compact, and that the *average* silane orientation is more upright (Figure 4.3c inset) with the terminal amines in the silane pointing downward (*i.e. interacting with the perovskite surface*). We note that while it is also possible that the O species in the methoxy groups also interact with the perovskite surface, the data suggest the average interaction is more N dominated (Figure S18). Such equivocality in silane arrangements

have also been observed in more-studied silane deposition on Si and oxide surfaces.<sup>61</sup> We note that the N, C, Si and O trends discussed also hold for all different Cs17Br15 samples passivated with silanes (Figure S17-S19). Moreover, we do not observe any specific trends in N 1s or C 1s signal for control films as a function of take-off angles (different surface depth sensitivity) (Figure S19). Together, the high-resolution and angle resolved XPS results confirm that the terminal amine primarily interacts with the perovskite surface, which we speculate occurs as a combination of Lewis base and protonated amine to passivate the defects. In other words, we propose that APTMS can bind to the halide vacancies as an amine/Lewis base ( $-\text{NH}_2$ )<sup>31</sup> and to the A-site vacancies as a protonated amine ( $-\text{NH}_3^+$ ). We hypothesize that if both Lewis base and protonated amines are required to fully passivate the MA-free perovskites surfaces, it would explain why APTMS is able to passivate the C17Br15 films much more effectively than pure Lewis Base donors like TOPO, which are able to passivate nearly 100% of halide-vacancy defects in MAPI films.<sup>26</sup>

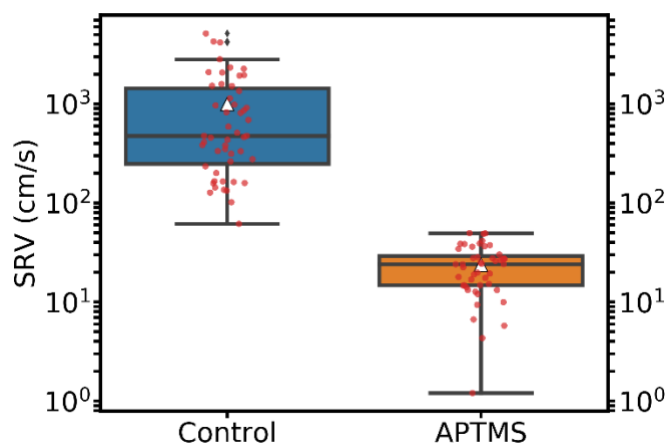


**Figure 4.4 – Surface recombination velocity (SRV) extracted from the PL lifetime data on Cs17Br15 films as discussed in the text. Boxplot of SRV for control and APTMS passivated Cs17Br15, for SRV=0 limit. The box shows the quartiles of the data and the whiskers extend to capture the rest of the distribution. The white triangle denotes the average of the distribution. The red scatter points are the individual data points.**

## 4.6. Surface recombination velocity (SRV)

Having demonstrated a method to alleviate the non-radiative recombination introduced at surfaces in non-MA based mixed halide perovskites, we turn to investigate its impact on SRV. SRV quantifies the rate of minority carrier recombination occurring at the surface of the semiconductor and is one of the parameters that defines non-radiative recombination occurring at the surfaces and interfaces in devices. For the purposes of our SRV discussion here, “surfaces” will refer to the top and bottom film surfaces, though we cannot exclude the possibility that low concentrations of APTMS are also penetrating the grain boundaries, which have also been shown to act as non-radiative recombination sites.<sup>28,62</sup> Reducing SRV has proved to be an important

parameter to improve the efficiency of established PV systems including Si,<sup>63,64</sup> GaAs,<sup>65</sup> CIGS<sup>66</sup> and CdTe.<sup>67</sup>

Early modeling, using literature values for the physical properties of CH<sub>3</sub>NH<sub>3</sub>PbI<sub>3</sub>, showed that SRVs  $\sim < 10$  cm/s will be required to approach the theoretical performance limit for perovskite PV.<sup>23</sup> While passivated and well-grown MA-based perovskite thin-films and single crystals have already been demonstrated with relatively low SRVs on the order of  $\sim 10$  cm/s,<sup>23,68,69</sup> while unpassivated MAPbBr<sub>3</sub> single crystals,<sup>70</sup> MAPbI<sub>3</sub> single crystals and thin films<sup>71</sup> commonly report much higher SRVs on the order of  $\sim 10^3$  cm/s.

Here, we use time-resolved PL measurements to investigate the minority carrier lifetime and the associated SRV in Cs17Br15 films. The average PL lifetime ( $\langle \tau \rangle$ ) as given by Eq. S3 for Cs17Br15 films is the effective minority carrier lifetime under low fluence. The relationship between effective lifetime ( $\tau_e$ ), bulk lifetime ( $\tau_b$ ), and surface lifetime ( $\tau_s$ )<sup>72</sup> is shown in SI. The bulk lifetime ( $\tau_b$ ) can be measured either in a single crystal or, in a case where all surface recombination is alleviated, and only bulk recombination remains (such that the internal PLQY approaches the radiative limit). Here, we use the latter approach and approximate the bulk lifetime to be 8  $\mu$ s.<sup>23,26</sup> We note that this is an estimate of the bulk lifetime as it is measured in surface passivated thin films which have internal PLQY greater than 90% and very small amounts of bulk non-radiative recombination left.<sup>26</sup> Further, this assumption is a conservative approach, as *underestimating* the bulk recombination rate (*i.e. overestimating* bulk lifetime) should lead to an overestimate of the extracted SRV. Using this bulk lifetime, we then use the approach described previously<sup>23</sup> (see Appendix C for full details) to estimate the SRV. Our results show that on average, control films exhibit SRV of  $\sim 1000$  cm/s while the same films, after surface passivation with APTMS, exhibit an average SRV of  $\sim 10$  cm/s, with a champion SRV value of 1 cm/s (Figure 4.4). We emphasize that under this approach, the SRV values we report are on the *higher* end of the limit as bulk lifetimes are likely overestimated and all recombination is assumed to occur at only one interface; *i.e.* this assumption ignores recombination occurring at the back interface.

Next, we use the calculated SRV values and idealized contacts with realistic transport properties to simulate the device performance using drift-diffusion simulations in SCAPS,<sup>73</sup> as described further in SI. Figure S20 shows the simulated J-V curve for SRV of  $10^3$  cm/s, 10 cm/s and 1 cm/s. We observe a  $>4\%$  absolute improvement in PCE as we vary the SRV from  $10^3$  cm/s down to 1 cm/s, demonstrating the importance of minimizing SRV at the perovskite/transport layer interfaces. As expected, the majority of the improvement in PCE is due to the improvement in the  $V_{OC}$  and fill factor (Figure S21). We note that the improvement in the simulated device performance due to a reduction in SRV is seen despite perfect energetic alignment of contact layers with the perovskite. Increasing the energy mismatch in transport layer alignment with the perovskite will adversely impact the PCE and  $V_{OC}$  (Figure S22) placing even more stringent demands on SRV. We note that the increased importance of SRV reported here (relative to earlier work by Wang *et al.*<sup>23</sup>) is due to our use of more realistic transport-layer properties such as mobility, etc. (see Appendix C for a complete list of SCAPS simulation parameters). These results only increase the importance of further reducing SRV.

## 4.7. Conclusion

In conclusion, we have used APTMS as a model compound to study its interaction with a variety of MA-free mixed cation halide perovskite interfaces, and the resulting optoelectronic properties. We demonstrated high-performing MA-free mixed cation and mixed halide perovskites with  $>4 \mu\text{s}$  PL lifetime and  $>20\%$  external PLQE achieved by facile surface passivation using a silane. The high PLQE corresponds to  $\sim 97\%$  of the theoretical QFLS; a first for non-MA based compositions. Importantly, we also demonstrate that the passivation approach works for a wide range of different compositions with different bandgaps, including the widely used triple cation composition,  $(\text{FA}_{0.83}\text{MA}_{0.17})_{0.95}\text{Cs}_{0.05}\text{Pb}(\text{I}_{0.83}\text{Br}_{0.17})_3$ . We note that the relative improvements post APTMS passivation are higher for Cs17Br15 compositions compared to higher Cs/Br compositions; likely due to higher bulk defect densities in the high Cs/Br compositions as APTMS primarily interacts with the surface. We used XPS and UPS to confirm the stoichiometry and investigate the band alignments of the perovskite compositions. Notably, we also demonstrate that the same XPS and UPS values can be obtained at multiple institutions with films prepared at, and transported between, different institutions, validating protocols for sample transport and surface analysis. In addition, with high-resolution XPS and angle-resolved XPS we investigate the nature of the interaction and the average orientation of APTMS on the perovskite surface. We find that, on average, the APTMS molecules primarily interact with the perovskite surface using the terminal amine group. We propose that APTMS binds to the halide vacancies as an amine ( $-\text{NH}_2$ ) and to the A-site vacancies as a protonated amine ( $-\text{NH}_3^+$ ). Lastly, we show the effects of APTMS passivation on the SRV and observe that the SRV decreases to  $\sim 10 \text{ cm/s}$  on average, with a champion low of  $\sim 1 \text{ cm/s}$  (note that this is the upper limit of the value). These are significant reductions in SRV: using SCAPS simulations,<sup>73,74</sup> such improvements in the SRV can translate to  $>4\%$  absolute enhancement in device PCE, even with perfectly aligned contacts. These possible increases are consistent with the significant gains in device performance recently reported for new surface passivation/hole transport layers.<sup>75</sup>

While our focus here is not on device studies, these results nevertheless demonstrate that non-radiative recombination at surfaces remains a major loss pathway for many as-grown compositions of mixed-cation perovskites. Taken together, the success of APTMS in surface passivation, the relative ineffectiveness of TOPO on MA-free mixed cation mixed halide perovskites, and the XPS data indicating the preferential interaction of the amine head group (possibly as a mixture of Lewis base and protonated amine), with the perovskite suggests that surface passivation of MA-free mixed-cation perovskites is likely more complicated than the passivation of classic MAPI formulations.

Since APTMS crosslinks and polymerizes into an insoluble and non-volatile film with moisture from ambient air,<sup>47-49</sup> it can be further exposed to solvents or vacuum experiments for subsequent studies. Future work should, thus, not only explore molecules with similar structural motifs to understand which molecular factors are critical for surface passivation but may also explore the use of APTMS in various device geometries. While the use of APTMS in traditional n-i-p or p-i-n solar cell geometry would likely need further thickness optimizations due to presumed insulating nature of APTMS, we propose that molecules like APTMS may still be useful in PERC-like<sup>76</sup> perovskite solar cells, either with self-assembled, or intentionally-patterned interfacial passivation between the perovskite and the HTL and ETL. Alternatively, the use of APTMS with an interdigitated back contact perovskite solar cell<sup>77,78</sup> could be another practical

option. Regardless, the data here provide guidance on what to look for while designing and optimizing new “passivating” layers and more importantly, they demonstrate that current perovskite thin film growth methods can already yield films with optoelectronic quality that can enable much higher potential performance than has to date not been realized in MA-free mixed cation (FA/Cs) mixed halide based devices.

*See Appendix C on page 96 for experiment, characterization and simulation details; tables containing composition and binding energies from XPS, simulation parameters; additional TRPL discussion; supplementary figures – TRPL, XRD, UV-Vis, XPS, UPS, PLQE, GDOES, SEM, SCAPS simulation.*

## Acknowledgements

This material is based upon work supported primarily by the U.S. Department of Energy’s Office of Energy Efficiency and Renewable Energy (EERE) under the Solar Energy Technology Office (SETO), Award Number DE-EE0008747. Part of this work was conducted at the Molecular Analysis Facility, a National Nanotechnology Coordinated Infrastructure site at the University of Washington which is supported in part by the National Science Foundation (grant NNCI-1542101), the University of Washington, the Molecular Engineering & Sciences Institute, and the Clean Energy Institute. SJ thanks Gerry Hammer at Molecular Analysis Facility for help with XPS measurements and analysis and Yangwei Shi for experimental help. Research support for work performed at the University of Arizona was provided by the Office of Naval Research ONR: N00014-18-1-2711 and ONR N00014-20-1-2440. Contributions from JJB and SPD were undertaken at the National Renewable Energy Laboratory, operated by Alliance for Sustainable Energy, LLC, for the U.S. Department of Energy (DOE) under Contract No. DE-AC36-08GO28308 efforts here were supported by the U.S. Department of Energy’s Office of Energy Efficiency and Renewable Energy (EERE) under the Solar Energy Technologies Office (SETO) project “De-risking Halide Perovskite Solar Cells” program (DE-FOA-0000990). The views expressed in the article do not necessarily represent the views of the DOE or the U.S. Government.

## References

- (1) National Renewable Energy Laboratory Efficiency Chart 2020  
<https://www.nrel.gov/pv/assets/pdfs/best-research-cell-efficiencies.20200925.pdf>  
(accessed Oct 22, 2020).
- (2) Saliba, M.; Matsui, T.; Seo, J. Y.; Domanski, K.; Correa-Baena, J. P.; Nazeeruddin, M. K.; Zakeeruddin, S. M.; Tress, W.; Abate, A.; Hagfeldt, A.; et al. Cesium-Containing Triple Cation Perovskite Solar Cells: Improved Stability, Reproducibility and High Efficiency. *Energy Environ. Sci.* **2016**, 9 (6), 1989–1997.  
<https://doi.org/10.1039/c5ee03874j>.
- (3) Kim, D.; Jung, H. J.; Park, I. J.; Larson, B. W.; Dunfield, S. P.; Xiao, C.; Kim, J.; Tong, J.; Boonmongkolras, P.; Ji, S. G.; et al. Efficient, Stable Silicon Tandem Cells Enabled by

- Anion-Engineered Wide-Bandgap Perovskites. *Science* (80-. ). **2020**, 3433 (March), eaba3433. <https://doi.org/10.1126/science.aba3433>.
- (4) McMeekin, D. P.; Sadoughi, G.; Rehman, W.; Eperon, G. E.; Saliba, M.; Horantner, M. T.; Haghighirad, A.; Sakai, N.; Korte, L.; Rech, B.; et al. A Mixed-Cation Lead Mixed-Halide Perovskite Absorber for Tandem Solar Cells. *Science* (80-. ). **2016**, 351 (6269), 151–155. <https://doi.org/10.1126/science.aad5845>.
  - (5) Saliba, M.; Matsui, T.; Domanski, K.; Seo, J. Y.; Ummadisingu, A.; Zakeeruddin, S. M.; Correa-Baena, J. P.; Tress, W. R.; Abate, A.; Hagfeldt, A.; et al. Incorporation of Rubidium Cations into Perovskite Solar Cells Improves Photovoltaic Performance. *Science* (80-. ). **2016**, 354 (6309), 206–209. <https://doi.org/10.1126/science.aah5557>.
  - (6) Rajagopal, A.; Stoddard, R. J.; Jo, S. B.; Hillhouse, H. W.; Jen, A. K.-Y. Overcoming the Photovoltage Plateau in Large Bandgap Perovskite Photovoltaics. *Nano Lett.* **2018**, 18 (6), 3985–3993. <https://doi.org/10.1021/acs.nanolett.8b01480>.
  - (7) Stoddard, R. J.; Rajagopal, A.; Palmer, R. L.; Braly, I. L.; Jen, A. K.-Y.; Hillhouse, H. W. Enhancing Defect Tolerance and Phase Stability of High-Bandgap Perovskites via Guanidinium Alloying. *ACS Energy Lett.* **2018**, 3 (6), 1261–1268. <https://doi.org/10.1021/acsenergylett.8b00576>.
  - (8) Xu, J.; Boyd, C. C.; Yu, Z. J.; Palmstrom, A. F.; Witter, D. J.; Larson, B. W.; France, R. M.; Werner, J.; Harvey, S. P.; Wolf, E. J.; et al. Triple-Halide Wide-Band Gap Perovskites with Suppressed Phase Segregation for Efficient Tandems. *Science* (80-. ). **2020**, 367 (6482), 1097–1104. <https://doi.org/10.1126/science.aaz5074>.
  - (9) Prasanna, R.; Leijtens, T.; Dunfield, S. P.; Raiford, J. A.; Wolf, E. J.; Swifter, S. A.; Werner, J.; Eperon, G. E.; de Paula, C.; Palmstrom, A. F.; et al. Design of Low Bandgap Tin–Lead Halide Perovskite Solar Cells to Achieve Thermal, Atmospheric and Operational Stability. *Nat. Energy* **2019**, 1–9. <https://doi.org/10.1038/s41560-019-0471-6>.
  - (10) Palmstrom, A. F.; Eperon, G. E.; Leijtens, T.; Prasanna, R.; Habisreutinger, S. N.; Nemeth, W.; Gauldin, E. A.; Dunfield, S. P.; Reese, M.; Nanayakkara, S.; et al. Enabling Flexible All-Perovskite Tandem Solar Cells. *Joule* **2019**, 3 (9), 2193–2204. <https://doi.org/10.1016/j.joule.2019.05.009>.
  - (11) Rajagopal, A.; Yang, Z.; Jo, S. B.; Braly, I. L.; Liang, P. W.; Hillhouse, H. W.; Jen, A. K. Y. Highly Efficient Perovskite–Perovskite Tandem Solar Cells Reaching 80% of the Theoretical Limit in Photovoltage. *Adv. Mater.* **2017**, 29 (34), 1–10. <https://doi.org/10.1002/adma.201702140>.
  - (12) Hou, Y.; Aydin, E.; De Bastiani, M.; Xiao, C.; Isikgor, F. H.; Xue, D. J.; Chen, B.; Chen, H.; Bahrami, B.; Chowdhury, A. H.; et al. Efficient Tandem Solar Cells with Solution-Processed Perovskite on Textured Crystalline Silicon. *Science* (80-. ). **2020**, 367 (6482), 1135–1140. <https://doi.org/10.1126/science.aay0262>.
  - (13) Zhuang, J.; Mao, P.; Luan, Y.; Yi, X.; Tu, Z.; Zhang, Y.; Yi, Y.; Wei, Y.; Chen, N.; Lin, T.; et al. Interfacial Passivation for Perovskite Solar Cells: The Effects of the Functional Group in Phenethylammonium Iodide. *ACS Energy Lett.* **2019**, 4 (12), 2913–2921. <https://doi.org/10.1021/acsenergylett.9b02375>.
  - (14) Al-Ashouri, A.; Magomedov, A.; Roß, M.; Jošt, M.; Talaikis, M.; Chistiakova, G.; Bertram, T.; Márquez, J. A.; Köhnen, E.; Kasparavičius, E.; et al. Conformal Monolayer Contacts with Lossless Interfaces for Perovskite Single Junction and Monolithic Tandem Solar Cells. *Energy Environ. Sci.* **2019**, 12 (11), 3356–3369. <https://doi.org/10.1039/c9ee02268f>.

- (15) Yoo, J. J.; Wieghold, S.; Sponseller, M. C.; Chua, M. R.; Bertram, S. N.; Hartono, N. T. P.; Tresback, J. S.; Hansen, E. C.; Correa-Baena, J. P.; Bulović, V.; et al. An Interface Stabilized Perovskite Solar Cell with High Stabilized Efficiency and Low Voltage Loss. *Energy Environ. Sci.* **2019**, *12* (7), 2192–2199. <https://doi.org/10.1039/c9ee00751b>.
- (16) Yoo, J. J.; Seo, G.; Chua, M. R.; Park, T. G.; Lu, Y.; Rotermund, F.; Kim, Y.-K.; Moon, C. S.; Jeon, N. J.; Correa-Baena, J.-P.; et al. Efficient Perovskite Solar Cells via Improved Carrier Management. *Nature* **2021**, *590* (7847), 587–593. <https://doi.org/10.1038/s41586-021-03285-w>.
- (17) Conings, B.; Drijkoningen, J.; Gauquelin, N.; Babayigit, A.; D’Haen, J.; D’Olieslaeger, L.; Ethirajan, A.; Verbeeck, J.; Manca, J.; Mosconi, E.; et al. Intrinsic Thermal Instability of Methylammonium Lead Trihalide Perovskite. *Adv. Energy Mater.* **2015**, *5* (15), 1500477. <https://doi.org/10.1002/aenm.201500477>.
- (18) Tan, W.; Bowring, A. R.; Meng, A. C.; McGehee, M. D.; McIntyre, P. C. Thermal Stability of Mixed Cation Metal Halide Perovskites in Air. *ACS Appl. Mater. Interfaces* **2018**, *10* (6), 5485–5491. <https://doi.org/10.1021/acsami.7b15263>.
- (19) Shi, L.; Bucknall, M. P.; Young, T. L.; Zhang, M.; Hu, L.; Bing, J.; Lee, D. S.; Kim, J.; Wu, T.; Takamura, N.; et al. Gas Chromatography–Mass Spectrometry Analyses of Encapsulated Stable Perovskite Solar Cells. *Science (80- )*. **2020**, eaba2412. <https://doi.org/10.1126/science.aba2412>.
- (20) Cheacharoen, R.; Boyd, C. C.; Burkhard, G. F.; Leijtens, T.; Raiford, J. A.; Bush, K. A.; Bent, S. F.; McGehee, M. D. Encapsulating Perovskite Solar Cells to Withstand Damp Heat and Thermal Cycling. *Sustain. Energy Fuels* **2018**, *2* (11), 2398–2406. <https://doi.org/10.1039/c8se00250a>.
- (21) Dunfield, S. P.; Moore, D. T.; Klein, T. R.; Fabian, D. M.; Christians, J. A.; Dixon, A. G.; Dou, B.; Ardo, S.; Beard, M. C.; Shaheen, S. E.; et al. Curtailing Perovskite Processing Limitations via Lamination at the Perovskite/Perovskite Interface. *ACS Energy Lett.* **2018**, *3* (5), 1192–1197. <https://doi.org/10.1021/acsenergylett.8b00548>.
- (22) Kim, J.; Saidaminov, M. I.; Tan, H.; Zhao, Y.; Kim, Y.; Choi, J.; Jo, J. W.; Fan, J.; Quintero-Bermudez, R.; Yang, Z.; et al. Amide-Catalyzed Phase-Selective Crystallization Reduces Defect Density in Wide-Bandgap Perovskites. *Adv. Mater.* **2018**, *30* (13), 1706275. <https://doi.org/10.1002/adma.201706275>.
- (23) Wang, J.; Fu, W.; Jariwala, S.; Sinha, I.; Jen, A. K.-Y.; Ginger, D. S. Reducing Surface Recombination Velocities at the Electrical Contacts Will Improve Perovskite Photovoltaics. *ACS Energy Lett.* **2018**, *4*, 222–227. <https://doi.org/10.1021/acsenergylett.8b02058>.
- (24) Jariwala, S.; Sun, H.; Adhyaksa, G. W. P.; Lof, A.; Muscarella, L. A.; Ehrler, B.; Garnett, E. C.; Ginger, D. S. Local Crystal Misorientation Influences Non-Radiative Recombination in Halide Perovskites. *Joule* **2019**, *3* (12), 3048–3060. <https://doi.org/10.1016/j.joule.2019.09.001>.
- (25) Stolterfoht, M.; Caprioglio, P.; Wolff, C. M.; Márquez, J. A.; Nordmann, J.; Zhang, S.; Rothhardt, D.; Hörmann, U.; Redinger, A.; Kegelmann, L.; et al. The Perovskite/Transport Layer Interfaces Dominate Non-Radiative Recombination in Efficient Perovskite Solar Cells. Preprint at [Http://Arxiv.Org/Abs/1810.01333](http://Arxiv.Org/Abs/1810.01333). **2018**.
- (26) Braly, I. L.; Dequillettes, D. W.; Pazos-Outón, L. M.; Burke, S.; Ziffer, M. E.; Ginger, D. S.; Hillhouse, H. W. Hybrid Perovskite Films Approaching the Radiative Limit with over 90% Photoluminescence Quantum Efficiency. *Nat. Photonics* **2018**, *12* (6), 355–361.

- <https://doi.org/10.1038/s41566-018-0154-z>.
- (27) Abdi-Jalebi, M.; Andaji-Garmaroudi, Z.; Cacovich, S.; Stavrakas, C.; Philippe, B.; Richter, J. M.; Alsari, M.; Booker, E. P.; Hutter, E. M.; Pearson, Andrew J.; et al. Maximizing and Stabilizing Luminescence from Halide Perovskites with Potassium Passivation. *Nature* **2018**, *555* (7697), 497–501. <https://doi.org/10.1038/nature25989>.
  - (28) DeQuilettes, D. W.; Jariwala, S.; Burke, S.; Ziffer, M. E.; Wang, J. T. W.; Snaith, H. J.; Ginger, D. S. Tracking Photoexcited Carriers in Hybrid Perovskite Semiconductors: Trap-Dominated Spatial Heterogeneity and Diffusion. *ACS Nano* **2017**, *11* (11), 11488–11496. <https://doi.org/10.1021/acsnano.7b06242>.
  - (29) Diekmann, J.; Caprioglio, P.; Rothhardt, D.; Arvind, M.; Unold, T.; Kirchartz, T.; Neher, D.; Stolterfoht, M. Pathways towards 30% Efficient Perovskite Solar Cells. Preprint at <https://arxiv.org/abs/1910.07422>. **2019**.
  - (30) Schulz, P.; Cahen, D.; Kahn, A. Halide Perovskites: Is It All about the Interfaces? *Chemical Reviews*. American Chemical Society March 13, 2019, pp 3349–3417. <https://doi.org/10.1021/acs.chemrev.8b00558>.
  - (31) deQuilettes, D. W.; Koch, S.; Burke, S.; Paranjli, R.; Shropshire, A. J.; Ziffer, M. E.; Ginger, D. S. Photoluminescence Lifetimes Exceeding 8 Ms and Quantum Yields Exceeding 30% in Hybrid Perovskite Thin Films by Ligand Passivation. *ACS Energy Lett.* **2016**, *1* (2), 438–444. <https://doi.org/10.1021/acseenergylett.6b00236>.
  - (32) Noel, N. K.; Abate, A.; Stranks, S. D.; Parrott, E. S.; Burlakov, V. M.; Goriely, A.; Snaith, H. J. Enhanced Photoluminescence and Solar Cell Performance via Lewis Base Passivation of Organic–Inorganic Lead Halide Perovskites. *ACS Nano* **2014**, *8* (10), 9815–9821. <https://doi.org/10.1021/nn5036476>.
  - (33) Brenes, R.; Guo, D.; Osherov, A.; Noel, N. K.; Eames, C.; Hutter, E. M.; Pathak, S. K.; Niroui, F.; Friend, R. H.; Islam, M. S.; et al. Metal Halide Perovskite Polycrystalline Films Exhibiting Properties of Single Crystals. *Joule* **2017**, *1* (1), 155–167. <https://doi.org/10.1016/j.joule.2017.08.006>.
  - (34) Rolston, N.; Bush, K. A.; Printz, A. D.; Gold-Parker, A.; Ding, Y.; Toney, M. F.; McGehee, M. D.; Dauskardt, R. H. Engineering Stress in Perovskite Solar Cells to Improve Stability. *Adv. Energy Mater.* **2018**, *8* (29), 1802139. <https://doi.org/10.1002/aenm.201802139>.
  - (35) Xue, D.-J.; Hou, Y.; Liu, S.-C.; Wei, M.; Chen, B.; Huang, Z.; Li, Z.; Sun, B.; Proppe, A. H.; Dong, Y.; et al. Regulating Strain in Perovskite Thin Films through Charge-Transport Layers. *Nat. Commun.* **2020**, *11* (1), 1514. <https://doi.org/10.1038/s41467-020-15338-1>.
  - (36) Tan, F.; Tan, H.; Saidaminov, M. I.; Wei, M.; Liu, M.; Mei, A.; Li, P.; Zhang, B.; Tan, C.; Gong, X.; et al. In Situ Back-Contact Passivation Improves Photovoltage and Fill Factor in Perovskite Solar Cells. *Adv. Mater.* **2019**, *31* (14), 1807435. <https://doi.org/10.1002/adma.201807435>.
  - (37) Alberti, A.; Deretzis, I.; Mannino, G.; Smecca, E.; Giannazzo, F.; Listorti, A.; Colella, S.; Masi, S.; La Magna, A. Nitrogen Soaking Promotes Lattice Recovery in Polycrystalline Hybrid Perovskites. *Adv. Energy Mater.* **2019**, *9* (12), 1803450. <https://doi.org/10.1002/aenm.201803450>.
  - (38) Miyasaka, T.; Kulkarni, A.; Kim, G. M.; Öz, S.; Jena, A. K. Perovskite Solar Cells: Can We Go Organic-Free, Lead-Free, and Dopant-Free? *Adv. Energy Mater.* **2020**, *10* (13), 1902500. <https://doi.org/10.1002/aenm.201902500>.
  - (39) Liu, N.; Yam, C. Y. First-Principles Study of Intrinsic Defects in Formamidinium Lead

- Triiodide Perovskite Solar Cell Absorbers. *Phys. Chem. Chem. Phys.* **2018**, *20* (10), 6800–6804. <https://doi.org/10.1039/c8cp00280k>.
- (40) Azpiroz, J. M.; Mosconi, E.; Bisquert, J.; De Angelis, F. Defect Migration in Methylammonium Lead Iodide and Its Role in Perovskite Solar Cell Operation. *Energy Environ. Sci.* **2015**, *8* (7), 2118–2127. <https://doi.org/10.1039/C5EE01265A>.
- (41) Gratia, P.; Grancini, G.; Audinot, J.-N.; Jeanbourquin, X.; Mosconi, E.; Zimmermann, I.; Dowsett, D.; Lee, Y.; Gra, M.; De Angelis, F.; et al. Intrinsic Halide Segregation at Nanometer Scale Determines the High Efficiency of Mixed Cation/Mixed Halide Perovskite Solar Cells. <https://doi.org/10.1021/jacs.6b10049>.
- (42) Ambrosio, F.; Meggiolaro, D.; Mosconi, E.; De Angelis, F. Charge Localization and Trapping at Surfaces in Lead-Iodide Perovskites: The Role of Polarons and Defects. *J. Mater. Chem. A* **2020**, *8* (14), 6882–6892. <https://doi.org/10.1039/d0ta00798f>.
- (43) Meggiolaro, D.; Mosconi, E.; De Angelis, F. Formation of Surface Defects Dominates Ion Migration in Lead-Halide Perovskites. *ACS Energy Lett.* **2019**, *4* (3), 779–785. <https://doi.org/10.1021/acseenergylett.9b00247>.
- (44) Yin, W.-J.; Shi, T.; Yan, Y. Unusual Defect Physics in CH<sub>3</sub>NH<sub>3</sub>PbI<sub>3</sub> Perovskite Solar Cell Absorber. *Appl. Phys. Lett.* **2014**, *104* (6), 063903/1–063903/4. <https://doi.org/10.1063/1.4864778>.
- (45) Meggiolaro, D.; Motti, S. G.; Mosconi, E.; Barker, A. J.; Ball, J.; Andrea Riccardo Perini, C.; Deschler, F.; Petrozza, A.; De Angelis, F. Iodine Chemistry Determines the Defect Tolerance of Lead-Halide Perovskites. *Energy Environ. Sci.* **2018**, *11* (3), 702–713. <https://doi.org/10.1039/c8ee00124c>.
- (46) Quarti, C.; De Angelis, F.; Beljonne, D. Influence of Surface Termination on the Energy Level Alignment at the CH<sub>3</sub>NH<sub>3</sub>PbI<sub>3</sub> Perovskite/C60 Interface. *Chem. Mater.* **2017**, *29* (3), 958–968. <https://doi.org/10.1021/acs.chemmater.6b03259>.
- (47) Thompson, W. R.; Cai, M.; Ho, M.; Pemberton, J. E. Hydrolysis and Condensation of Self-Assembled Monolayers of (3-Mercaptopropyl)Trimethoxysilane on Ag and Au Surfaces. *Langmuir* **1997**, *13* (28), 2291–2302. <https://doi.org/10.1021/la960795g>.
- (48) Brinker, C. J.; Scherer, G. W. *Sol-Gel Science The Physics and Chemistry of Sol-Gel Processing*. Academic Press, San Diego. - References - Scientific Research Publishing; Academic Press: San Diego, CA, 1990.
- (49) Brinker, C. J. Hydrolysis and Condensation of Silicates: Effects On Structure. *J. Non-Cryst. Solids* **1988**, *100*, 31–50.
- (50) deQuilettes, D. W.; Koch, S.; Burke, S.; Paranjli, R.; Shropshire, A. J.; Ziffer, M. E.; Ginger, D. S. Photoluminescence Lifetimes Exceeding 8 Ms and Quantum Yields Exceeding 30% in Hybrid Perovskite Thin Films by Ligand Passivation. *ACS Energy Lett.* **2016**, *1* (2), 438–444. <https://doi.org/10.1021/acseenergylett.6b00236>.
- (51) Ross, R. T. Some Thermodynamics of Photochemical Systems. *J. Chem. Phys.* **1967**, *46* (12), 4590–4593. <https://doi.org/10.1063/1.1840606>.
- (52) Grätzel, M. The Light and Shade of Perovskite Solar Cells. *Nat. Mater.* **2014**, *13* (9), 838–842. <https://doi.org/10.1038/nmat4065>.
- (53) Richter, J. M.; Abdi-Jalebi, M.; Sadhanala, A.; Tabachnyk, M.; Rivett, J. P. H.; Pazos-Outón, L. M.; Gödel, K. C.; Price, M.; Deschler, F.; Friend, R. H. Enhancing Photoluminescence Yields in Lead Halide Perovskites by Photon Recycling and Light Out-Coupling. *Nat. Commun.* **2016**, *7*. <https://doi.org/10.1038/ncomms13941>.
- (54) Bi, D.; Tress, W.; Dar, M. I.; Gao, P.; Luo, J.; Renevier, C.; Schenk, K.; Abate, A.;

- Giordano, F.; Correa Baena, J. P.; et al. Efficient Luminescent Solar Cells Based on Tailored Mixed-Cation Perovskites. *Sci. Adv.* **2016**, *2* (1), e1501170. <https://doi.org/10.1126/sciadv.1501170>.
- (55) Eperon, G. E.; Hörantner, M. T.; Snaith, H. J. Metal Halide Perovskite Tandem and Multiple-Junction Photovoltaics. *Nat. Rev. Chem.* **2017**, *1*, 0095. <https://doi.org/10.1038/s41570-017-0095>.
- (56) Bush, K. A.; Frohna, K.; Prasanna, R.; Beal, R. E.; Leijtens, T.; Swifter, S. A.; McGehee, M. D. Compositional Engineering for Efficient Wide Band Gap Perovskites with Improved Stability to Photoinduced Phase Segregation. *ACS Energy Lett.* **2018**, *3* (2), 428–435. <https://doi.org/10.1021/acsenergylett.7b01255>.
- (57) Mahesh, S.; Ball, J. M.; Oliver, R. D. J.; Mcmeekin, D. P.; Nayak, P. K.; Johnston, M. B.; Snaith, H. J. Revealing the Origin of Voltage Loss in Mixed-Halide Perovskite Solar Cells †. *This J. is Cite this Energy Environ. Sci* **2020**, *13*, 258. <https://doi.org/10.1039/c9ee02162k>.
- (58) Shallcross, R. C.; Zheng, Y.; Saavedra, S. S.; Armstrong, N. R. Determining Band-Edge Energies and Morphology-Dependent Stability of Formamidinium Lead Perovskite Films Using Spectroelectrochemistry and Photoelectron Spectroscopy. *J. Am. Chem. Soc.* **2017**, *139* (13), 4866–4878. <https://doi.org/10.1021/jacs.7b00516>.
- (59) Chen, P.; Bai, Y.; Wang, S.; Lyu, M.; Yun, J.-H.; Wang, L. In Situ Growth of 2D Perovskite Capping Layer for Stable and Efficient Perovskite Solar Cells. *Adv. Funct. Mater.* **2018**, *28* (17), 1706923. <https://doi.org/10.1002/adfm.201706923>.
- (60) Shallcross, R. C.; Olthof, S.; Meerholz, K.; Armstrong, N. R. Impact of Titanium Dioxide Surface Defects on the Interfacial Composition and Energetics of Evaporated Perovskite Active Layers. *ACS Appl. Mater. Interfaces* **2019**, *11* (35), 32500–32508. <https://doi.org/10.1021/acsami.9b09935>.
- (61) Acres, R. G.; Ellis, A. V.; Alvino, J.; Lenahan, C. E.; Khodakov, D. A.; Metha, G. F.; Andersson, G. G. Molecular Structure of 3-Aminopropyltriethoxysilane Layers Formed on Silanol-Terminated Silicon Surfaces. *J. Phys. Chem. C* **2012**, *116* (10), 6289–6297. <https://doi.org/10.1021/jp212056s>.
- (62) DeQuilettes, D. W.; Vorpahl, S. M.; Stranks, S. D.; Nagaoka, H.; Eperon, G. E.; Ziffer, M. E.; Snaith, H. J.; Ginger, D. S. Impact of Microstructure on Local Carrier Lifetime in Perovskite Solar Cells. *Science* (80-. ). **2015**, *348* (6235), 683–686. <https://doi.org/10.1126/science.aaa5333>.
- (63) Pointon, A. I.; Grant, N. E.; Pain, S. L.; White, J. T.; Murphy, J. D. Sub-2 Cm/s Passivation of Silicon Surfaces by Aprotic Solutions. *Appl. Phys. Lett.* **2020**, *116* (12), 121601. <https://doi.org/10.1063/5.0003704>.
- (64) Grant, N. E.; Niewelt, T.; Wilson, N. R.; Wheeler-Jones, E. C.; Bullock, J.; Al-Amin, M.; Schubert, M. C.; Van Veen, A. C.; Javey, A.; Murphy, J. D. Superacid-Treated Silicon Surfaces: Extending the Limit of Carrier Lifetime for Photovoltaic Applications. *IEEE J. Photovoltaics* **2017**, *7* (6), 1574–1583. <https://doi.org/10.1109/JPHOTOV.2017.2751511>.
- (65) Woodall, J. M.; Hovel, H. J. High-Efficiency Ga1-XAlxAsSingle Bond SignGaAs Solar Cells. *Appl. Phys. Lett.* **1972**, *21* (8), 379–381. <https://doi.org/10.1063/1.1654421>.
- (66) Vermang, B.; Fjällström, V.; Pettersson, J.; Salomé, P.; Edoff, M. Development of Rear Surface Passivated Cu(In,Ga)Se2 Thin Film Solar Cells with Nano-Sized Local Rear Point Contacts. *Sol. Energy Mater. Sol. Cells* **2013**, *117*, 505–511. <https://doi.org/10.1016/j.solmat.2013.07.025>.

- (67) Reese, M. O.; Perkins, C. L.; Burst, J. M.; Farrell, S.; Barnes, T. M.; Johnston, S. W.; Kuciauskas, D.; Gessert, T. A.; Metzger, W. K. Intrinsic Surface Passivation of CdTe. *J. Appl. Phys.* **2015**, *118* (15), 155305. <https://doi.org/10.1063/1.4933186>.
- (68) Liu, Z.; Kru, L.; Krogmeier, B.; Klingebiel, B.; Ma, A.; Levchenko, S.; Mathur, S.; Rau, U.; Unold, T.; Kirchartz, T. Open-Circuit Voltages Exceeding 1.26 V in Planar Methylammonium Lead Iodide Perovskite Solar Cells. **2019**, *4*, 110–117. <https://doi.org/10.1021/acsenergylett.8b01906>.
- (69) Staub, F.; Hempel, H.; Hebig, J.-C.; Mock, J.; Paetzold, U. W.; Rau, U.; Unold, T.; Kirchartz, T. Beyond Bulk Lifetimes: Insights into Lead Halide Perovskite Films from Time-Resolved Photoluminescence. **2016**. <https://doi.org/10.1103/PhysRevApplied.6.044017>.
- (70) Yang, Y.; Yan, Y.; Yang, M.; Choi, S.; Zhu, K.; Luther, J. M.; Beard, M. C. Low Surface Recombination Velocity in Solution-Grown CH<sub>3</sub>NH<sub>3</sub>PbBr<sub>3</sub> Perovskite Single Crystal. *Nat Commun* **2015**, *6*, 7961. <https://doi.org/10.1038/ncomms8961>.
- (71) Yang, Y.; Yang, M.; Moore, D. T.; Yan, Y.; Miller, E. M.; Zhu, K.; Beard, M. C.; Kojima, A.; Teshima, K.; Shirai, Y.; et al. Top and Bottom Surfaces Limit Carrier Lifetime in Lead Iodide Perovskite Films. *Nat. Energy* **2017**, *2* (January), 16207. <https://doi.org/10.1038/nenergy.2016.207>.
- (72) Sproul, A. B. Dimensionless Solution of the Equation Describing the Effect of Surface Recombination on Carrier Decay in Semiconductors Contactless Determination of Current–Voltage Characteristics and Minority-Carrier Lifetimes in Semiconductors from Quasi-Steady-State. *J. Appl. Phys.* **1994**, *76* (10), 2851–2282. <https://doi.org/10.1063/1.361459>.
- (73) Burgelman, M.; Nollet, P.; Degraeve, S. Modelling Polycrystalline Semiconductor Solar Cells. *Thin Solid Films* **2000**, *361*, 527–532. [https://doi.org/10.1016/S0040-6090\(99\)00825-1](https://doi.org/10.1016/S0040-6090(99)00825-1).
- (74) Burgelman, M.; Decock, K.; Khelifi, S.; Abass, A. Advanced Electrical Simulation of Thin Film Solar Cells. In *Thin Solid Films*; Elsevier, 2013; Vol. 535, pp 296–301. <https://doi.org/10.1016/j.tsf.2012.10.032>.
- (75) Al-Ashouri, A.; Köhnen, E.; Li, B.; Magomedov, A.; Hempel, H.; Caprioglio, P.; Márquez, J. A.; Vilches, A. B. M.; Kasparavicius, E.; Smith, J. A.; et al. Monolithic Perovskite/Silicon Tandem Solar Cell with >29% Efficiency by Enhanced Hole Extraction. *Science (80-. )*. **2020**, *370* (6522), 1300–1309. <https://doi.org/10.1126/science.abd4016>.
- (76) Green, M. A. The Passivated Emitter and Rear Cell (PERC): From Conception to Mass Production. *Sol. Energy Mater. Sol. Cells* **2015**, *143*, 190–197. <https://doi.org/10.1016/j.solmat.2015.06.055>.
- (77) Adhyaksa, G. W. P.; Johlin, E.; Garnett, E. C. Nanoscale Back Contact Perovskite Solar Cell Design for Improved Tandem Efficiency. *Nano Lett.* **2017**, *17* (9), 5206–5212. <https://doi.org/10.1021/acs.nanolett.7b01092>.
- (78) Tainter, G. D.; Hörantner, M. T.; Pazos-Outón, L. M.; Lamboll, R. D.; Āboliņš, H.; Leijtens, T.; Mahesh, S.; Friend, R. H.; Snaith, H. J.; Joyce, H. J.; et al. Long-Range Charge Extraction in Back-Contact Perovskite Architectures via Suppressed Recombination. *Joule* **2019**, *3* (5), 1301–1313. <https://doi.org/10.1016/j.joule.2019.03.010>.



# Appendix A: Supplementary Information for Chapter 2

## Experimental Procedures

### Precursor Preparation and Film Deposition

In a nitrogen-filled glovebox, a methylammonium iodide (MAI) solution (1.78 M) was made by dissolving MAI (Dyesol, CAS:14965-49-2) in anhydrous N,N-dimethylformamide (DMF). Lead acetate trihydrate ( $\text{PbOAc}_2 \cdot 3\text{H}_2\text{O}$ ) (99.999%, Sigma-Aldrich, CAS:6080-56-4) was added to the MAI solution at a 3:1 molar ratio of MAI to  $\text{PbOAc}_2 \cdot 3\text{H}_2\text{O}$  (0.59 M). A hypophosphorous acid (HPA) solution was further added to the precursor solution with a molar ratio HPA/ $\text{PbOAc}_2 \cdot 3\text{H}_2\text{O}$  of 8%.<sup>35</sup>

Glass substrates were cleaned by sequentially sonicating in 2% Micro-90 detergent, DI water, acetone, then propan-2-ol. Prior to film deposition, the glass substrates were plasma-cleaned. The perovskite precursor solution was spin-coated on top in a nitrogen-filled glovebox, at 2000 rpm for 45 s to form the perovskite thin film layer. The films were then annealed at room temperature for 10 mins and at 100°C for 5 mins.

### Fluorescence Lifetime Imaging Microscopy

A custom scanning confocal microscope built around Nikon TE-2000 inverted microscope with a sample stage controlled by Physik Instrumente E-710 piezo controller was used to measure fluorescence images. The system was first calibrated using 200 nm fluorescent microspheres (Lifetechnologies FluoSpheres Polystyrene Microspheres, 200 nm, red fluorescent, 580/605 nm). The sample was illuminated, through a LU Nikon Plan Fluor 100x infinity corrected dry objective (0.9 NA), with 470 nm pulsed diode laser (PDL-800 LDH-P-C-470B, 1 MHz, ~300 ps pulse width) and the emission was filtered using a 50/50 dichroic beam splitter and a pair of 500/600 nm long-pass filters. The local fluorescence was measured by directing the emission to a Micro Photon Devices PDM series single-photon avalanche photodiode with a 50  $\mu\text{m}$  active area. The pixel size (or scanning step size) used for fluorescence lifetime images was 100 nm and the pixel dwell time (or integration time) was 100 ms.

### Electron Back-Scatter Diffraction (EBSD)

PELCO® conductive silver paint was first deposited on top of the perovskite film on glass to cover all the edges of the film. Upon drying, it forms a thick silver layer around edges to provide good conductivity with a sheet resistance of 0.066 ohm/sq. The dried silver paint was then connected to a metal sample holder for further grounding. EBSD was performed in the region between the silver paint (~5 mm x 5mm) to avoid any charging effects. The electron beam was optimized to 100 pA beam current and 6 kV accelerating voltage with a 10 mm working distance to the sample. The sample was tilted such that the electron beam was hitting the sample at 70° with respect to the sample surface normal. The electron beam was scanned across the sample

with a step size of 50-100 nm to collect Kikuchi patterns at every pixel. The patterns were collected using EDAX OIM software and the pixel integration time was 100 ms. The electron dose rate for the measurement was estimated to be  $\sim 0.1$  electrons/ $\text{\AA}^2$  per second. The total dose for  $8\mu\text{m} \times 8\mu\text{m}$  scan with  $0.1\mu\text{m}$  step size and 100 ms pixel dwell time was estimated to be  $\sim 62$  electrons / $\text{\AA}^2$ . The  $1/e$  decay length for the backscatter electron energy distribution in the X-Y plane is  $\sim 106$  nm (Figure S17), thus justifying the assumption in the calculation that the beam size is similar to the step size in the measurement.

The individual Kikuchi patterns acquired from EBSD were indexed to a tetragonal MAPI structure with  $I4/mcm$  space group symmetry.<sup>1,2</sup> The lattice parameters used were  $a = b = 8.84$   $\text{\AA}$  and  $c = 12.63$   $\text{\AA}$ . The overall absolute error in orientation determination was calculated using average fit to be  $1.8^\circ$  (typically, the accuracy of absolute orientation determination is  $\sim 2^\circ$ ).<sup>3</sup> Average fit describes the average angular difference between the detected Kikuchi bands in the diffraction pattern and the corresponding bands reconstructed from the orientation solution.<sup>4</sup> The average fit value is heavily dependent on the pattern quality and the Kikuchi band detection parameters.<sup>5</sup> However, when detecting sub-grain microstructures, the accuracy of relative orientations between adjacent data points is more important.<sup>3</sup> The relative angular resolution was measured by scanning across a Si (100) single crystal. The orientation noise or the angular resolution was found to be  $< 1^\circ$  for 90% of the points. The beam conditions were 6 kV accelerating voltage, 800 pA beam current and 0.2 s exposure. Post indexing, the EBSD data was analyzed and plotted using MTEX, an open-source MATLAB toolbox for texture/orientation analysis.<sup>6,7</sup>

## Supplementary Information

### Kikuchi Diffraction Patterns Analysis

We process the data using a home script to remove background, optimize brightness and contrast, and balance the signal in 4 quadrants of the detector. The boundaries between the 4 quadrants of the detector are also removed to prevent it from being recognized as a diffraction line. Using OIM Analysis Software from EDAX, the patterns are corrected to reduce the noise levels using Neighbor Pattern Averaging & Reindexing (NPAR) method prior to indexing.

The Kikuchi patterns are also calibrated with an Aluminum metal sheet at the same working distance as the perovskite sample. Next, we optimize Hough transform by adjusting convolution mask, maximum band count, Rho fraction. After indexing, we correct pseudosymmetry and correct non-indexed points with grain dilation function. Lastly, we further improve image with Neighbor Orientation Correlation.

### Grain Detection using MTEX

During grain identification from raw inverse pole figure (IPF), pixelated regions are first identified and removed. These are the points that the grain detection algorithm identifies as one pixel grain, and since that is likely a random measurement point/indexing error, they are removed from the map.

Once these pixels are removed from the EBSD map, a grain threshold angle is selected, and grain identification is performed using MTEX texture analysis package. According to the MTEX

algorithm,<sup>8</sup> missing data due to measurement errors (here the removed pixels) do not interfere in the grain detection process.<sup>8</sup> Briefly, in the MTEX algorithm, there is no systemic bias in the assignment of these missing orientations and, they do not cause the grain to be split into different grains. The missing orientation data are equally assigned to neighboring points. Importantly, since the pixels are removed, they do not contribute to or interfere in any further analysis of grains, grain boundaries, grain orientation spread, etc.

Post grain detection, we plot the mean grain orientation along with the grain boundaries. The above process is depicted in Figure S8.

### **Aligning Confocal Photoluminescence (PL) Images and EBSD maps**

First, a region of interest (ROI) was formed by using Atomic Force Microscope (AFM) tip in contact mode to precisely scratch through the perovskite film. The ROI size was defined by AFM controls in x and y direction. After ROI was formed, confocal PL was performed on the ROI and silver paint was then deposited on the sides of the film for EBSD. Then, EBSD was performed on the same ROI to generate a local crystal orientation map.

Using an image registration program written in python using packages such as scikit-image<sup>9</sup> and OpenCV, the confocal PL maps and EBSD maps were aligned keeping ROI fiducial markers as known reference points across the two maps. Image registration between PL and EBSD was achieved by using fiducial markers followed by affine transformation (to account for resolution differences, beam angle etc). Post alignment, the PL and EBSD were overlaid to map the grain orientation spread of the grains to their corresponding local PL. Since the analysis requires correlation with PL, grains that were not optically resolved (smaller than the resolution limit of the microscope) were not considered for the analysis. Furthermore, grains right beside the scratch were also not considered for the analysis due to possible mechanical damage from scratching. The data were binned in intervals of GOS to create a plot of average PL intensity as a function of GOS.

### **Hypothesis testing and p-value**

In inferential statistics, hypothesis testing is used to deduce relationships between the underlying distributions. The most common test is the null hypothesis ( $H_0$ ) versus the alternate hypothesis ( $H_a$ ) test.  $H_0$  assumes that there is no relationship between underlying distributions, say X and Y.  $H_a$  assumes that there is some relationship between the distributions.<sup>10</sup>

The p-value is the probability of the occurrence of a given event within a statistical hypothesis test. In other words, the p-value indicates the probability of uncorrelated distributions (X and Y) producing the same correlation as determined from the correlated distributions, X and Y.

The interpretation of p-value is as follows: a small p-value (generally,  $p < 0.05$  or 5%) indicates that it is *unlikely* that any association between the distributions (X & Y) exists due to *random chance*. Therefore, if we see a small p-value ( $p < 0.05$ ), we can infer that there is a relationship between the distributions, and we can reject the null hypothesis. In other words, a small p-value ( $p < 0.05$ ) indicates that there is statistically significant relationship between X and Y.<sup>10</sup> On the contrary, if the p-value is greater than 0.05, we can infer that the relationship between the distributions is not statistically significant and we cannot reject the null hypothesis.<sup>10</sup> We note that a p-value larger than the threshold (0.05) does not imply there is simply *no relationship*

between the distributions. But, instead, the hypothesis under investigation does not adequately explain the observations.

We also note that although the choice of p-value threshold of 0.05 is most commonly used, it is an arbitrary convention.

The correlations and p-values were calculated using scipy (scipy.stats) library in python.<sup>11</sup>

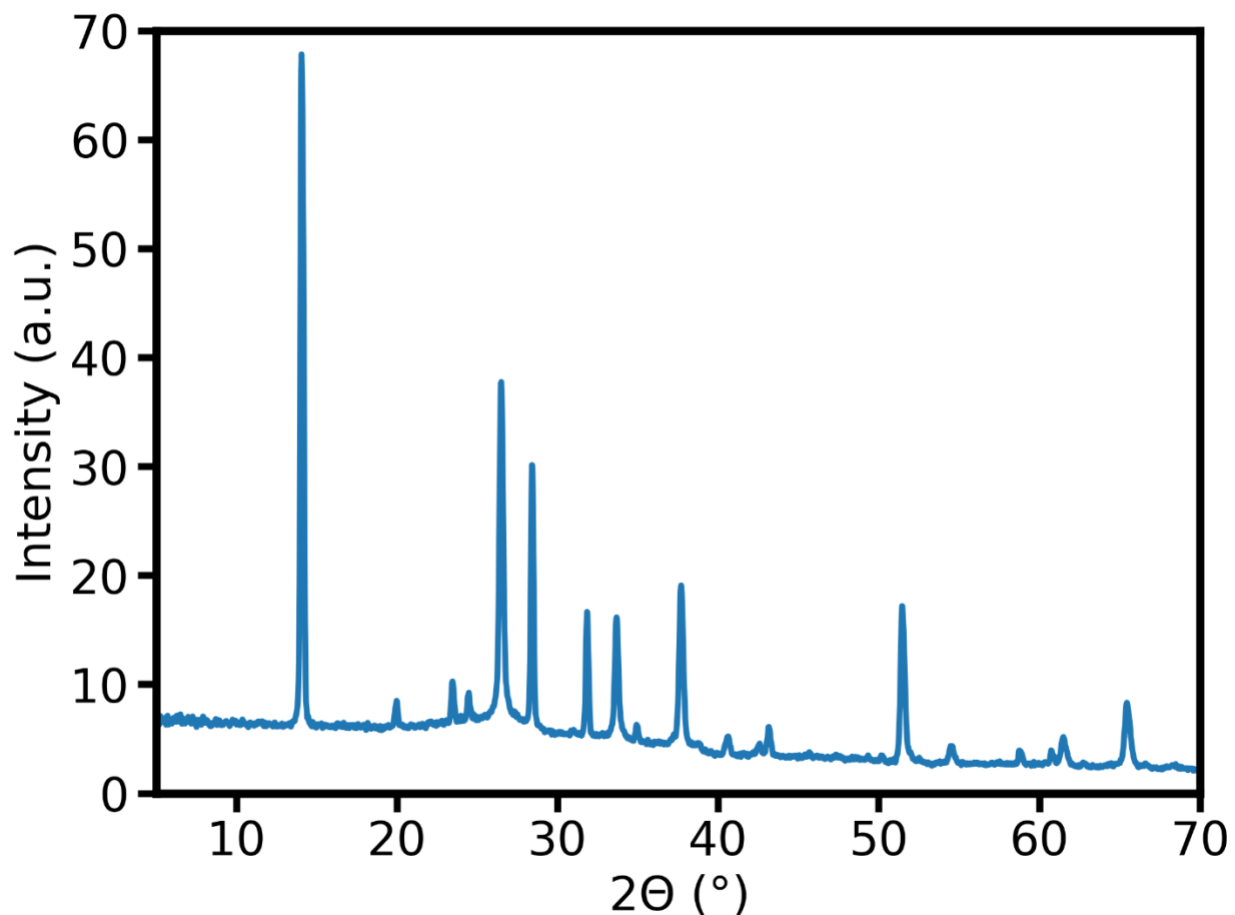


**Figure S1. XRD plot of a representative  $\text{CH}_3\text{NH}_3\text{PbI}_3$  thin film on FTO substrate demonstrating the crystallinity of the film.**

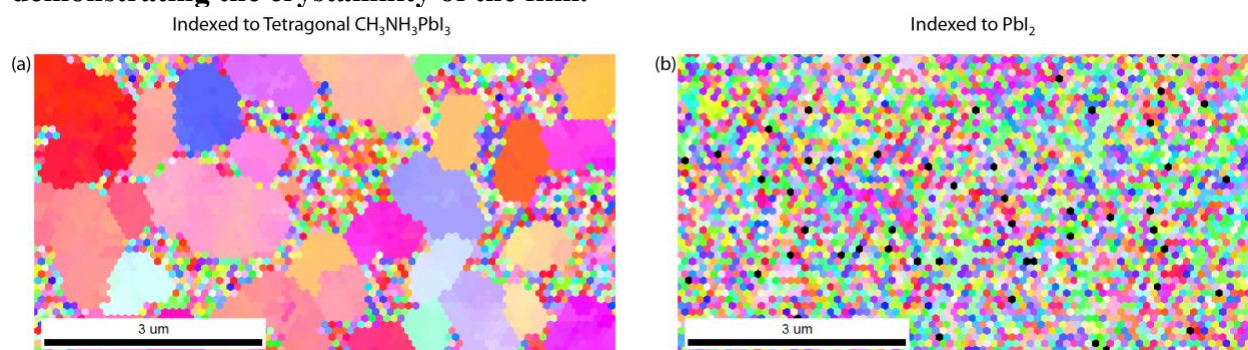


**Figure S2. Inverse Pole Figure of  $\text{CH}_3\text{NH}_3\text{PbI}_3$  thin films with individual back scatter diffraction patterns indexed to (a) tetragonal  $\text{CH}_3\text{NH}_3\text{PbI}_3$  structure and (b) hexagonal  $\text{PbI}_2$  for the same scan region.**

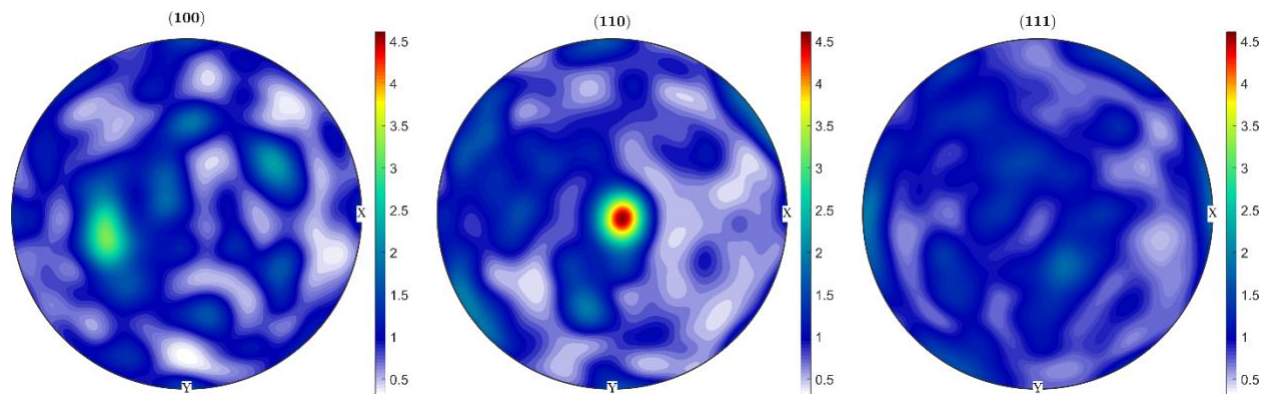


**Figure S3. Pole Density Figure. Projection of crystal orientations into the sample coordinate system. The color bars represent multiples of random distribution of orientations, meaning pole figure of a random standard sample would be ‘1x’ at all points. Pole figure regions with intensities higher than ‘1x’ demonstrate lattice planes that are preferentially aligned in those directions compared to a sample with random texture.**

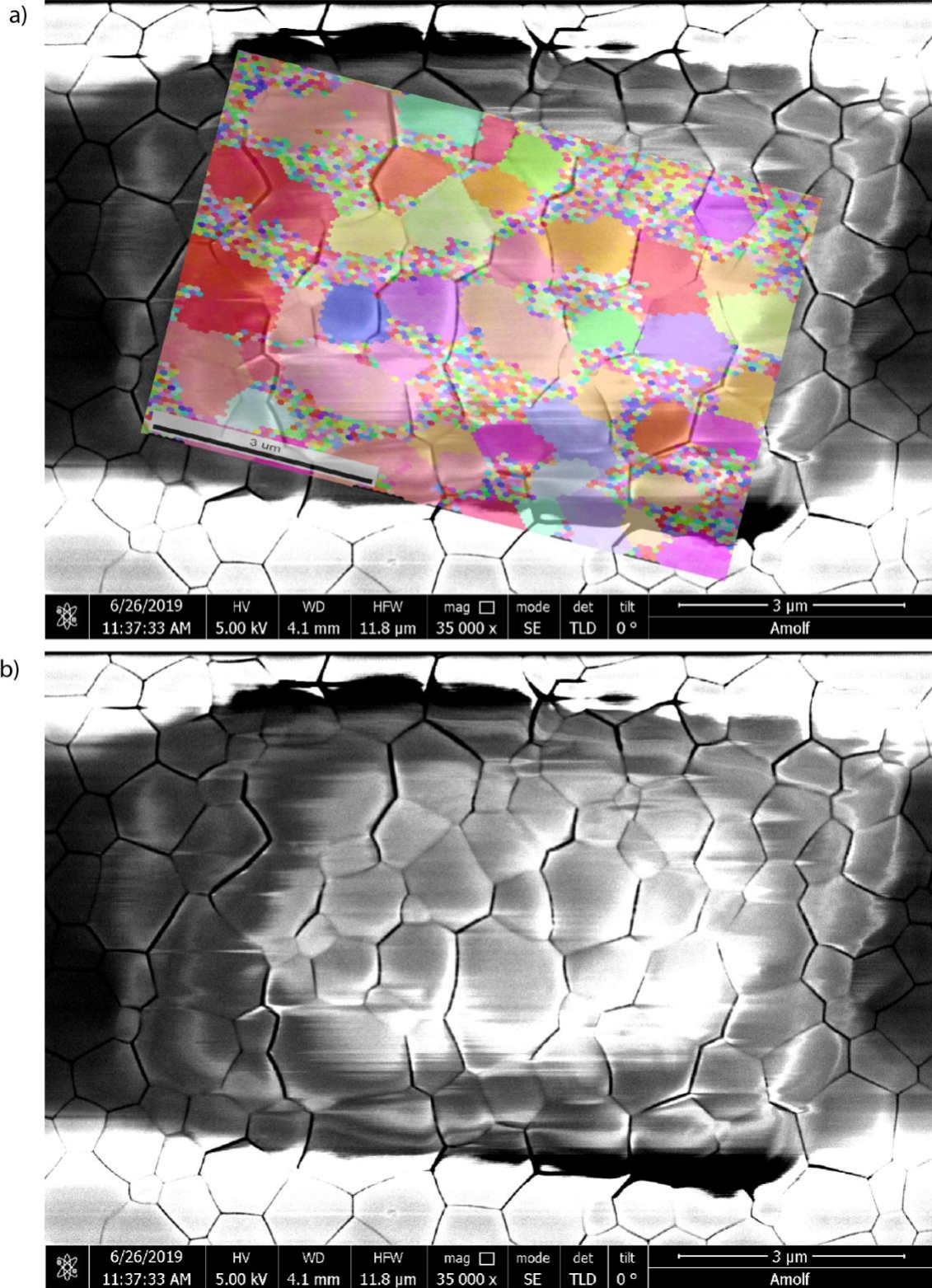


**Figure S4. Conventional SEM image at 0 degrees tilt and EBSD of the corresponding region. (a) Inverse Pole Figure (IPF) overlaid on top of the high-resolution SEM image. (b)**

High-resolution SEM image acquired after EBSD measurement. The white regions are due to charging effects.

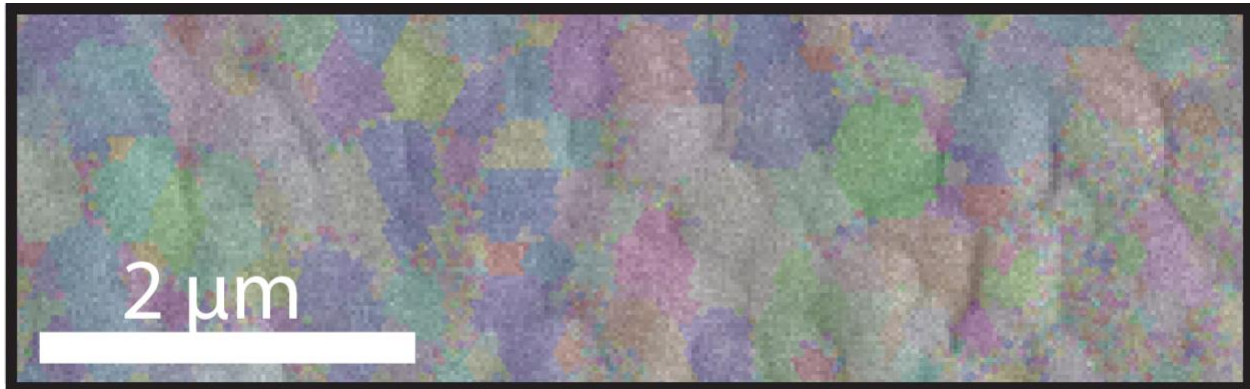


Figure S5. Overlay of scanning electron microscope image and inverse pole figure (IPF) shown in Figure 1b and 1c in the main text.

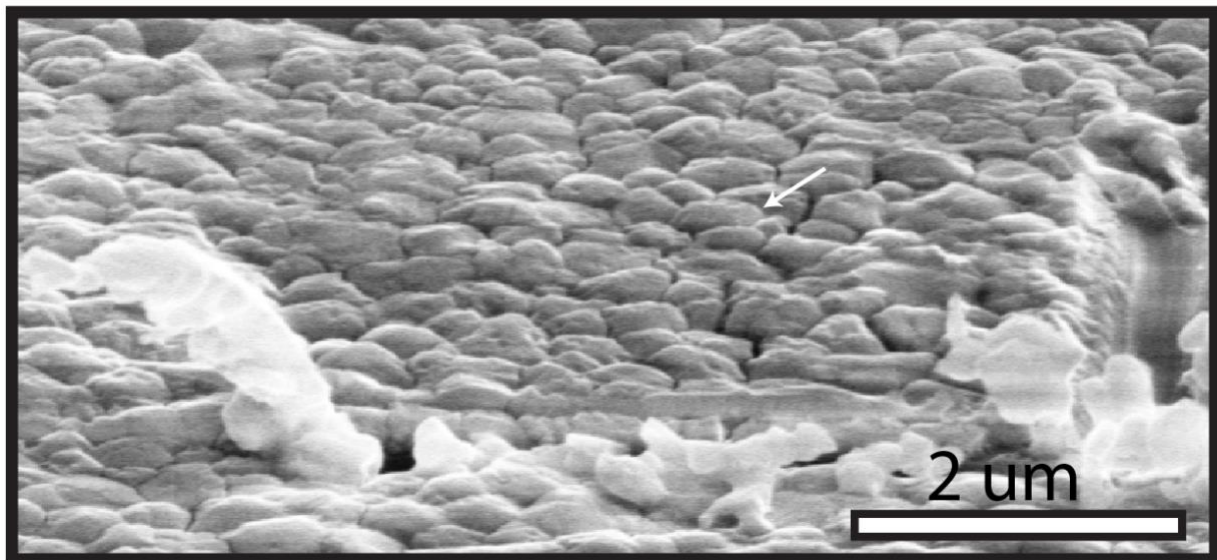
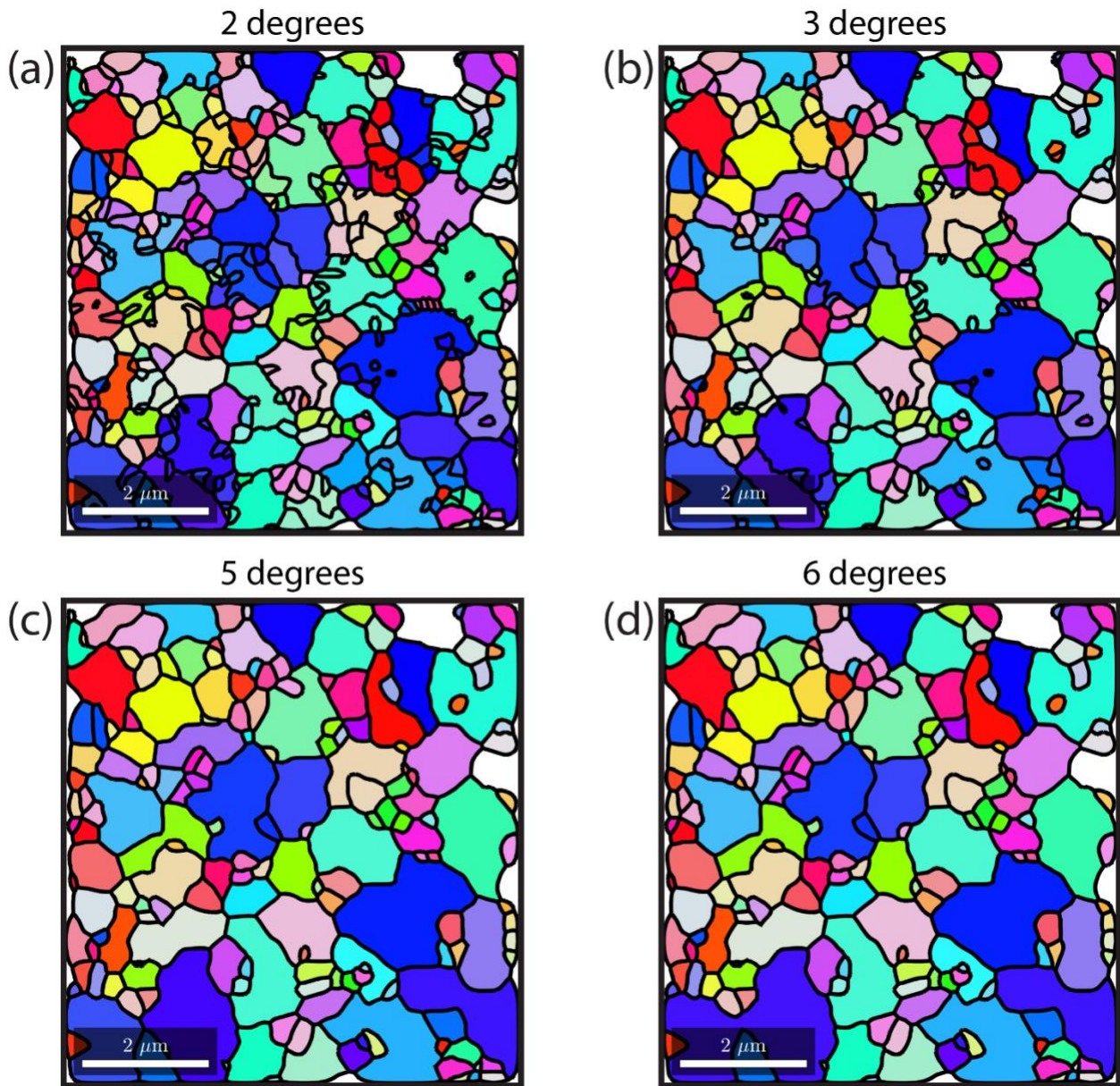
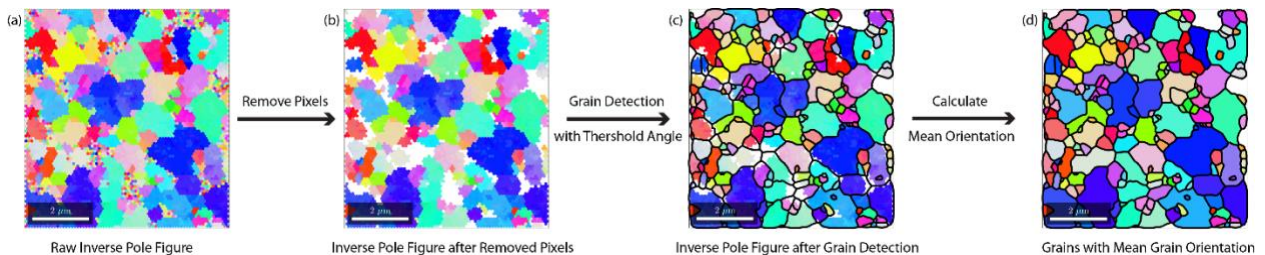


Figure S6. Higher resolution SEM image (at 40° tilt) of the region in Figure 1b in the main text with scratch markers defining the ROI. The arrow shows the same region along the arrow in Figure 1b.



**Figure S7. Grain identification from IPF using different misorientation thresholds of (a) 2 degrees, (b) 3 degrees, (c) 5 degrees and (d) 6 degrees. Grains are plotted with their mean orientation. Refer Figure 2 in the main text for 4 degrees grain threshold and for color key.**



**Figure S8. Grain identification process from raw inverse pole figure (IPF) to grains with mean orientation. (a) Raw IPF. (b) IPF after pixelated regions corresponding to one pixel grain are removed from the map. (c) Grain detection performed on resulting IPF from (b) with a threshold angle. The IPF is plotted with corresponding grains and grain boundaries that were identified. (d) Grain mean orientation is calculated and plotted with the corresponding grain boundaries.**

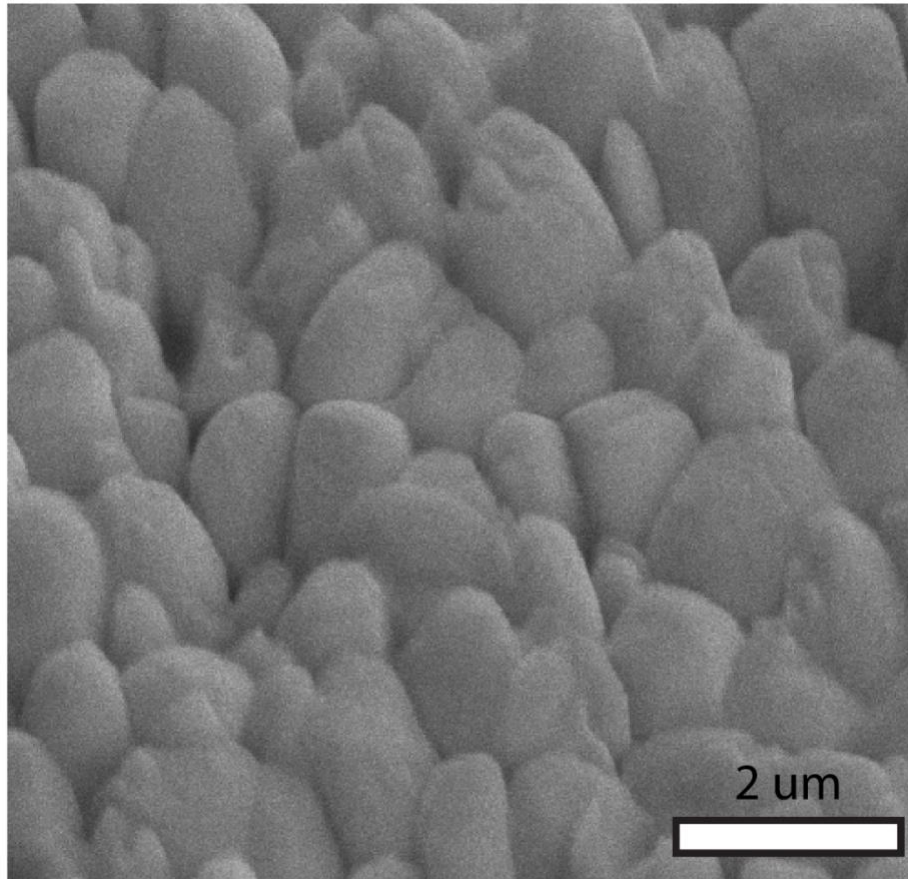


**Figure S9. SEM image at 40° tilt of CH<sub>3</sub>NH<sub>3</sub>PbI<sub>3</sub> thin film for the region in Figure 2 in the main text.**

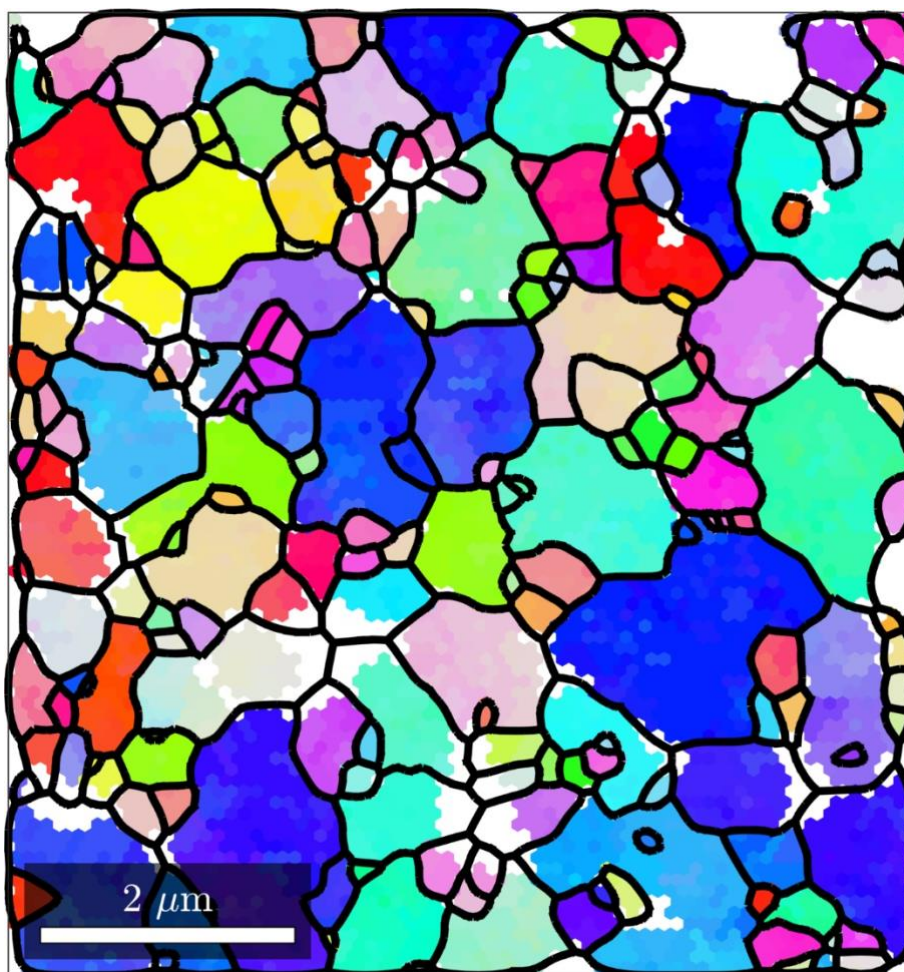


**Figure S10. Inverse Pole Figure (IPF) with grain boundaries after grain detection showing grain-to-grain orientation heterogeneity within the film. See Figure 2a and 2b in main text for IPF and plot of grains with mean orientation.**

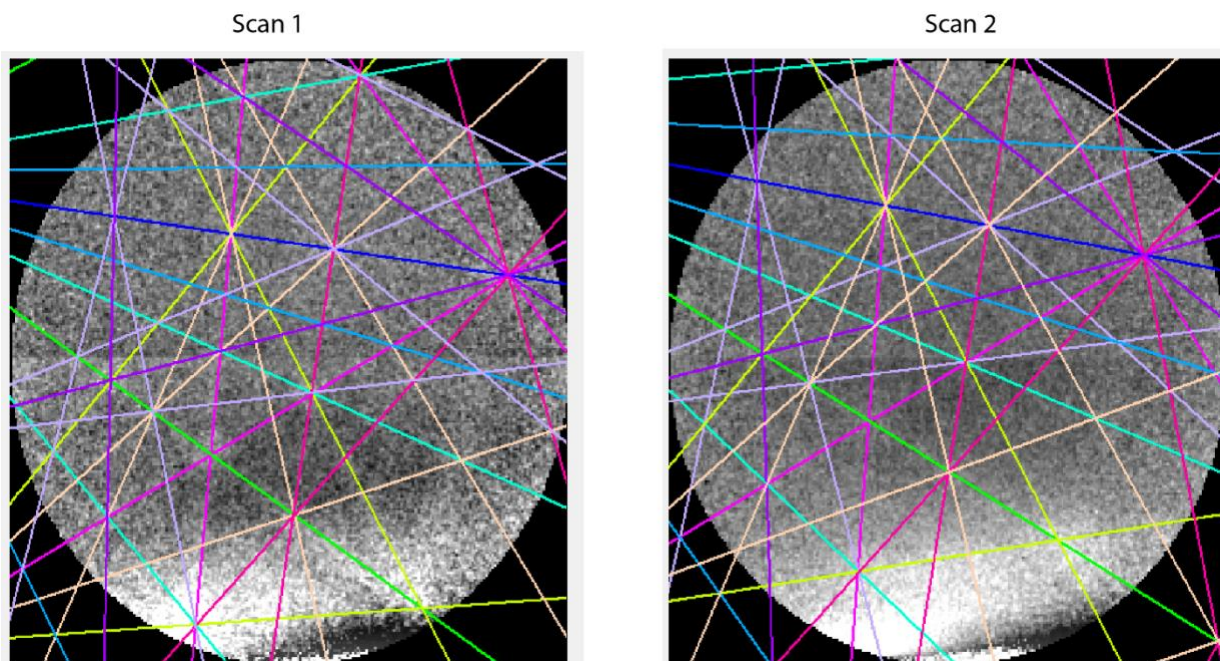


**Figure S11. Electron back scatter diffraction patterns of the same region from two consecutive scans showing that the pattern is present and indexed to the same crystallographic orientation of tetragonal  $\text{CH}_3\text{NH}_3\text{PbI}_3$  after consecutive scans and, thus, demonstrating the minimal influence of electron beam induced damage on the overall results interpreted from the diffraction patterns.**

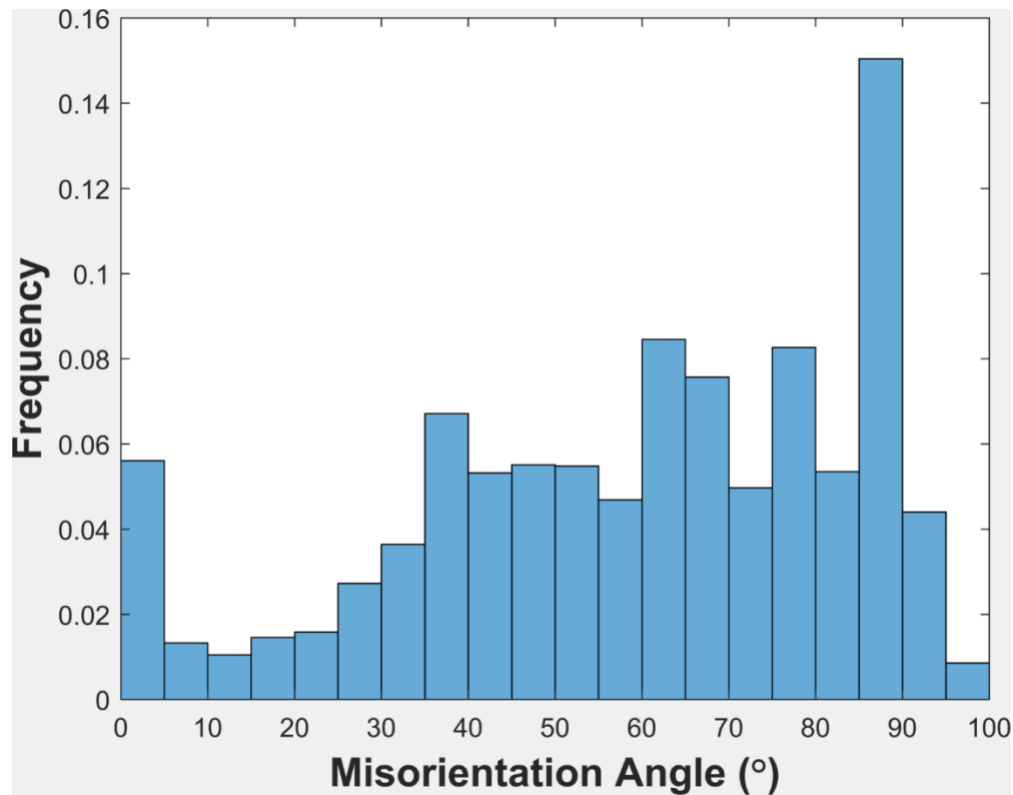


**Figure S12. Misorientation angle histogram showing the distribution of grain boundary misorientation angle in a representative  $\text{CH}_3\text{NH}_3\text{PbI}_3$  thin film.**

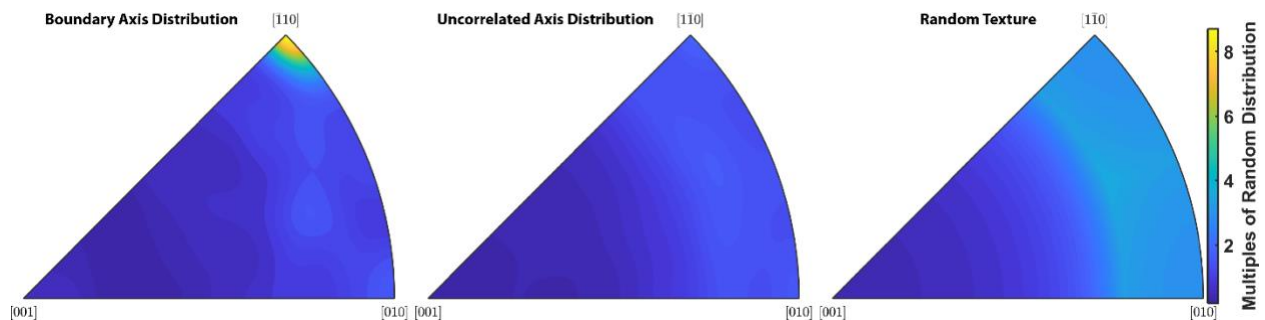


**Figure S13. Grain boundary misorientation axis distribution showing preferred orientation along [110] direction. Uncorrelated axis distribution is calculated using the uncorrelated misorientation (from points far from each other) and the underlying orientation distribution function. Misorientation axis distribution for random texture was calculated using random orientation distribution and crystal symmetry in the film.**

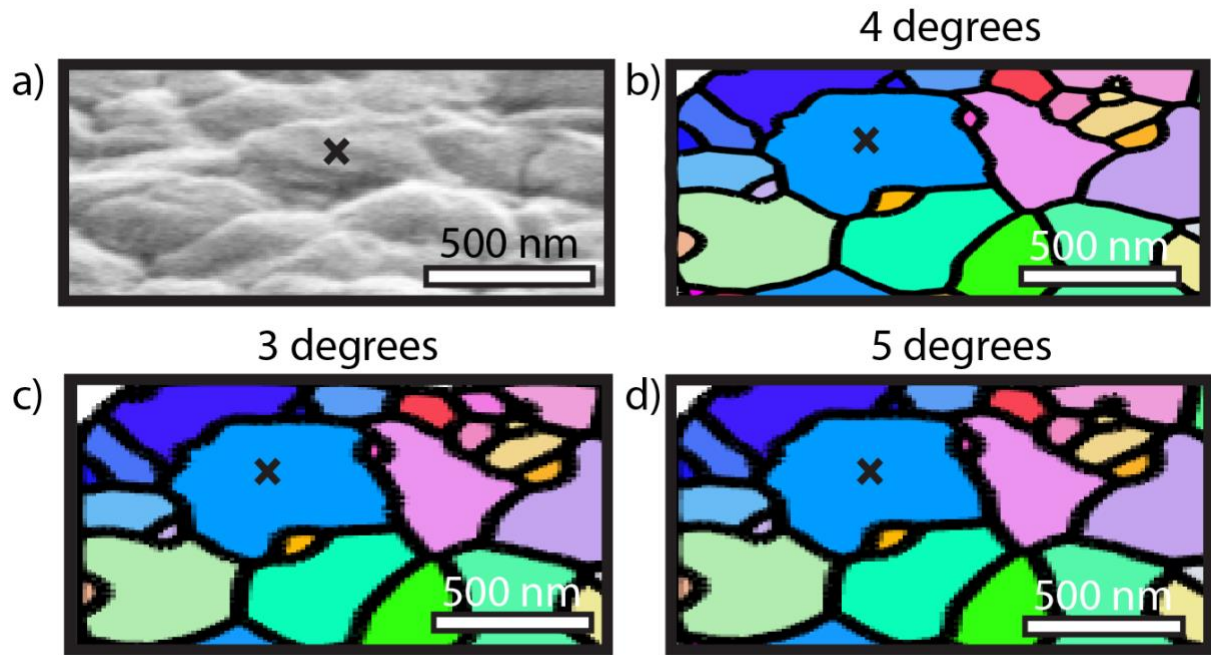


**Figure S14. (a) SEM image at 40 degrees tilt and corresponding grains identified at different thresholds; (b) 4°, (c) 3° and (d) 5°; and plotted with their mean grain orientation. The grain marked with “X” represents the grain in Figure 3a in the main text.**

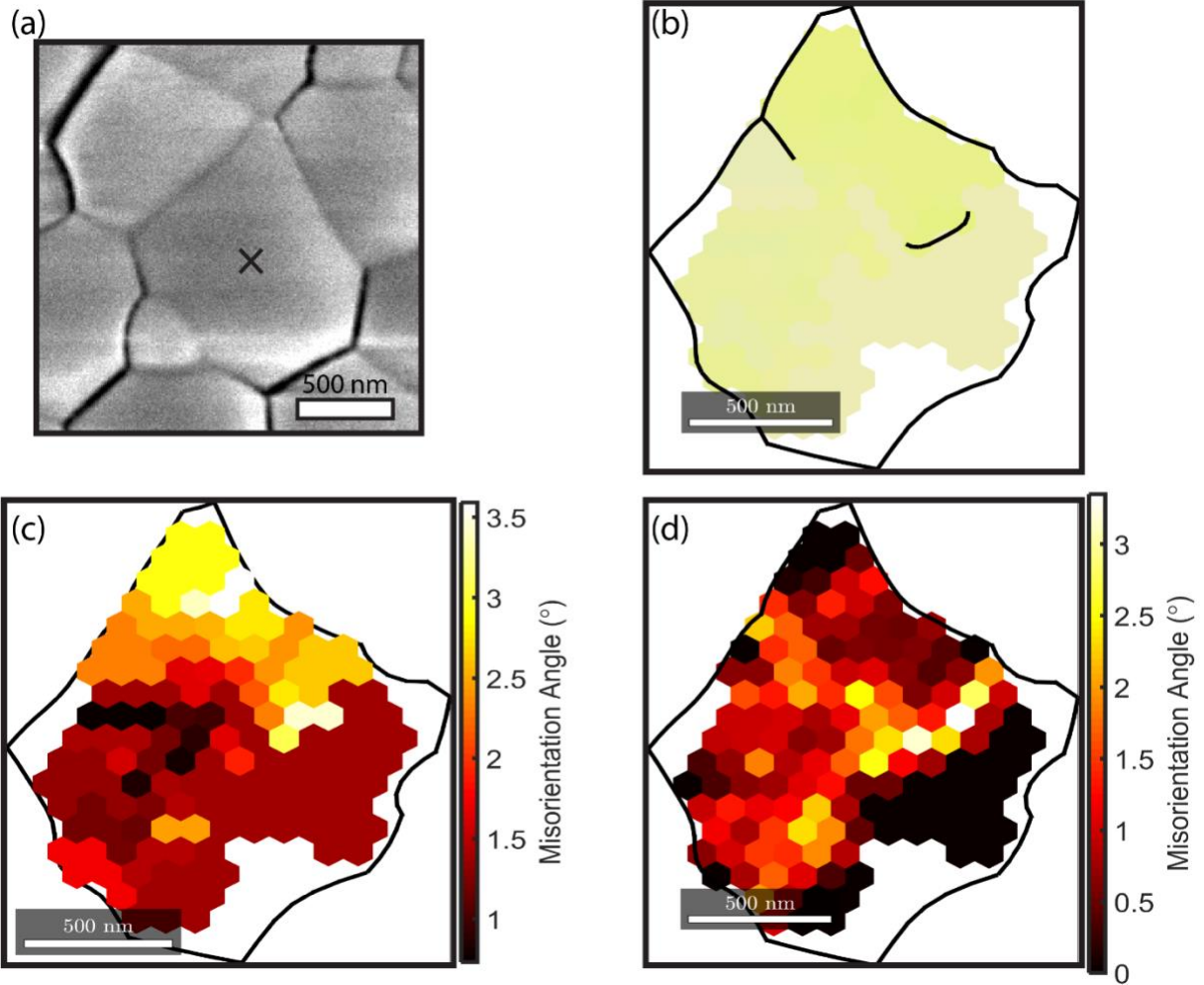


**Figure S15. (a) High-resolution SEM image of a grain along with (b) Inverse Pole Figure (IPF) with sub-grain boundaries. (c) Kernel average misorientation (KAM) and (d) misorientation with respect to mean grain orientation of the same grain in (a) and (b). The grains were identified using a 4° threshold. The grains in (b), (c) and (d) correspond to the grain marked with “X” in the (a).**

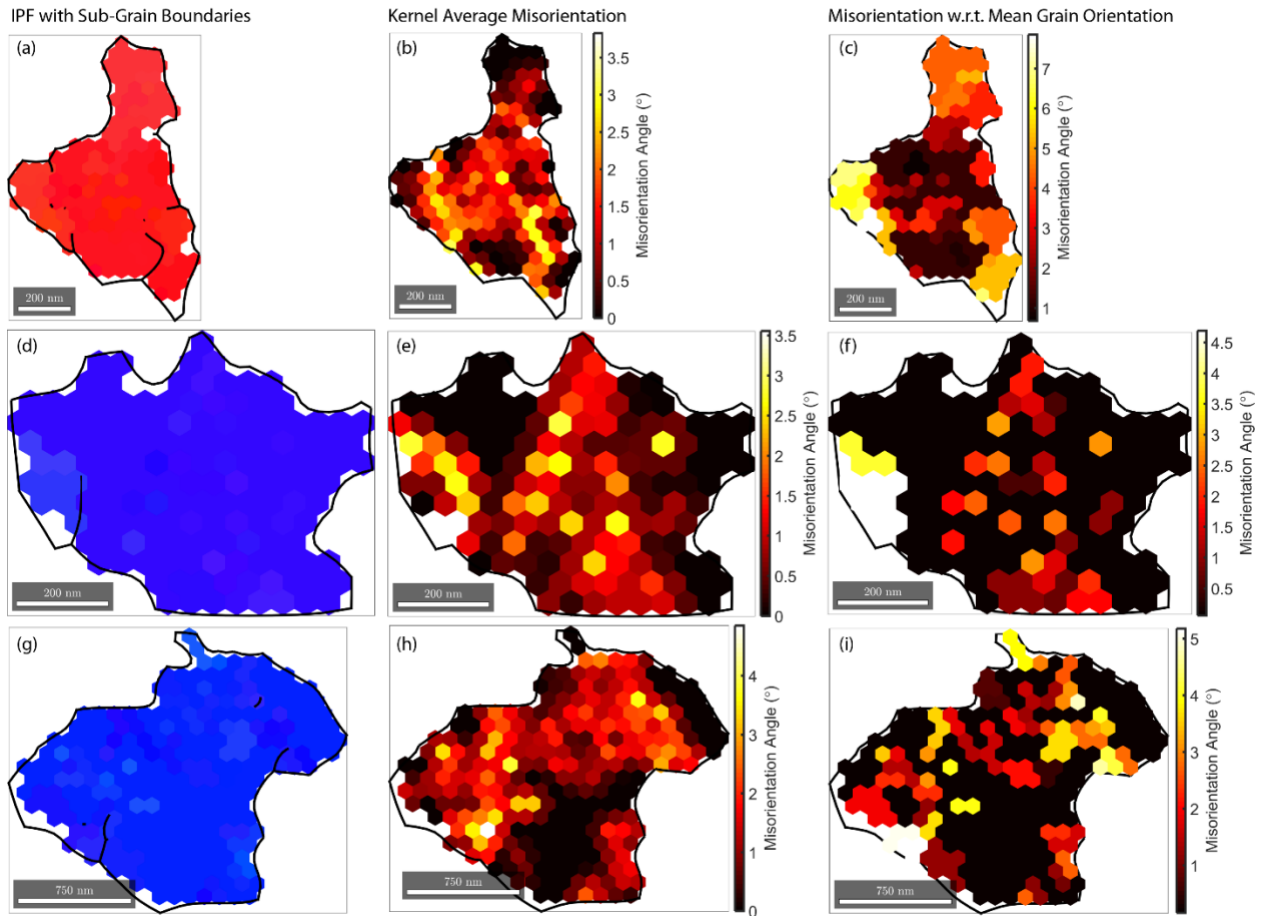


**Figure S16. Inverse Pole Figure (IPF) with sub-grain boundaries (a, d, g), kernel average misorientation (b, e, h) and misorientation with respect to mean grain orientation (c, f, i) for three different grains from different EBSD scans.**

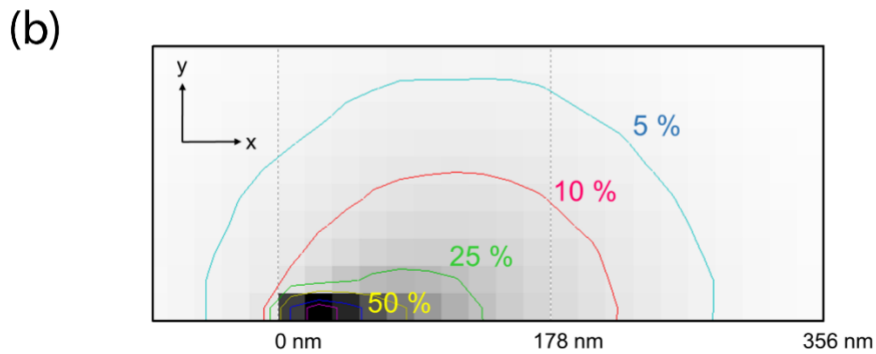
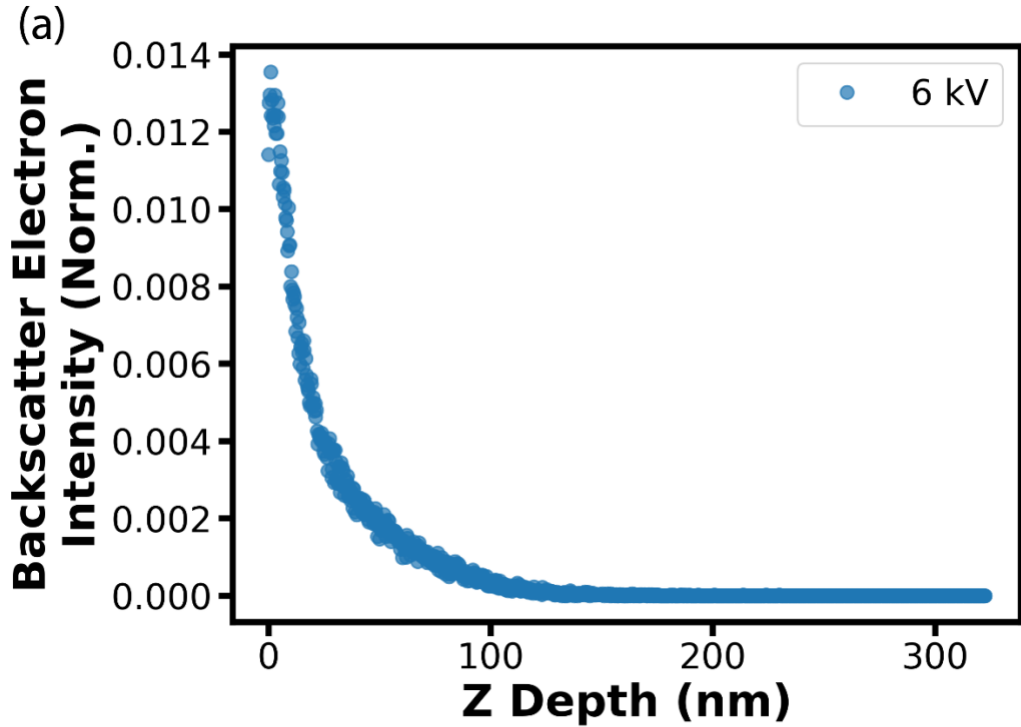


**Figure S17. Monte-Carlo simulation (using CASINO<sup>12</sup>) of electron interaction with  $\text{CH}_3\text{NH}_3\text{PbI}_3$  showing backscatter electron intensity as a function of (a) z-depth in the film at 6kV accelerating voltage. The simulation was performed in traditional EBSD geometry (70° electron incidence with respect to the surface normal). This shows that the traditional EBSD geometry is more surface sensitive with a higher probability of backscattered electrons escaping from the perovskite surface. (b) X-Y plane profile of the back-scattered electron beam energy at 70° electron incidence with respect to the surface normal, showing ~37% backscattered electron energy distributed ~106 nm in the X-Y plane.**

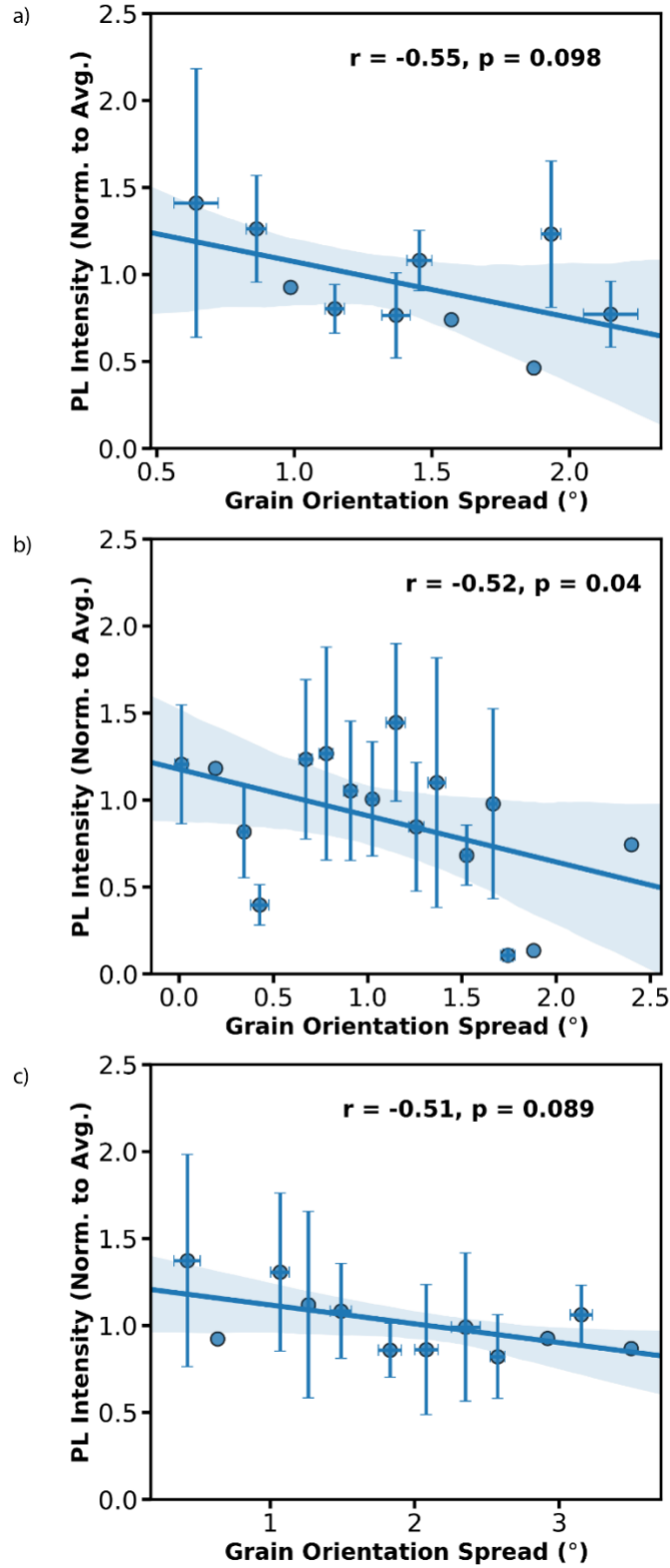


**Figure S18. Correlation plot of PL intensity as a function of grain orientation spread (GOS) showing negative correlation for three different sample sets individually comprising**

of (a) 25 grains, (b) 80 grains and (c) 38 grains. The plots show anti-correlation with the line representing a linear regression fit to the data and shaded region representing 95% confidence interval. Error bars represent the standard deviation of the average PL intensity in a specific GOS interval.

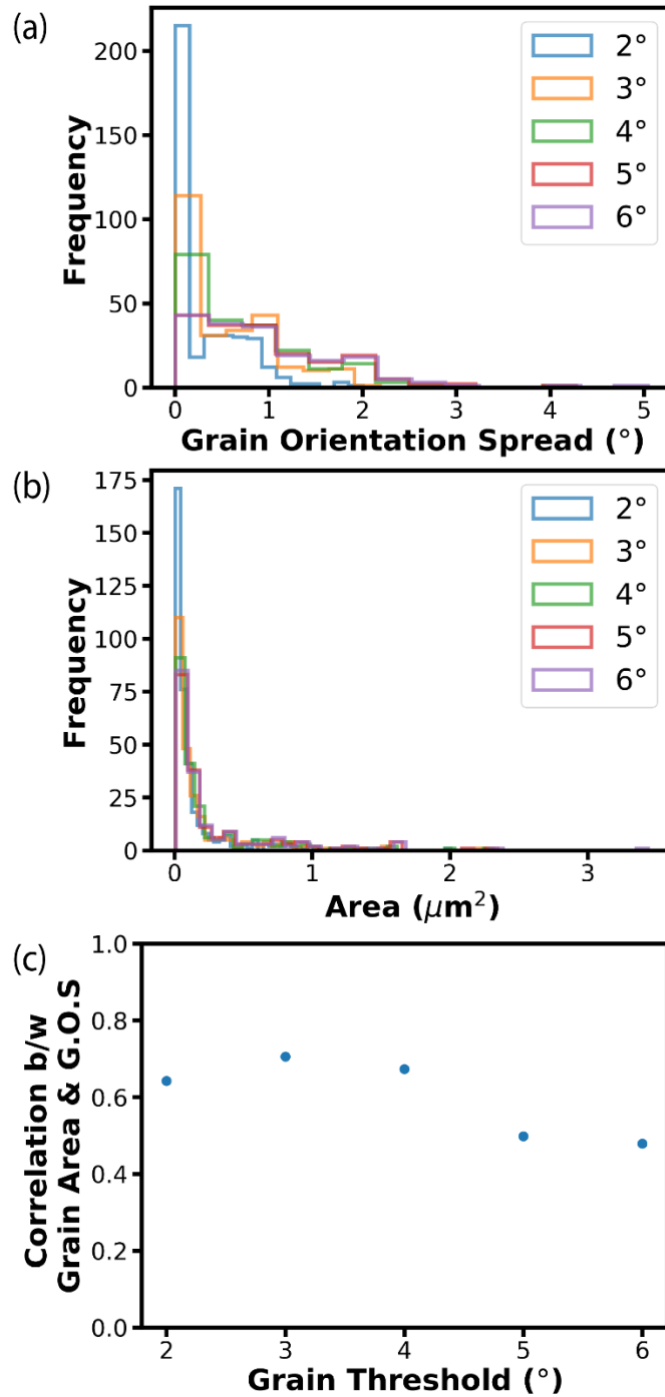


**Figure S19. Histograms of (a) grain orientation spread (GOS) and (b) grain area for different grain threshold values. (c) Correlation between grain area and GOS at different threshold values showing strong positive correlation at all different grain threshold values.**

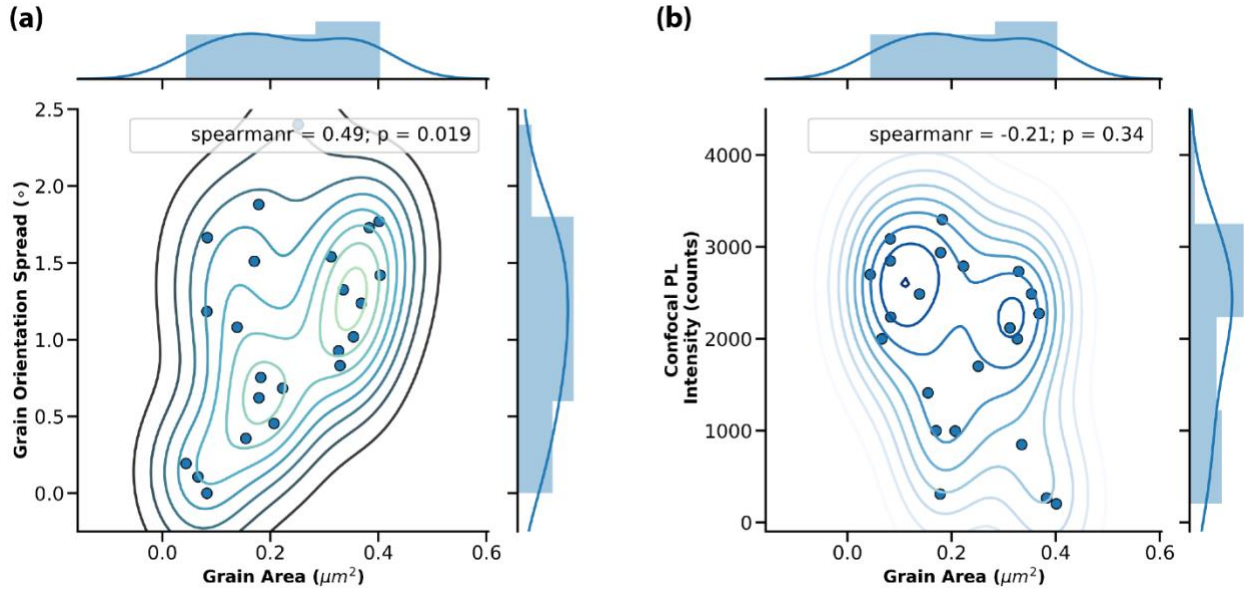


**Figure S20. (a) Grain orientation spread within grains as a function of grain area showing positive correlation with high statistical significance ( $p = 0.019$ ;  $p < 0.05$ ). (b) PL intensity measured at fluence corresponding to local trap density (see main text for more details) as a function of grain area showing very weak negative correlation with very low statistical significance ( $p = 0.34$ ;  $p > 0.05$ ). The contours in (a) and (b) represent the kernel density estimate.**

## References

- [1] Poglitsch A, Weber D. Dynamic disorder in methylammoniumtrihalogenoplumbates (II) observed by millimeter-wave spectroscopy. *J. Chem. Phys.* 1987;*87*:6373–8. doi:10.1063/1.453467.
- [2] Baikie T, Fang Y, Kadro JM, Schreyer M, Wei F, Mhaisalkar SG, et al. Synthesis and crystal chemistry of the hybrid perovskite (CH<sub>3</sub>NH<sub>3</sub>)PbI<sub>3</sub> for solid-state sensitised solar cell applications. *J. Mater. Chem. A* 2013;*1*:5628. doi:10.1039/c3ta10518k.
- [3] Humphreys FJ, Huang Y, Brough I, Harris C. Electron backscatter diffraction of grain and subgrain structures - resolution considerations. *J. Microsc.* 1999;*195*:212–6.
- [4] Krieger Lassen NC. Source point calibration from an arbitrary electron backscattering pattern. *J. Microsc.* 1999;*195*:204–11. doi:10.1046/j.1365-2818.1999.00581.x.
- [5] Nowell MM, Wright SI. Orientation effects on indexing of electron backscatter diffraction patterns. *Ultramicroscopy*, vol. 103, 2005, p. 41–58. doi:10.1016/j.ultramic.2004.11.012.
- [6] Bachmann F, Hielscher R, Schaeben H. Texture Analysis with MTEX – Free and Open Source Software Toolbox. *Solid State Phenom.* 2010;*160*:63–8. doi:10.4028/www.scientific.net/SSP.160.63.
- [7] Nolze G, Hielscher R. Orientations - Perfectly colored. *J. Appl. Crystallogr.* 2016;*49*:1786–802. doi:10.1107/S1600576716012942.
- [8] Bachmann F, Hielscher R, Schaeben H. Grain detection from 2d and 3d EBSD data- Specification of the MTEX algorithm. *Ultramicroscopy* 2011;*111*:1720–33. doi:10.1016/j.ultramic.2011.08.002.
- [9] van der Walt S, Schönberger JL, Nunez-Iglesias J, Boulogne F, Warner JD, Yager N, et al. scikit-image: image processing in Python. *PeerJ* 2014;*2*:e453. doi:10.7717/peerj.453.
- [10] James G, Witten D, Hastie T, Tibshirani R. *An Introduction to Statistical Learning with Applications in R.* n.d.Springer; . doi:10.1007/978-1-4614-7138-7.
- [11] Jones, E., Oliphant, E., Peterson P et al. *SciPy: Open Source Scientific Tools for Python* 2001.
- [12] Demers H, Poirier-Demers N, Couture AR, Joly D, Guilmain M, de Jonge N, et al. Three-dimensional electron microscopy simulation with the CASINO Monte Carlo software. *Scanning* 2011;*33*:135–46. doi:10.1002/sca.20262.

# Appendix B: Supplementary Information for Chapter 3

## Experimental Procedures

### Materials and Methods

Perovskite precursor solutions were prepared and deposited according to method reported by Eperon *et al.*<sup>1,2</sup> FAI (Greatcell), DMAI (Greatcell), CsI (Sigma Aldrich), PbI<sub>2</sub> (TCI), PbBr<sub>2</sub> (Sigma) and PbCl<sub>2</sub> (TCI) were dissolved in anhydrous DMF & DMSO (ratio of 3:1 v/v) to produce a 1M solution of FA<sub>x</sub>Cs<sub>1-x-y</sub>DMA<sub>y</sub>Pb(I<sub>0.8</sub>Br<sub>0.2</sub>)<sub>3</sub>. The small amount of Cl added is in stoichiometric excess (6 mg for a 1mL solution).

Perovskite solutions of varying A site composition (DMA10, Ctrl 67/33 and Ctrl 80/20) were made by tuning the amount of FAI, CsI and DMAI according to the formula above.

All precursors were used as purchased and stored and mixed in a Nitrogen glovebox.

Perovskite thin films were prepared on plasma/UV-Ozone cleaned glass. The solution was deposited on top of the substrate and spun at 5000 rpm for 60 s. At ~35 s remaining, anhydrous methyl acetate antisolvent was dropped from above. The thin films were then annealed at 100 C for 30 mins. The thin films were prepared in a Nitrogen filled glovebox.

### Time-of-flight secondary-ion mass spectrometry (TOF-SIMS)

TOF-SIMS data was collected using IONTOF TOF-SIMS 5. Bi<sup>3+</sup> was used as primary ion for TOF-SIMS analysis. The primary ion dosage used for depth profile was  $\sim 1.5 \times 10^{11}$  ions/cm<sup>3</sup>. The measurement was performed in high mass resolution mode. The sputtering was done using Ar (at 20 keV) with a cluster size of 1000. The sputtering ion dosage used was  $\sim 6.1 \times 10^{13}$  ions/cm<sup>3</sup>. An area of 500 x 500 um was sputtered and a raster size of 100 x 100 um within the sputtered area was used for analysis. Identical settings were used for both positive and negative ions.

### Photoluminescence Microscopy

Local photoluminescence (PL) spectra were collected using a custom scanning confocal microscope built around a Nikon TE-2000 inverted microscope. An infinity corrected 100× dry objective (Nikon LU Plan Fluor, NA 0.9) was used for the acquisition. The sample was illuminated with a 470 nm pulsed diode laser (PDL-800 LDH-P-C-470B, 2.5 MHz, ~300 ps pulse width) and the sample PL was filtered using a 600 nm long pass filter and directed onto a Ocean Optics spectrometer (USB-2000). The sample stage was controlled using a piezo controller (Physik Instrumente E-710) and the pixel dwell time was 10-100 ms.

## **Photo-induced Force Microscopy (PiFM)**

A Molecular Vista VistaScope coupled to a LaserTune QCL was used for PiFM imaging. The PiFM was operated in sideband mode where the first and second mechanical resonance frequencies at 320 kHz and 1.9 MHz of a Si cantilever with Pt coating were used to detect the photoinduced force and surface topography, respectively. The spatial resolution of the hyperspectral image acquired was  $256 \times 256$  pixels /  $512 \times 512$  pixels. The PiFM spectra was collected by sweeping the laser from 760 to  $1875 \text{ cm}^{-1}$ . The PiFM imaging was then carried out by keeping the laser at  $1714 \text{ cm}^{-1}$ , corresponding to the C=N stretch in FA (formamidinium).

## **Data Analysis**

TOF-SIMS data were analyzed using commercial software provided by IONTOF. PL microscopy data were analyzed using an inhouse software that is openly available online at [https://github.com/SarthakJariwala/Python\\_GUI\\_apps](https://github.com/SarthakJariwala/Python_GUI_apps). All the data were then plotted and analyzed further in python using numpy,<sup>3</sup> matplotlib,<sup>4</sup> seaborn,<sup>5</sup> and seaborn-image.

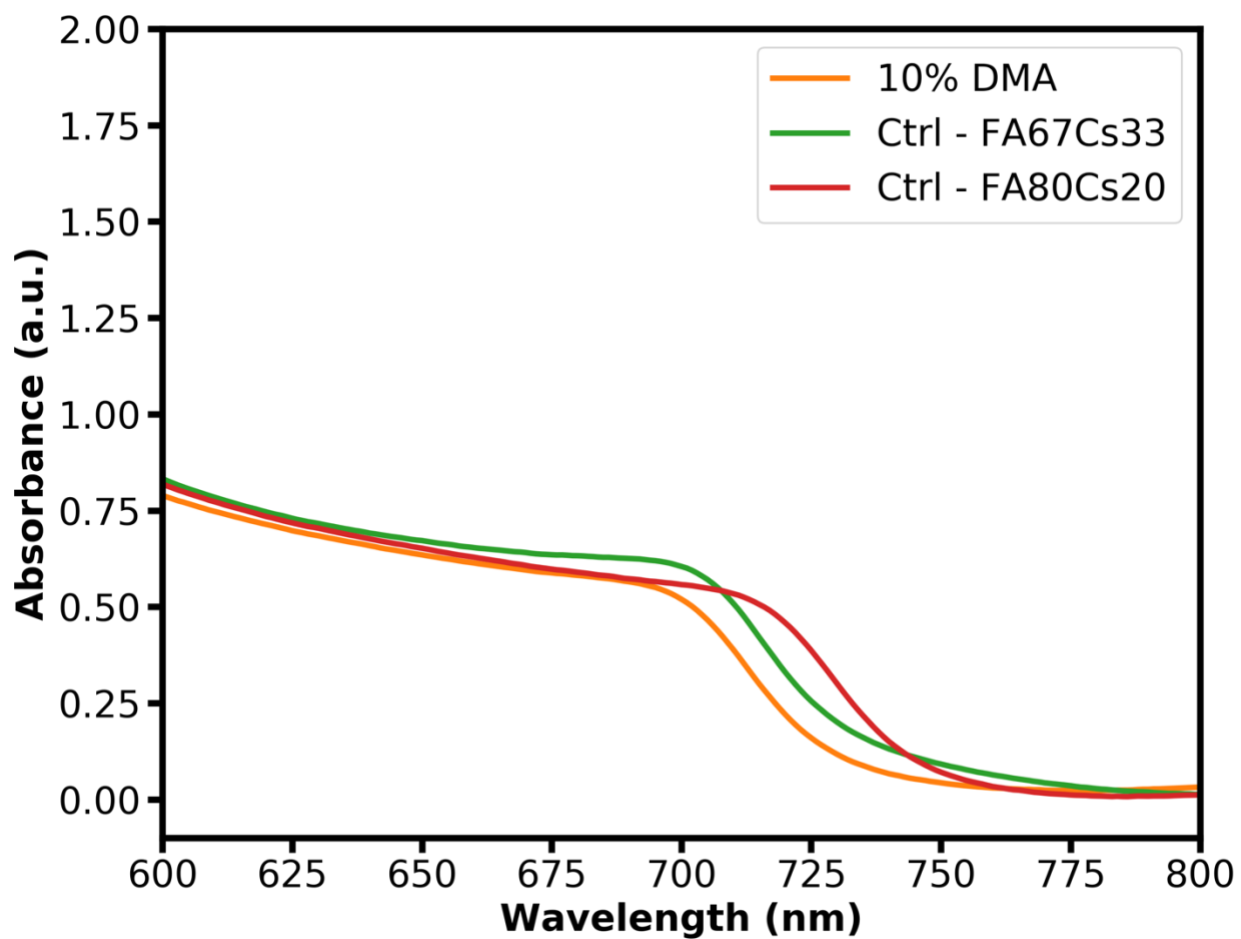
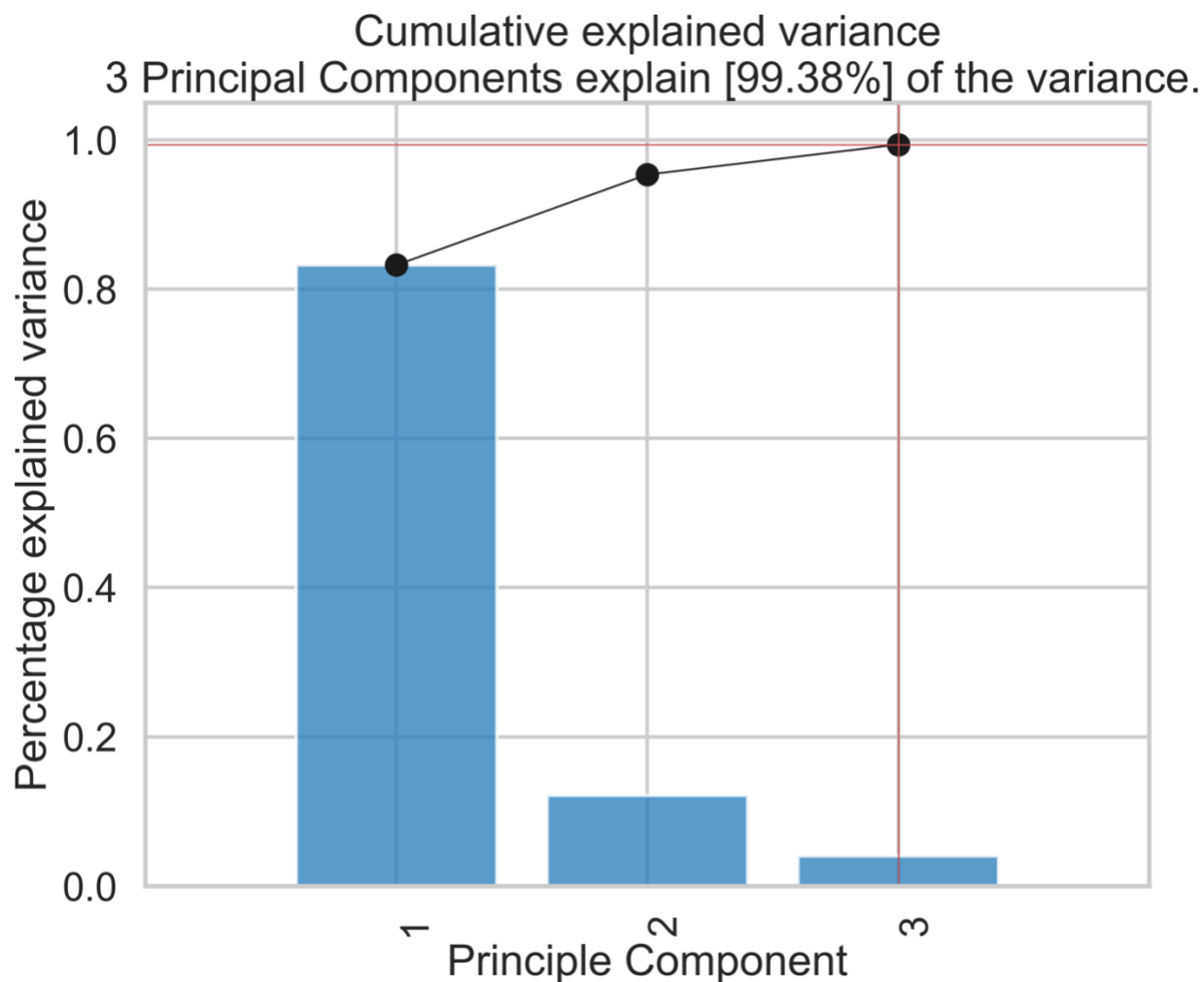
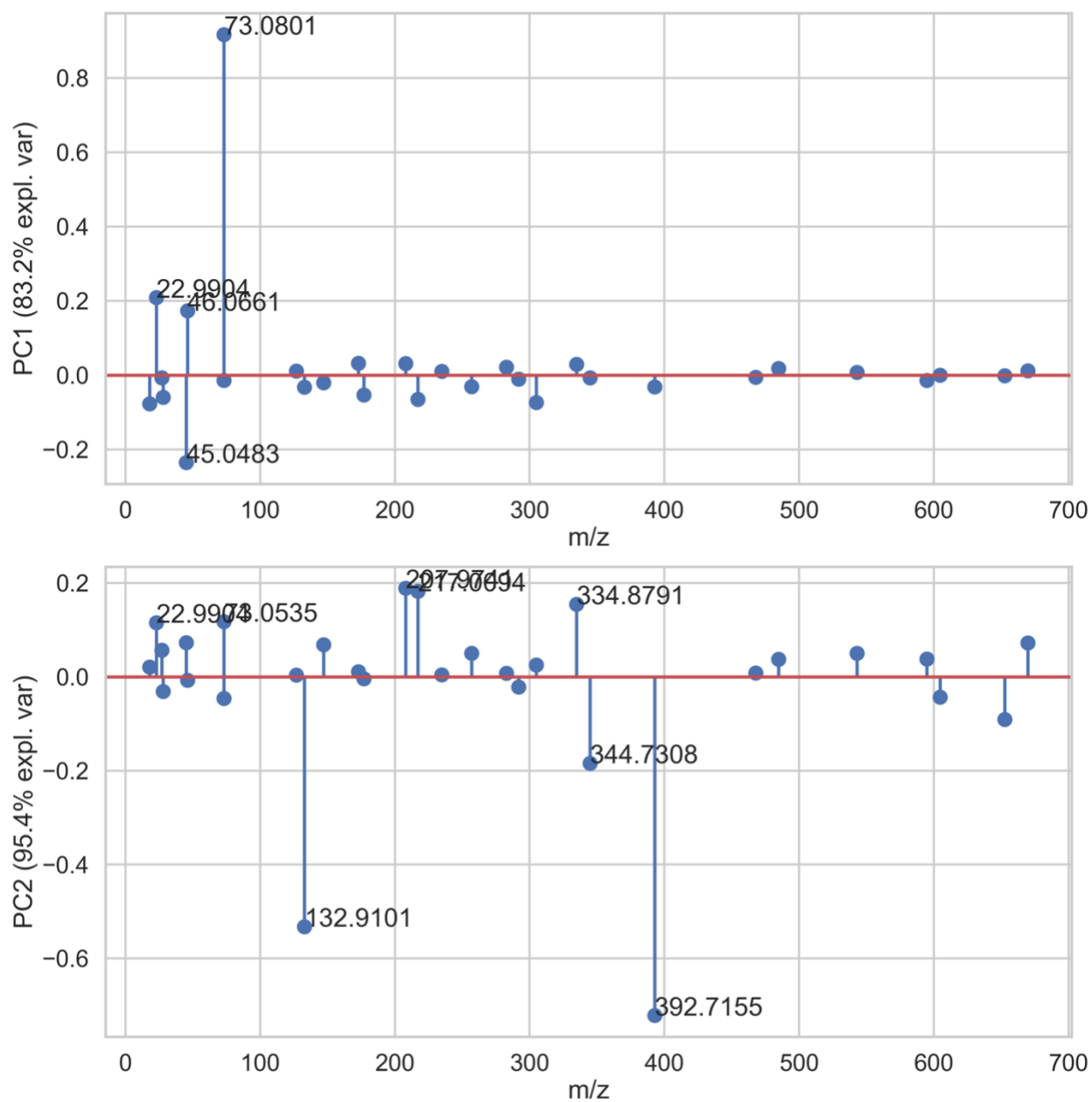


Figure S1. UV-Vis absorption spectra of DMA10, Ctrl 67/33 and Ctrl 80/20 thin films.



**Figure S2. Cumulative explained variance observed in the TOF-SIMS spectra of DMA 10, Ctrl 67/33 and Ctrl 80/20 thin films. 3 principal components explain over 99% of the observed variance in the TOF-SIMS spectra.**



**Figure S3. Plot of loadings for the scores of first (top) and second (bottom) principal component. Only peaks contributing to >0.1 are labelled in the figure.**

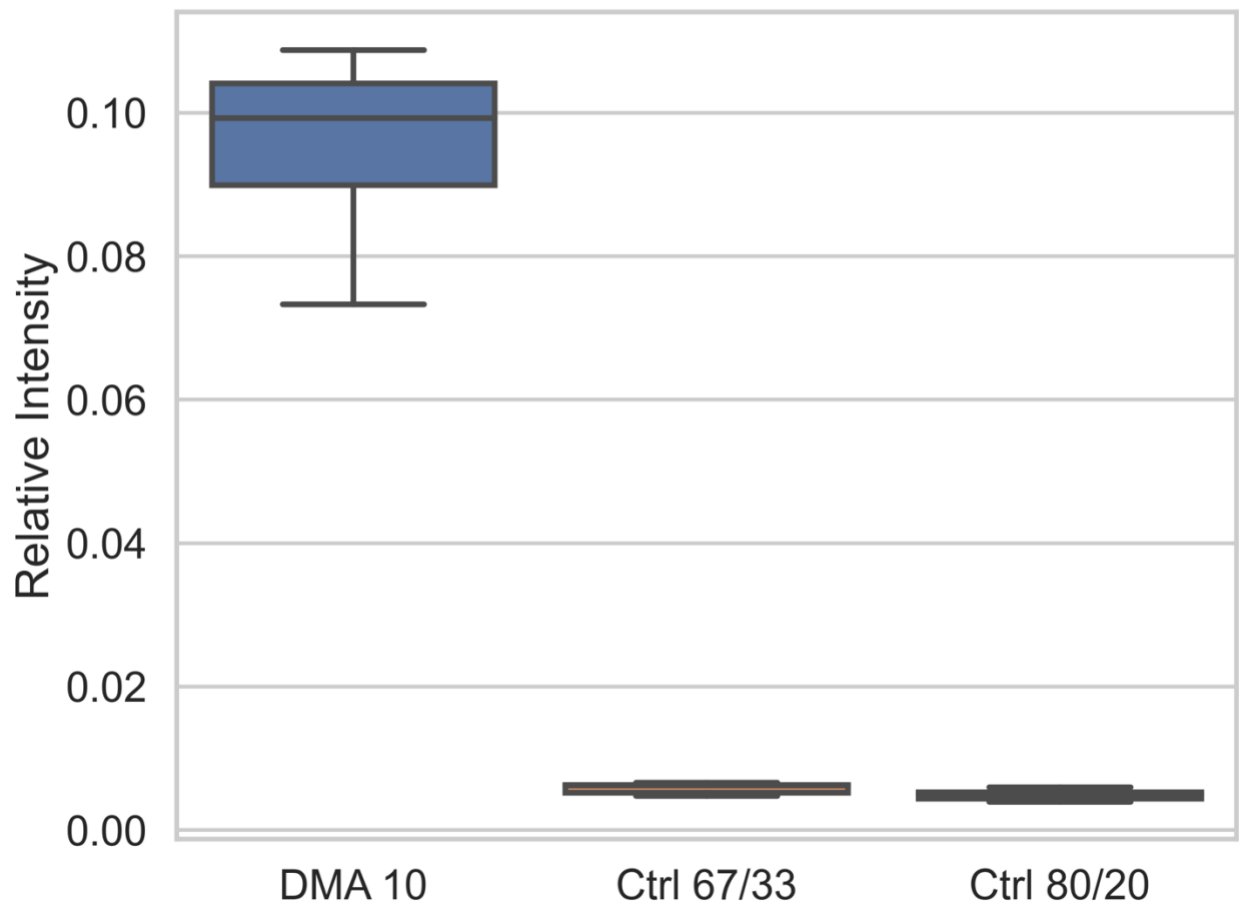
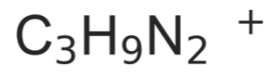


**Figure S4. Normalized relative intensity of  $\text{C}_3\text{H}_9\text{N}_2^+$  peak spectra ( $m/z = 73.08$ ) for DMA10, Ctrl 67/33 and Ctrl 80/20 thin films.**

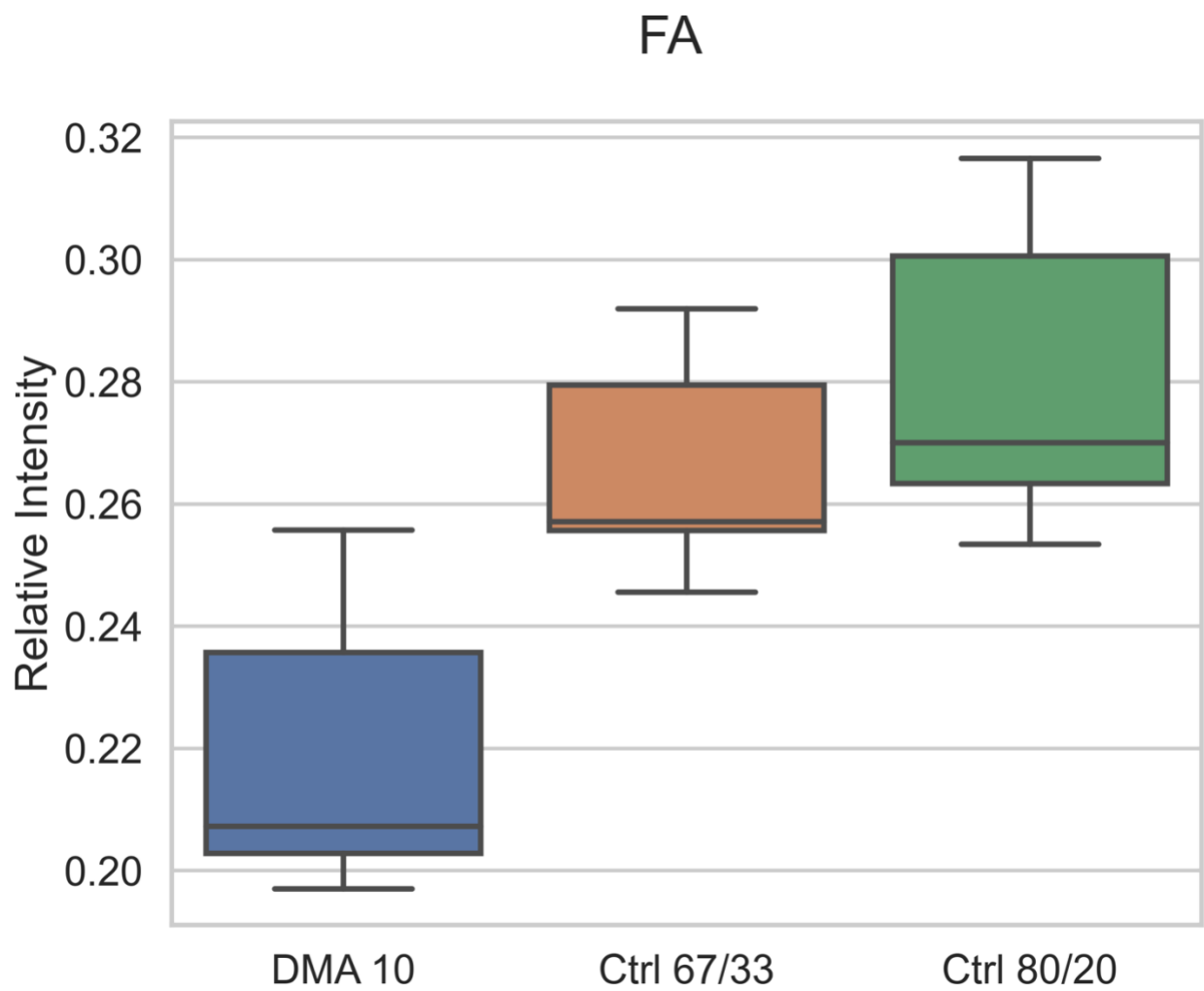


**Figure S5. Normalized relative intensity of FA peak spectra ( $m/z = 45.05$ ) for DMA10, Ctrl 67/33 and Ctrl 80/20 thin films.**

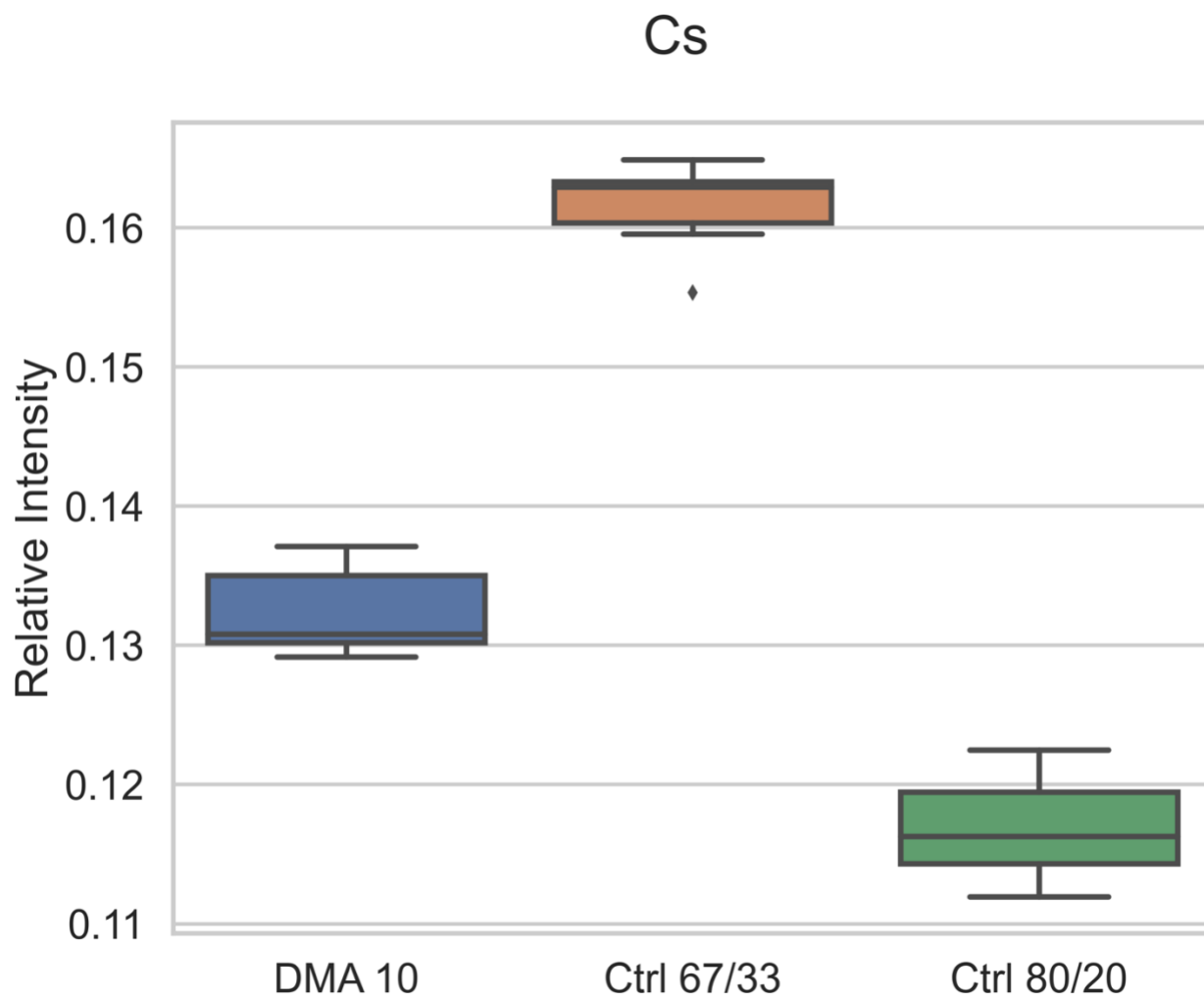


**Figure S6.** Normalized relative intensity of Cs peak spectra ( $m/z = 132$ ) for DMA10, Ctrl 67/33 and Ctrl 80/20 thin films.

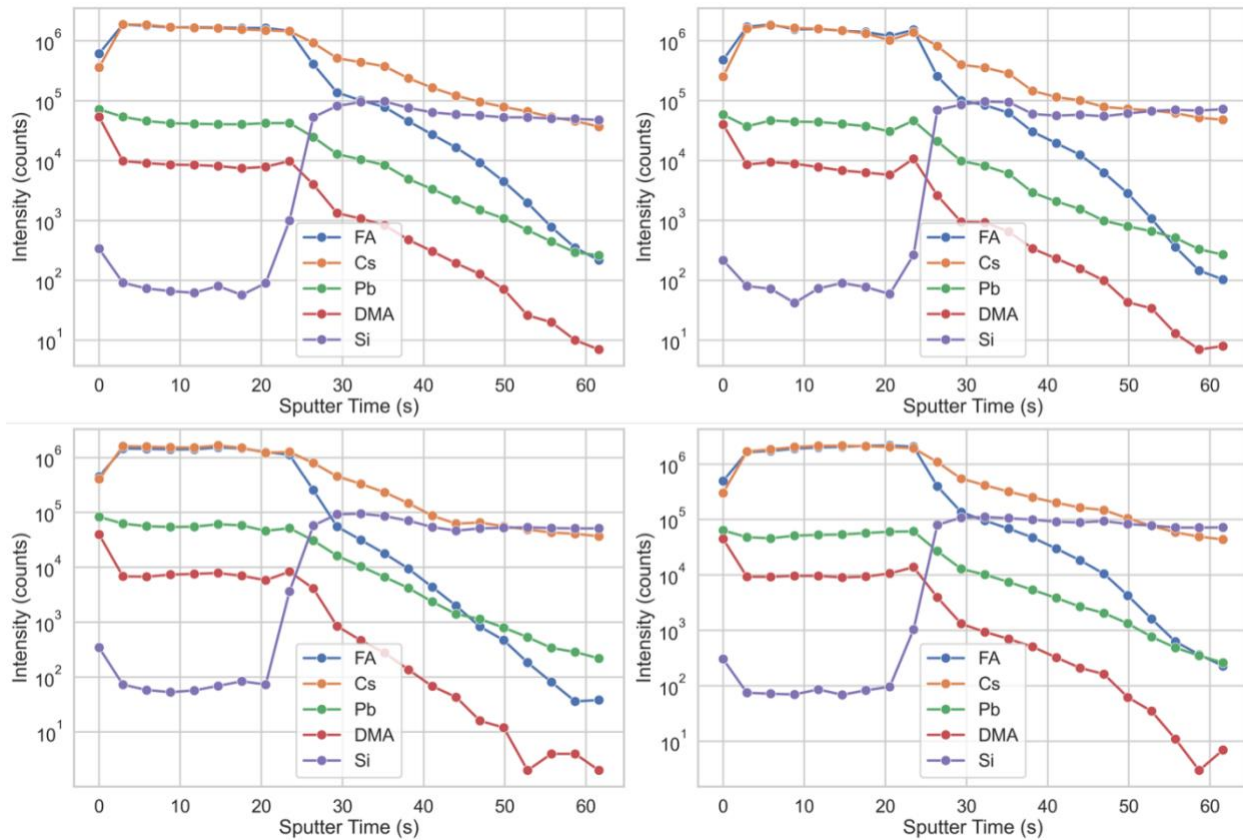


**Figure S7. TOF-SIMS depth profile of positive ions – FA, Cs, Pb, DMA, and Si acquired on different regions of different DMA10 samples.**

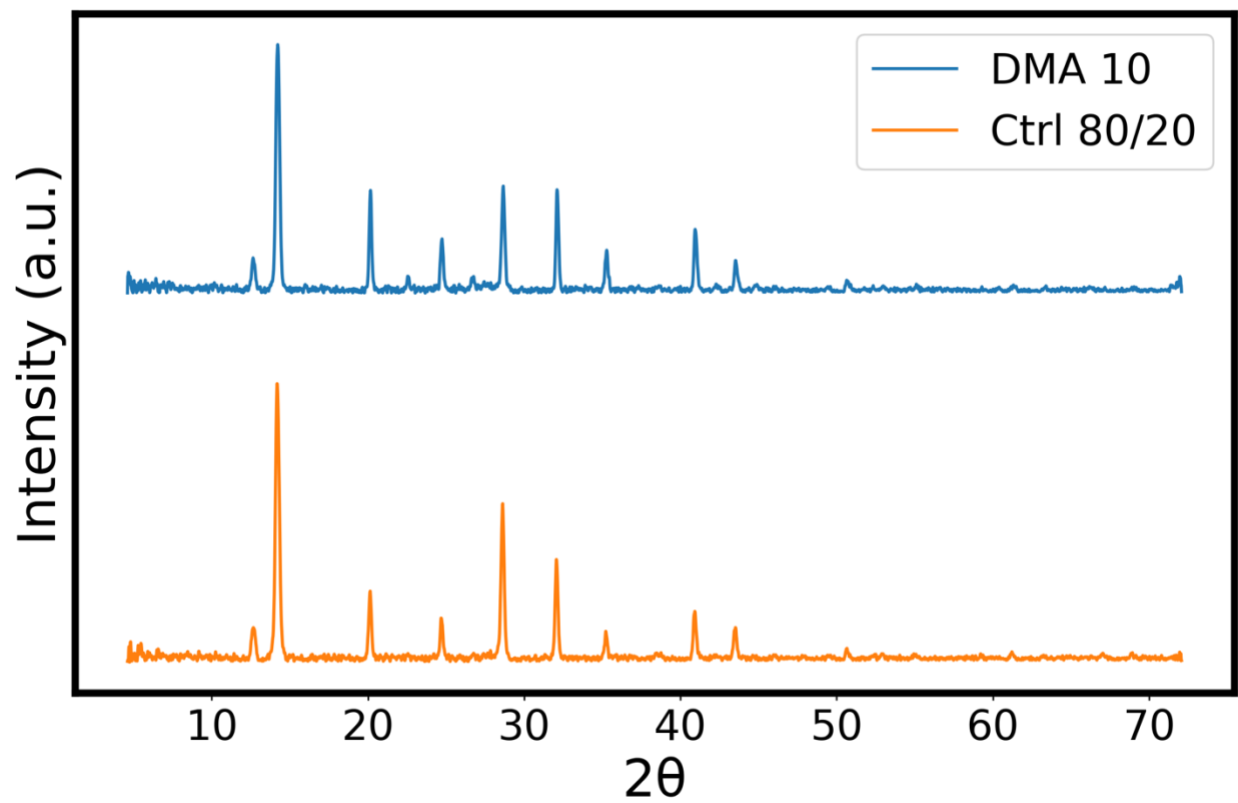
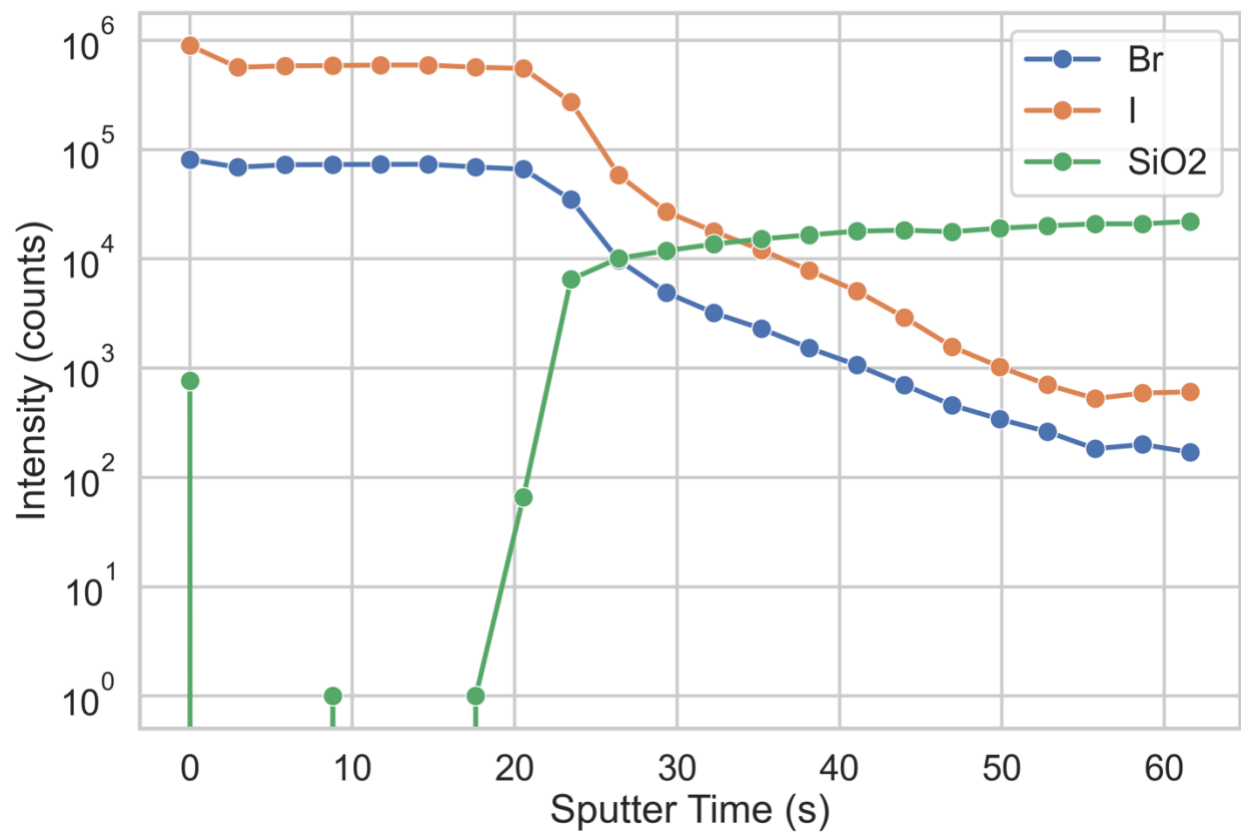
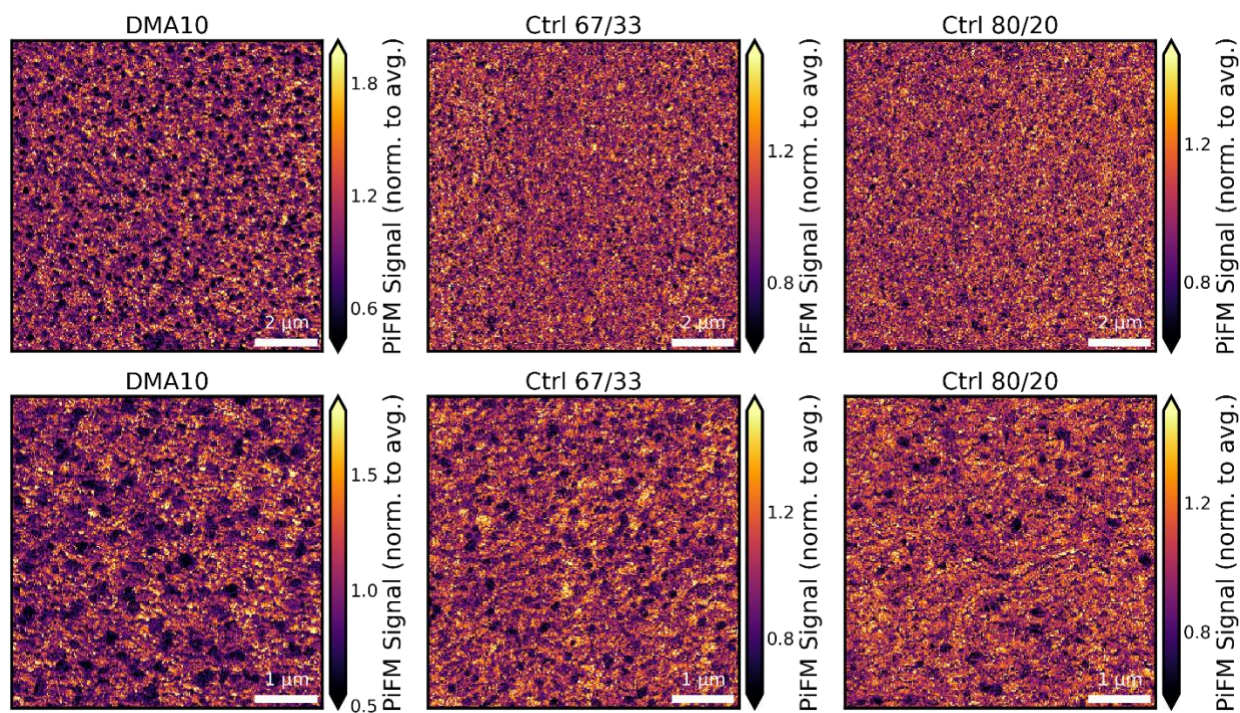


Figure S8. XRD of DMA10 and Ctrl 80/20 thin films.



**Figure S9. TOF-SIMS depth profile of negative ions – Br, I and SiO<sub>2</sub> acquired on a DMA10 thin film.**



**Figure S10. PiFM scan at  $1714\text{ cm}^{-1}$  for different DMA10, Ctrl 67/33 and Ctrl 80/20 thin films normalized to the average intensity showing larger variations in FA composition ( $1714\text{ cm}^{-1}$ ) for DMA incorporated thin films.**

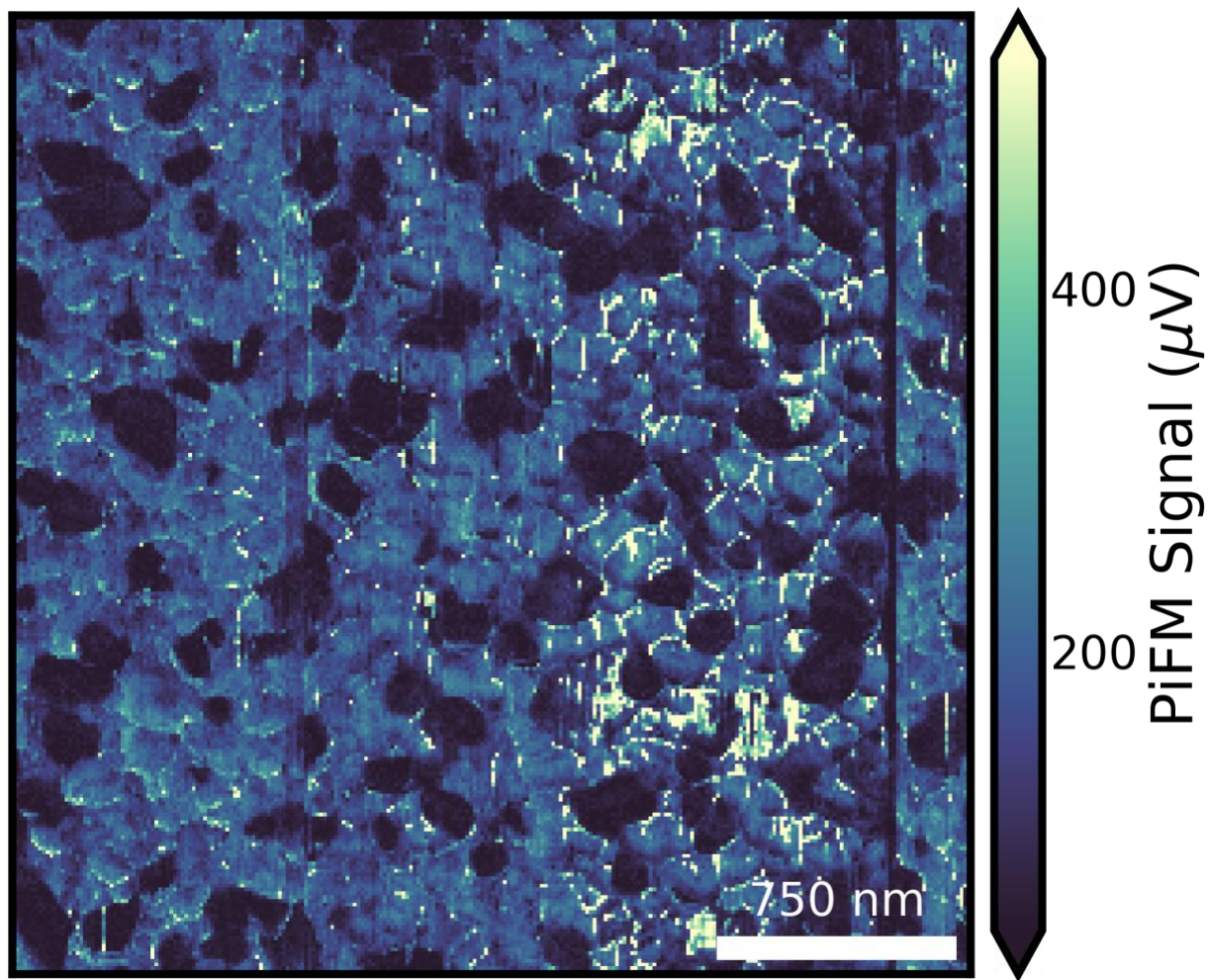


**Figure S11. Higher spatial resolution PiFM image showing heterogeneity in the local FA composition in DMA10 film, acquired at  $1714\text{ cm}^{-1}$  (tracking local FA composition).**

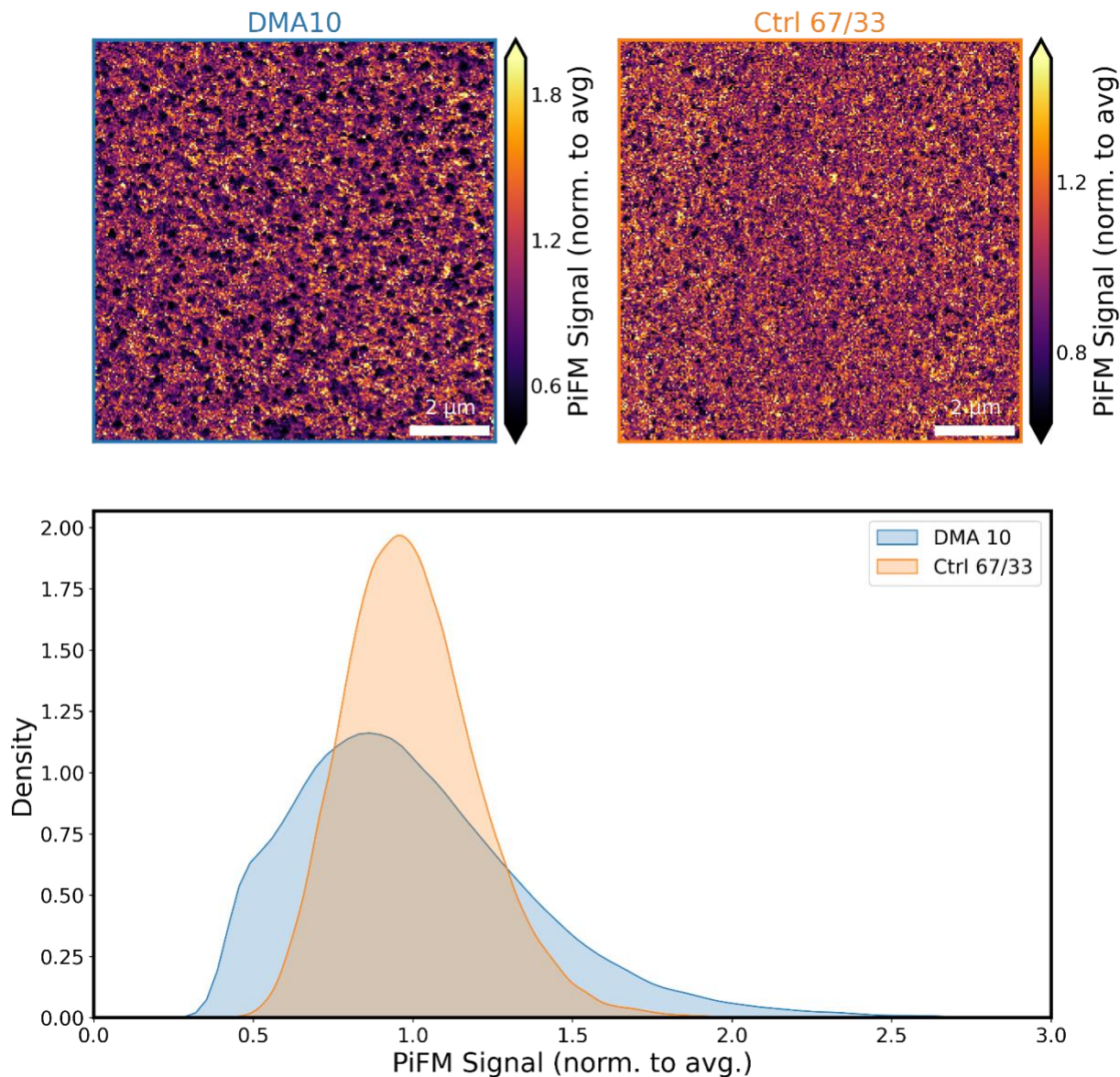


**Figure S12.** PiFM image at  $1714\text{ cm}^{-1}$  for various DMA10 (top left) and Ctrl 67/33 (top right) thin films showing that the distribution of FA intensity is more uniform in the Ctrl 67/33 thin films compared to DMA10 thin films (bottom). This indicates that the local FA heterogeneity is not merely a result of the increase in Cs concentration for the DMA10 films.

## References

- (1) Eperon, G. E.; Stone, K. H.; Mundt, L. E.; Schloemer, T. H.; Habisreutinger, S. N.; Dunfield, S. P.; Schelhas, L. T.; Berry, J. J.; Moore, D. T. The Role of Dimethylammonium in Bandgap Modulation for Stable Halide Perovskites. *ACS Energy Lett.* **2020**, 1856–1864. <https://doi.org/10.1021/acsenerylett.0c00872>.
- (2) Palmstrom, A. F.; Eperon, G. E.; Leijtens, T.; Prasanna, R.; Habisreutinger, S. N.; Nemeth, W.; Gauldin, E. A.; Dunfield, S. P.; Reese, M.; Nanayakkara, S.; et al. Enabling Flexible All-Perovskite Tandem Solar Cells. *Joule* **2019**, 3 (9), 2193–2204. <https://doi.org/10.1016/j.joule.2019.05.009>.
- (3) Harris, C. R.; Millman, K. J.; van der Walt, S. J.; Gommers, R.; Virtanen, P.; Cournapeau, D.; Wieser, E.; Taylor, J.; Berg, S.; Smith, N. J.; et al. Array Programming with NumPy. *Nature*. Nature Research September 17, 2020, pp 357–362. <https://doi.org/10.1038/s41586-020-2649-2>.
- (4) Caswell, T. A.; Droettboom, M.; Lee, A.; Hunter, J.; Andrade, E. S. de; Firing, E.; Hoffmann, T.; Klymak, J.; Stansby, D.; Varoquaux, N.; et al. Matplotlib/Matplotlib: REL: V3.3.2. **2020**. <https://doi.org/10.5281/ZENODO.4030140>.
- (5) Waskom, M.; Botvinnik, O.; O’Kane, D.; Hobson, P.; Ostblom, J.; Lukauskas, S.; Gemperline, D. C.; Augspurger, T.; Halchenko, Y.; Cole, J. B.; et al. Mwaskom/Seaborn: V0.9.0 (July 2018). **2018**. <https://doi.org/10.5281/ZENODO.1313201>.

# Appendix C: Supplementary Information for Chapter 4

## Experimental Methods

### Perovskite solution and thin film fabrication

*Perovskite Solution: 1M (3v% Formamide):* All precursors were purchased from Sigma, unless stated otherwise. Perovskite precursor solutions were formed by adding stoichiometric amounts of precursor salts FAI (greatcellsolar), CsI, PbI<sub>2</sub> (TCI/Sigma), PbBr<sub>2</sub> in DMF:DMSO (1300:640 for Cs<sub>17</sub>Br<sub>15</sub> and 1600:360 for Cs<sub>25</sub>Br<sub>20</sub>, Cs<sub>40</sub>Br<sub>30</sub> and Cs<sub>40</sub>Br<sub>40</sub>) and 60uL of Formamide to make a 2mL 1M solution.

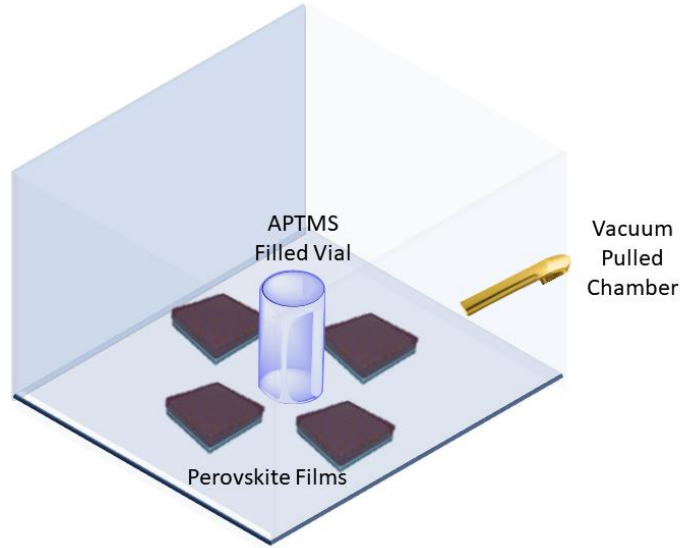
*Spin coating procedure:* The glass substrates were plasma cleaned before spin coating. Inside the glovebox, the perovskite solution was filtered before deposition. The substrates were placed on the spin coater chuck and ~25 uL of the filtered perovskite solution was deposited on top. The substrate were spun at 4000 rpm for 60 seconds. When ~35 s were remaining, ~50 uL of chlorobenzene (CB) was dropped from above. The films were then annealed on the hotplate at 100 C for 30 s and at 150 C for 10 mins.

Triple cation (FAMACs) films were made according to previously reported procedure.<sup>1</sup>

### Surface passivation with (3-Aminopropyl)trimethoxysilane or APTMS

Surface passivation with APTMS was done at RT in vacuum oven (Precision Vacuum Oven Model 19) for 5-10 mins. 1 mL of APTMS was taken in a 4 mL vial and perovskite films were placed around the vial as shown in schematic S1. Silane deposition was performed under vacuum with the gauge pressure reading -30 In. of Hg relative to atmospheric pressure. The chamber dimensions are 30.5x20.3x20.3 cm (length x width x height) but to avoid coating the entirety of the inside chamber with silanes, we cover the films and APTMS vial with a 500 mL glass jar inside the chamber. After silane deposition, the films were sonicated in anhydrous CB/Toluene for 60 s. Alternatively, instead of sonicating, films can also be washed by dynamically dropping anhydrous CB or Toluene on top of the spinning sample (2000 rpm for 60 s). Finally, the samples were dried with N<sub>2</sub>.

For solution deposition of APTMS on top of perovskite films, 5v% of APTMS was prepared in anhydrous CB. ~50-70  $\mu$ L of the prepared solution was placed on top of the prepared perovskite film and spun at 2000 rpm for 60 seconds.



**Scheme S1. Schematic of passivation with APTMS on perovskite surfaces**

### Shipping Samples for XPS/UPS Measurements

After fabrication, the samples were transferred internally through an antechamber to a solvent-free inert glovebox. The samples were covered in an Al foil and sealed in a vacuum bag (Weston 30-0101-W 8-by-12-Inch Vacuum-Sealer Bags). The samples were stored in the solvent-free glovebox until they were shipped overnight. Upon receiving the samples, they were transferred directly to a solvent-free glovebox and stored there until XPS/UPS measurements.

### Quasi-Fermi Level Splitting (QFLS)

The Shockley-Queisser theoretical QFLS limit ( $\Delta\mu_{SQ}$ ) for a bandgap of 1.63 eV is 1.353 eV at 300K. Using this theoretical limit in Ross equation<sup>2</sup>, we can calculate the QFLS based on the external photoluminescence quantum efficiency (PLQE,  $\eta_{ext}$ ) as seen in Eq. S1.

$$\Delta\mu_{\eta_{ext}} = \Delta\mu_{SQ} - kT |\ln(\eta_{ext})| \quad (S1)$$

Using measured external PLQE value of 20.1% at  $\sim 1$  sun condition with above bandgap illumination and  $T = 300$  K, we calculate QFLS  $\Delta\mu_{\eta_{ext}}$  value of 1.31 eV;  $\sim 97\%$  of the theoretical SQ limit.

The application used to calculate Shockley-Queisser limit is available online at <https://sqcalculator.herokuapp.com/> and the code is available at <https://github.com/SarthakJariwala/Shockley-Queisser-Web-App>.

### External Photoluminescence Quantum Efficiency (PLQE)

PLQE was performed in an integrating sphere (Hamamatsu C9920-02, A10094) using a 532 nm CW laser (CrystaLaser, GCL532-005-L) following the procedure reported by de Mello *et al.*<sup>3</sup> with scattering correction. For intensity dependent measurements, the incident laser intensity was attenuated using neutral density filters

## Time-resolved Photoluminescence (TRPL)

*Measurement:* TRPL was measured using a PicoQuant PicoHarp 300 TCSPC system equipped with a 470 nm pulsed diode laser (PDL-800 LDH-P-C-470B, 300 ps pulse width). The laser was pulsed at repetition rates from 100KHz to 1MHz. The PL emission was filtered using a 580 nm long-pass filter before being directed to the detector.

*TRPL fitting:* To analyze the data, we fit the time resolved PL decays to the stretched exponential decay function described in Eq S2. Physically, the stretched exponential can be interpreted as a superposition of different relaxation rates in the film and captures the distribution of local recombination rates.<sup>4-7</sup> The distribution of the relaxation rates is captured by the  $\beta$  factor in Eq S2. A  $\beta$  value closer to 0 represents a more heterogeneous distribution in the relaxation rates and a  $\beta$  value closer to 1 represents a more homogeneous distribution in the relaxation rates. If  $\beta$  is 1, then the PL decay is a single exponential. The characteristic lifetime ( $\tau_c$  in Eq S2) is the time required for the PL intensity to reach  $1/e$  of the maximum intensity. The average lifetime, or  $\langle \tau \rangle$ , for a single PL decay considers the characteristic lifetime and the  $\beta$  factor to give an average lifetime of that distribution, and is given by Eq S3. Notably  $\langle \tau \rangle$  is the lifetime most relevant for analyzing photophysics, such as evaluating PL quantum yields.<sup>8</sup>

$$I = I_0 e^{(-t/\tau_c)^\beta} \quad (\text{S2})$$

$$\langle \tau \rangle = \frac{\tau_c}{\beta} \Gamma(1/\beta), \text{ where } \Gamma(1/\beta) \text{ is the gamma function} \quad (\text{S3})$$

## Surface Recombination Velocity Calculation

The surface lifetime ( $\tau_s$ ) is determined from Eq. S2 using average PL lifetime (from PL fitting) as effective lifetime ( $\tau_e$ ) and assuming a bulk lifetime ( $\tau_b$ ) of  $8 \mu\text{s}$  (see main text). Using the surface lifetime, the upper limit of SRV, where one interface has no recombination (SRV1 = 0), can be calculated as shown in Eq. S3.<sup>9</sup> The thickness ( $W$ ) can be measured experimentally (here,  $W = 400 \text{ nm}$ ) and the diffusion coefficient ( $D$ ) can be determined using Einstein's relation ( $D = \mu kT$ ) using measured or literature mobility ( $\mu$ ) value of  $35 \text{ cm}^2\text{V}^{-1}\text{s}^{-1}$  for Cs17Br15 thin film.<sup>10</sup>

$$\frac{1}{\tau_e} = \frac{1}{\tau_b} + \frac{1}{\tau_s} \quad (\text{S4})$$

$$\tau_s = \frac{W}{\text{SRV}} + \left(\frac{4}{D}\right) (W/\pi)^2, \text{ when SRV1} = 0 \quad (\text{S5})$$

## SCAPS Simulations

SCAPS 3.3.07<sup>11,12</sup>, developed at the University of Gent, was used to perform drift-diffusion simulations. Perovskite material parameters used in the simulations are listed in Table S3. We note that although photon recycling effects are not directly included in the device model, the radiative recombination rate constant is taken from experimental value measured from escaped photons post radiative recombination.<sup>13</sup>

The general cell design was Metal/HTL/Perovskite/ETL/Metal. In our simulations, the cell was illuminated from the HTL side. As noted in the main text, we use idealized contacts (0 eV interface energy offset) with realistic material properties such as mobility, bandgap, etc. By idealized contacts with realistic transport properties, we mean that we take the electronic transport properties (e.g. carrier mobility, thickness) typical of HTL and ETL layers, and assume that versions with appropriate energy level offsets (0 eV) and SRV (as modeled) can be realized. Keeping an ideal alignment of all the contact layers allows us to explicitly simulate and understand the impact of SRV. The SRV is introduced both between the perovskite/HTL and perovskite/ETL interfaces. Although these two interfaces will likely have different SRVs in reality,<sup>14</sup> for the purposes of the simulation we kept their SRV values the same. For a full list of the parameters used, refer to Table S3.

## Data Analysis

The application code to analyze data is available as an open-source resource at [https://github.com/SarthakJariwala/Python\\_GUI\\_apps](https://github.com/SarthakJariwala/Python_GUI_apps). Data analysis and plotting was done using matplotlib,<sup>15</sup> pandas<sup>16</sup> and seaborn.<sup>17</sup>

## Scanning Electron Microscope (SEM)

SEM images were measured using a FEI Sirion SEM at 5 kV accelerating voltage. To avoid charging the samples were prepared on ITO substrates.

## Glow Discharge Optical Emission Spectroscopy (GDOES)

Depth-dependent composition was measured using a Horiba GD-Profilier-2 using a high-power radio frequency (RF) argon plasma in a 4 mm diameter anode. The plasma was operated at 30 W and a pressure of 600 Pa. Lead (Pb), Bromine (Br), Iodine (I) and Oxygen (O) were detected using the 406 nm, 149 nm, 146 nm, and 130 nm atomic emission lines, respectively.

## X-ray Photoelectron Spectroscopy (XPS)

### National Renewable Energy Laboratory Measurements:

*As received samples* were loaded into a solvent free N<sub>2</sub> glovebox with < 0.1 H<sub>2</sub>O and O<sub>2</sub>, unpackaged, left to sit for 30 minutes, and then loaded into a KF Flange tube that had been baked in a vacuum oven overnight at 150 C. The KF Flange tube was then shut and stored in the glovebox until XPS analysis, at which point it was moved to the XPS argon glovebox, loaded onto an analysis puck, grounded, and then transferred inertly to the analysis chamber.

*Control samples* were fabricated on ITO samples shipped to NREL using an analogous procedure to the one above. Specifically, dry salts were weighed out in a solvent free glovebox, solvated in another glovebox, and spun in a third glovebox. After annealing, the resulting perovskite films were left to sit in the glovebox for 5 minutes before being transferred to the same solvent free glovebox as the shipped samples. From this point on, samples were handled identical to the as received samples (left to sit for 30 min, loaded into dry KF, transferred to XPS glovebox for analysis).

*High resolution X-Ray Photoemission Spectroscopy (XPS)* measurements were performed on a Physical Electronics 5600 photoelectron spectrometer, which has been discussed in detail previously.<sup>18</sup> In order to avoid beam damage, low power I3d core level measurements were first taken with a monochromatic 15W (15kV, 1 mA) Al K $\alpha$  excitation centered at 1486.7 eV, followed by typical XPS analysis using the same source at 350 W (15 KV, ~23 mA) and UPS analysis using radiation generated by a He-gas discharge lamp (He I = 21.22 eV). All XPS core-level spectra were collected using a step size of 0.1 eV and pass energy of 23.50 eV while UPS spectra and XPS WF measurements were conducted with a step size of 0.025 and pass energy of 2.95 eV. The electron binding energy scale was calibrated using the Fermi edge and core levels of gold and copper substrates, cleaned with Argon ion bombardment. UPS spectra were numerically corrected for satellite peaks that arise from the polychromatic He I radiation. Peak areas were fit using a Gaussian-Lorentzian peak fitting algorithm with a Shirley background. WFs were determined using the intersection between the baseline and a linear fit to the main secondary electron cutoff feature. VBMS were calculated using linear extrapolation of the main feature in the valence band edge to the background signal and corrected by the shift seen in the I3d core level measurements from low to high power. Additionally, to confirm that the consistency and reproducibility across multiple methods of analysis, fits in good agreement with the first set of measurements were made using the gaussian interpolation method described above (with different sigma factor due to different instrument response functions). Spectra taken with the Al source are typically assigned an uncertainty of 0.05 eV. Spectra taken with UPS are typically assigned an uncertainty of 0.025 eV. Compositional analyses are typically assigned an uncertainty of 5%.

#### University of Arizona Measurements:

*Monochromatic XPS and UPS:* Samples from the University of Washington, prepared and shipped under inert atmosphere environment, were loaded into a clean N<sub>2</sub> glovebox (< 0.1 ppm O<sub>2</sub> and H<sub>2</sub>O and solvent-free for over a week) which allowed for the samples to be positioned on a sample stub and transferred into the high vacuum surface analysis chamber without exposure to ambient. Photoemission spectroscopies were then conducted with a Kratos Axis Ultra PES system with a base pressure of ca.  $2 \times 10^{-9}$  Torr. XPS core level (CL) spectra were acquired with a monochromatic Al K $\alpha$  source (1486.6 eV, 20 mA, 15 kV, 20 eV pass energy) at a take-off angle (TOA) of 0 degrees w.r.t. the surface normal. Average and standard deviation values for BEs and atomic ratios were determined by measuring at least three spots per sample ( $n \geq 3$ ). The XPS binding energy scale was calibrated with sputter-cleaned Cu ( $3p_{3/2} = 75.10$  eV;  $2p_{3/2} = 932.60$  eV), Au ( $4f_{7/2} = 84.00$  eV), and Ag ( $3d_{5/2} = 368.20$  eV) foils. XPS spectra were processed using the Vision 2 software package (Kratos Analytical). Relative atomic concentrations are quantified from background-corrected and systematically deconvoluted CL spectra, which are corrected for the orbital photoionization cross sections and KE-dependent analyzer transfer function. Prior to typical high intensity (20 mA, 15 kV: 300 W) XPS measurements, the secondary electron cutoff (SECO) was measured using low intensity (1 mA, 15 kV: 15 W) XPS at 3 different spots on each sample, and the I 3d and Pb 4f core level (CL) were also measured at spot 2 on each sample. These measurements were used to determine if high intensity X-ray exposure changes the sample work function, band edge positions (i.e., BE with respect to a constant Fermi Energy;  $BE_F = 0$  eV) and I/Pb ratio. For purposes of this report no discernable changes were noted for these parameters although it should be noted that extensive X-ray exposure of the perovskite film under some XPS analysis conditions can cause compositional

changes within the sampling depth, which can change the effective work function, and need to be monitored to ensure sample integrity is sustained.

After the XPS characterization the valence band region (high kinetic energy) and the SECO were measured at spot 2 using UPS with a He I excitation source (SPECS UVS 10/35), (ca.  $1.1\text{-}1.2 \times 10^{-7}$  Torr He pressure, the He discharge lamp was operated at a current of 25 mA, producing a source energy = 21.22 eV) and an analyzer pass energy of 5 eV. Samples were fixed and grounded to stainless steel stubs. Samples were biased at -10.0 V for UPS measurements to enhance the yield of photoelectrons at the low kinetic energy (LKE) edge. The Fermi energy ( $E_F$ ) for UPS measurements was calibrated with sputter-cleaned Au, and the work function of the sample determined by subtracting the spectral width ( $E_F\text{-LKE}$ ) from the excitation energy (21.22 eV), providing a value of 5.1 eV for clean Au.

To ensure maximum sensitivity and spectral contrast for determination of the VBM energy and work function of each sample He  $I_{\beta,\gamma}$  satellites were removed from these spectra. These UPS experiments used a non-monochromatic He discharge lamp excitation source, which has a primary He  $I\alpha$  emission line at 21.22 eV. The He discharge lamp also emits low-intensity He  $I\beta$  ( $E_\beta = 23.09$  eV,  $\Delta E_{\beta-\alpha} = 1.87$  eV,  $I_{\beta(\alpha)} = 1.4\text{-}1.5\%$  of the He  $I\alpha$  intensity) and He  $I\gamma$  ( $E_\gamma = 23.74$  eV,  $\Delta E_{\gamma-\alpha} = 2.52$  eV,  $I_{\gamma(\alpha)} = 0.6\text{-}0.8\%$  of the He  $I\alpha$  intensity) satellite lines, which generate photoelectrons with slightly higher kinetic energy (KE) that overlap with the primary He  $I\alpha$  - created photoemission spectrum which can effectively hide spectral features below the VB edge, and may complicate determination of the VBM energy. In order to subtract satellite photoemission features from the He  $I\alpha$  VB spectra: 1) the raw UPS data is multiplied by the relative satellite intensity ( $I_{\beta/\gamma(\alpha)}$ ) which shows slight variations due to fluctuations in He discharge lamp pressure caused by evaporation and refilling of the liquid nitrogen trap that removes trace oxygen from the He gas source; 2) shifted by the relative offset w.r.t. He  $I\alpha$  ( $\Delta E_{\beta/\gamma-\alpha}$ ) to lower BE, and 3) subtracted from the raw UPS data. After removal of satellite photoemission features the residual background due to secondary electron photoemission was subtracted from the UPS data using a polynomial fitting function. The valence band region was then deconvoluted with the minimum number of Gaussian peaks to adequately reproduce the data, and this data was then area normalized to reveal differences in overall spectral shape. The VB onset energy was estimated using a Gaussian Interpolation protocol where VBM is determined to occur at  $3.5\sigma$  on the high kinetic energy side of the highest KE VB peak where  $\sigma \sim$  the full width at half-maximum of this peak.<sup>19</sup> The values of VBM shown here are similar to those shown previously by Tao and Olthoff using a monochromatic He I discharge.<sup>20</sup>

#### University of Washington Measurements:

High resolution XPS and angle resolved XPS at University of Washington was performed using Kratos AXIS Ultra DLD XPS system on samples prepared on ITO substrates. Control samples were fabricated as described above. APTMS samples were treated with APTMS vapors for 5 mins. The angle-resolved composition for an individual sample was calculated by averaging the composition at minimum three different sites on the same sample at every photo-electron take-off angle. XPS spectra were analyzed using the Kratos Analytical software package.

**Table S1: Perovskite composition determined from XPS measurements**

<b>Made at</b>	<b>FA/A</b>	<b>Cs/A</b>	<b>Pb/A</b>	<b>(I/3)/A</b>	<b>(Br/3)/A</b>	<b>Measured</b>
<b>UW</b>	0.84	0.16	1.06	0.86	0.14	<b>Univ. of Arizona</b>
<b>UW</b>	0.83	0.17	1.07	0.86	0.14	<b>Univ. of Arizona</b>
<b>UW</b>	0.84	0.16	1.02	0.87	0.13	<b>Univ. of Arizona</b>
<b>UW</b>	0.84	0.16	1.09	0.90	0.16	<b>NREL</b>
<b>NREL</b>	0.84	0.15	1.08	0.87	0.15	<b>NREL</b>
<i><b>Average</b></i>	<i><b>0.84</b></i>	<i><b>0.16</b></i>	<i><b>1.06</b></i>	<i><b>0.87</b></i>	<i><b>0.14</b></i>	
<i><b>Std. Dev</b></i>	<i><b>0.01</b></i>	<i><b>0.01</b></i>	<i><b>0.02</b></i>	<i><b>0.02</b></i>	<i><b>0.01</b></i>	

**Table S2. XPS binding energies of N 1s signal for control and APTMS passivated Cs17Br15 thin films**

	<b>Binding Energy</b>	<b>Peak Area (RSF Corrected)</b>	<b>%</b>
<b>Control – N1s</b>	400.172 eV	7686.4	92.68
<b>Control – N1s</b>	401.542 eV	606.75	7.32
<b>APTMS – N1s</b>	400.514 eV	6932.63	87.85
<b>APTMS – N1s</b>	402.121 eV	959.049	12.15

**Table S3. SCAPS simulation parameters.**

<b>Parameter</b>	<b>Value</b>
<b>Perovskite Thickness (nm)</b>	400
<b>Dielectric Permittivity</b>	39
<b>Electron Affinity (eV)</b>	4.01
<b>Bandgap (eV)</b>	1.63
<b>Absorption Coefficient (cm<sup>-1</sup>)</b>	SCAPS Model
<b>Bulk Lifetime (ns)</b>	8000
<b>Radiative Recombination Rate Constant (cm<sup>3</sup>/s)</b>	4e-11 <sup>13</sup>
<b>Auger Rate Constant (cm<sup>6</sup>/s)</b>	0
<b>VB/CB Effective Density of States (cm<sup>-3</sup>)</b>	3e18
<b>Electron and Hole Mobility (cm<sup>2</sup>/V.s)</b>	35 <sup>10</sup>
<b>Doping Concentration (cm<sup>-3</sup>)</b>	1e12
<b>Bandgap ETL (eV)</b>	2
<b>Bandgap HTL (eV)</b>	3
<b>Electron Mobility (cm<sup>2</sup>/V.s) ETL</b>	1e-2
<b>Hole Mobility (cm<sup>2</sup>/V.s) HTL</b>	1e-4
<b>Minority Carrier Recombination Velocity from Perovskite to ETL/HTL (cm/s) – SRV</b>	Vary
<b>Thickness ETL (nm)</b>	30
<b>Thickness HTL (nm)</b>	10
<b>Interface Energy Offset ETL/HTL with Perovskite</b>	Vary (0 eV main text)
<b>VB/CB Effective Density of States (ETL and HTL) (cm<sup>-3</sup>)</b>	1e20
<b>Dielectric Constant ETL</b>	5
<b>Dielectric Constant HTL</b>	3.5
<b>Majority and Minority Carrier Recombination Velocity at Front and Back Metal Contact (cm/s)</b>	1e7
<b>Interface Energy Offset ETL/HTL with Metal Contacts (eV)</b>	0

## Supplementary Information

### TRPL additional discussion

The defects at the surface can act as traps for the photo-generated carriers in the film. As also noted by Feldmann *et al.*,<sup>21</sup> the initial drop in the PL intensity at early times is due to non-radiative recombination. We observe this fast drop in the PL intensity at early times in our control samples for a range of different compositions. This initial drop in the PL intensity reduces dramatically after APTMS passivation for all compositions studied here and we observe a nearly mono-exponential (pseudo-first order) like PL decay for Cs17Br15. These pseudo first-order radiative recombination kinetics at low excitations are consistent with the photo-doping phenomenon as proposed by Feldmann *et al.*<sup>21</sup> As the recombination rate at these low excitations is proportional to the photodoping density, the lifetime increase after surface passivation would indicate a decrease in recombination rate and hence, a reduction in the photodoping density. This reduction suggests that some of those photodoped carriers could originate from surface trapped carriers - as these surface states get passivated, they are neither accessible to non-radiative recombination, nor would there be photodoped carriers that are promoted from these states into the band inducing a monomolecular like radiative recombination.

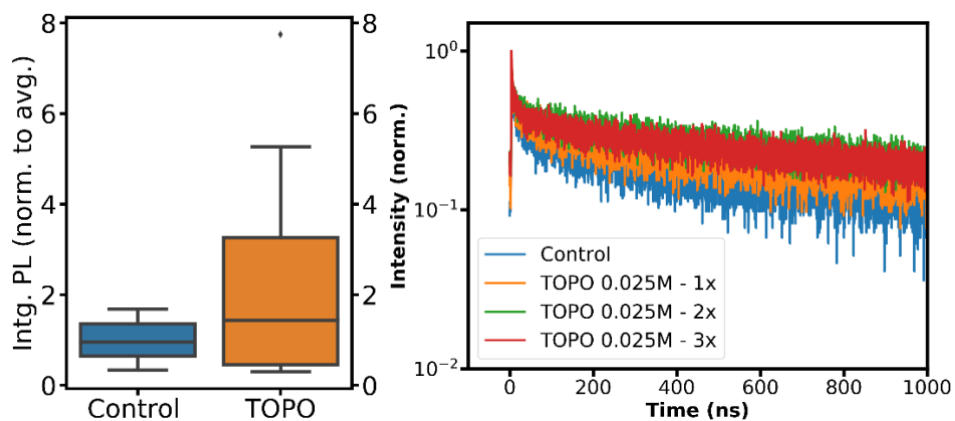


**Figure S1. Integrated PL intensity (normalized to average) and time-resolved PL decay for control Cs17Br15 and TOPO (0.025M) treated Cs17Br15 films**

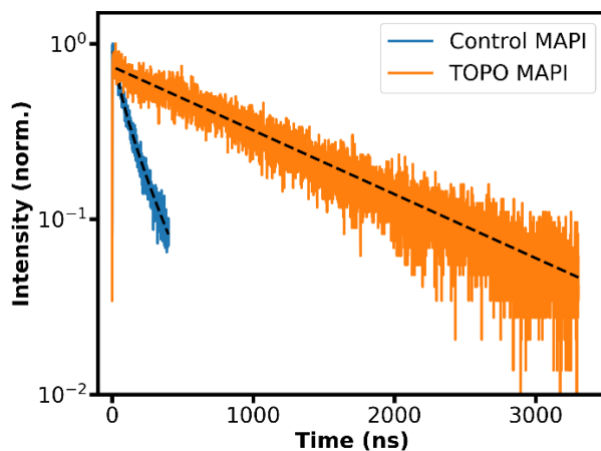


**Figure S2. Time-resolved PL decay for CH<sub>3</sub>NH<sub>3</sub>PbI<sub>3</sub> (MAPI) thin films (made acc to ref.<sup>25</sup>) before and after TOPO treatment.<sup>5</sup> The average PL lifetime improves from 137 ns (control) to 1.2 μs after TOPO treatment.**

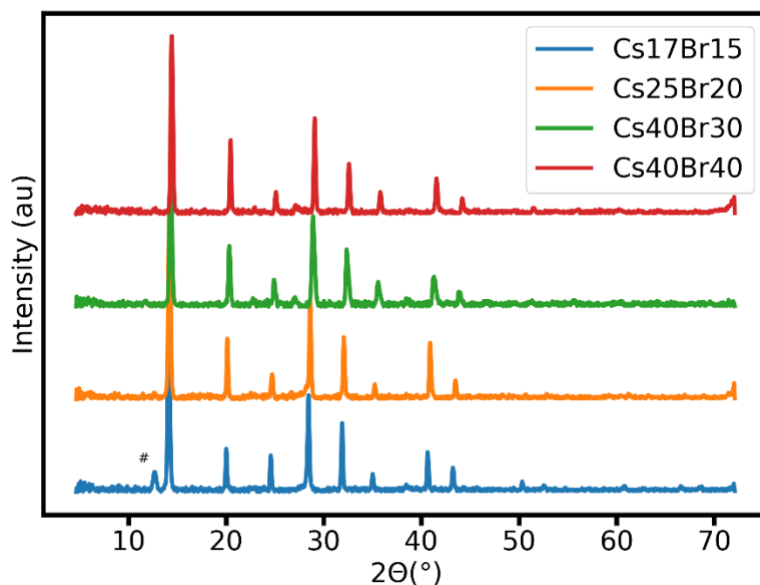


**Figure S3.** X-ray diffraction of Cs17Br15, Cs25Br20, Cs40Br30 and Cs40Br40 perovskite thin films. Peak marked with “#” represents PbI<sub>2</sub>.

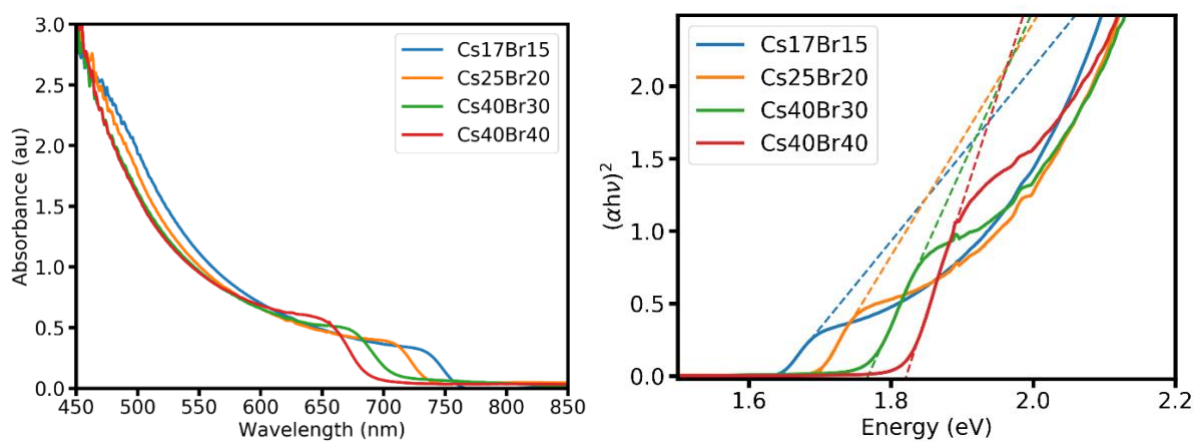


**Figure S4.** UV-Vis absorption spectra (left) and corresponding Tauc plots (right) of Cs17Br15 ( $E_g \sim 1.63$  eV), Cs25Br20 ( $E_g \sim 1.7$  eV), Cs40Br30 ( $E_g \sim 1.75$  eV) and Cs40Br40 ( $E_g \sim 1.8$  eV) perovskite thin films showing sharp absorption onsets. Tauc plot from the absorption spectra are used to determine the bandgap.

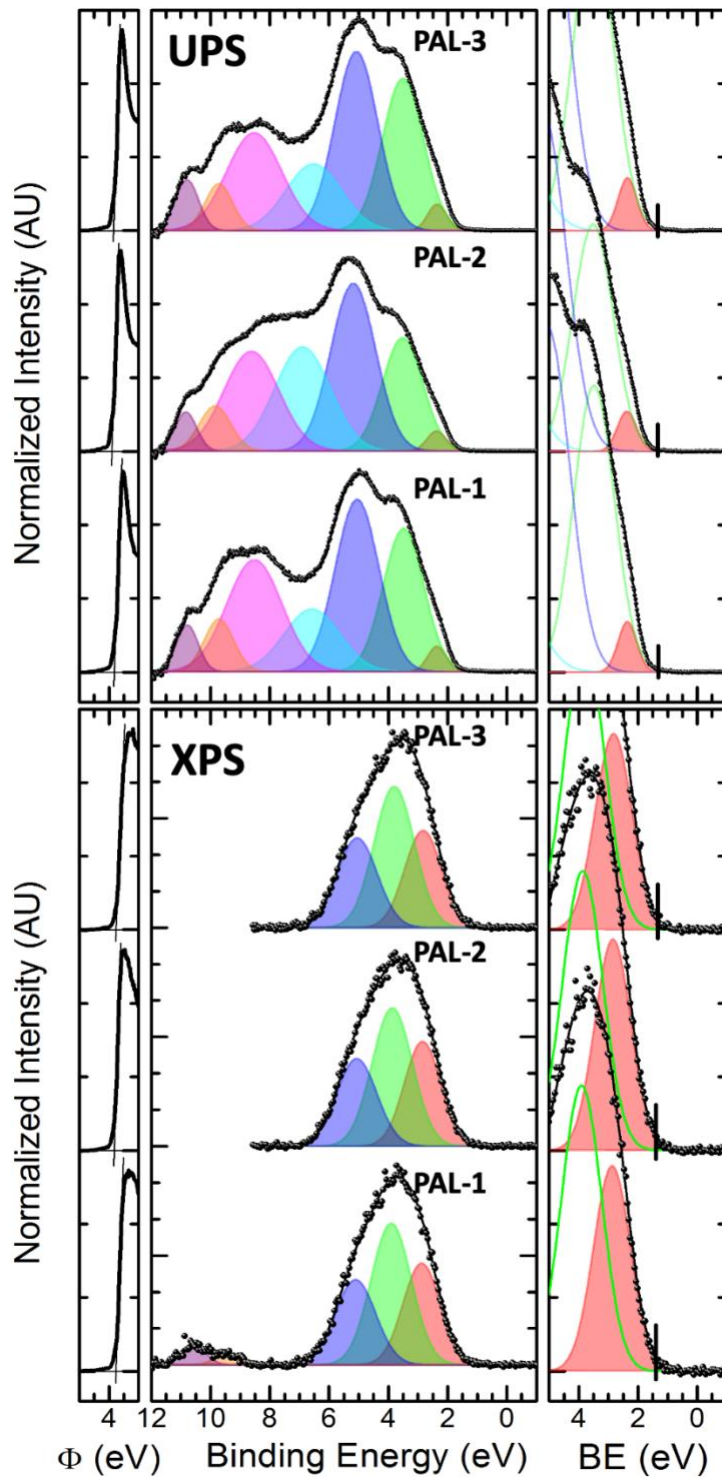


**Figure S5.** Valence band photoemission spectra for three identical perovskite active layer (PAL) thin films, as described in the text. The UPS data was acquired with He I excitation (21.22 eV) and was corrected for the additional photoemission arising from He I  $\beta$  and He I  $\gamma$  satellites in the excitation source. After removal of satellite photoemission features a polynomial fitting function was used to remove the residual background due to secondary

electron photoemission. The VBM region was fit with a minimum number of Gaussian peaks and the VB onset (VBM) energy (vertical line in each plot) estimated from the intersection of the energy axis and photoemission intensity at 3.5 sigma away from the mean of the highest KE valence band peak. Valence band XPS spectra were acquitted at low X-ray fluence ( ALK alpha source operated at 1 mA, 15 kV: 15 W) and the high KE valence band photoemission data treated in the same way as the UPS data. It can be seen that there is good agreement in estimates of VBM energy even though the sampling depths for the UPS experiment (less than ca. 10 nm) and the XPS experiment (approximately 3x that sampling depth seen for UPS data) are different.

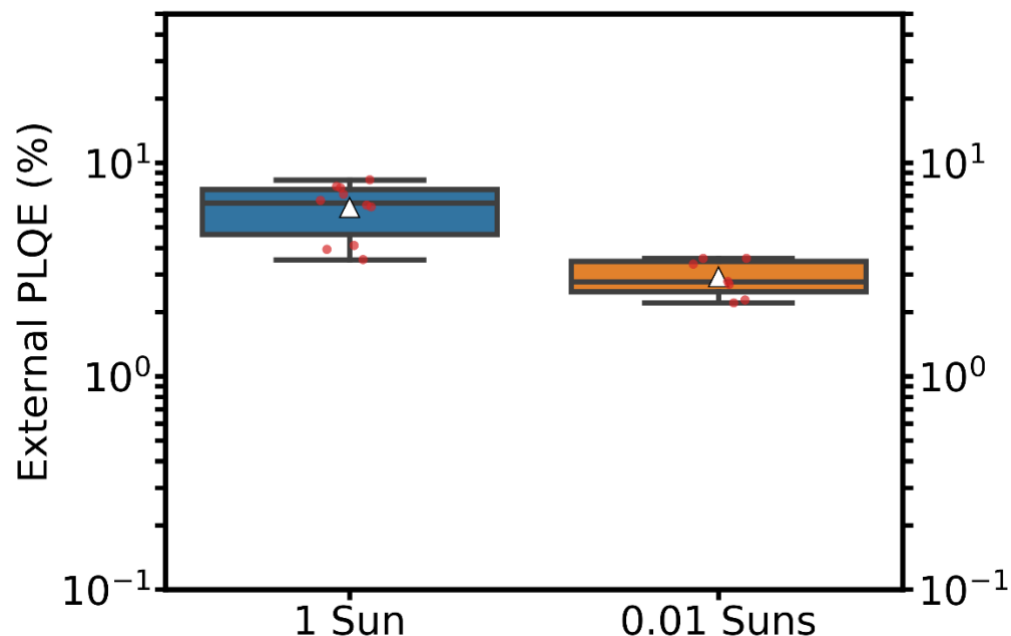
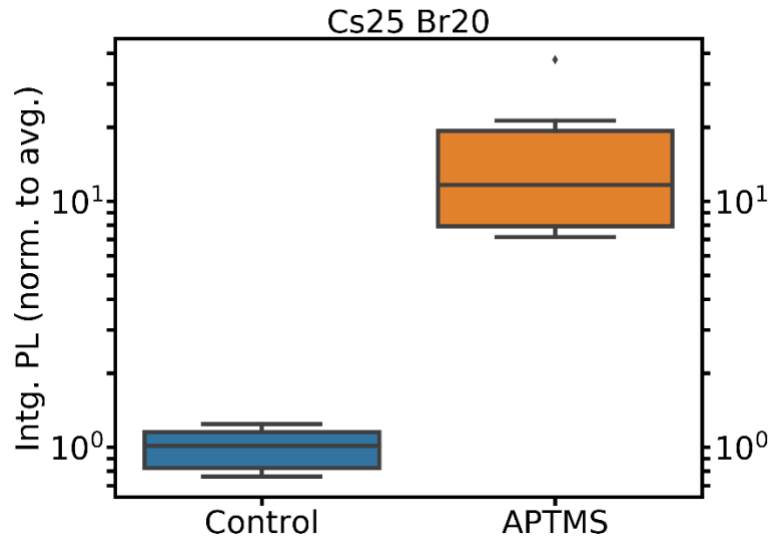
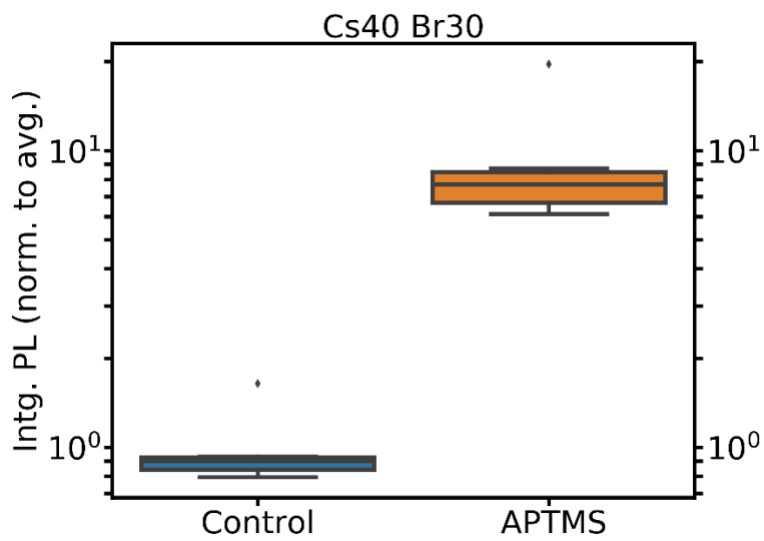


Figure S6. External PLQE for APTMS passivated Cs<sub>17</sub>Br<sub>15</sub> thin films showing high PLQE even at 0.01 Sun intensity. For a collection of samples with highest PLQE of 8.3% (n=10) at ~1 Sun intensity (60 mW/cm<sup>2</sup>), we measure a highest PLQE of 3.6% (n=7) at ~0.01 Sun intensity (0.7 mW/cm<sup>2</sup>). The boxes show the quartiles of the data and the whiskers extend to capture the rest of the distribution. The white triangle denotes the average of the distribution. The red scatter points are the individual data points.



**Figure S7. Integrated PL intensity normalized to the average for control and APTMS passivated Cs25Br20 films.**



**Figure S8. Integrated PL intensity normalized to the average for control and APTMS passivated Cs40Br30 films.**

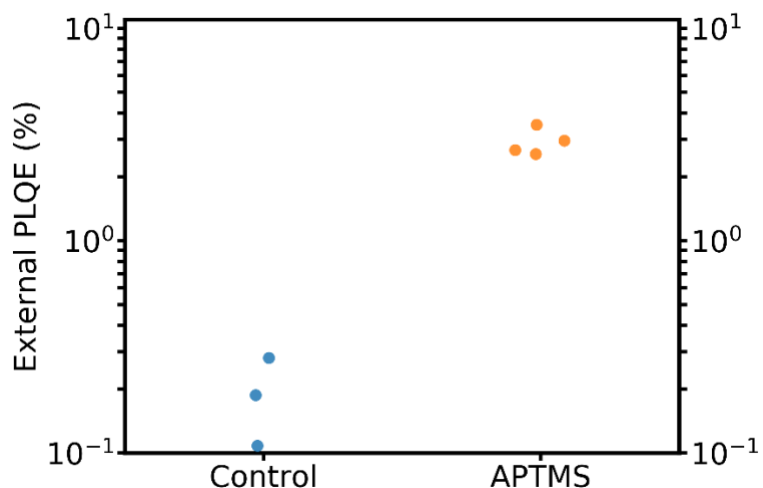


**Figure S9. External PLQE for control and APTMS passivated Cs<sub>25</sub>Br<sub>20</sub> ( $E_g \sim 1.7$  eV) thin films measured at  $\sim 1$  Sun intensity ( $60 \text{ mW/cm}^2$ ). The highest PLQE at  $\sim 1$  Sun intensity increases by 10X from 0.28% for control films to 3.5% for APTMS passivated Cs<sub>25</sub>Br<sub>20</sub> films.**

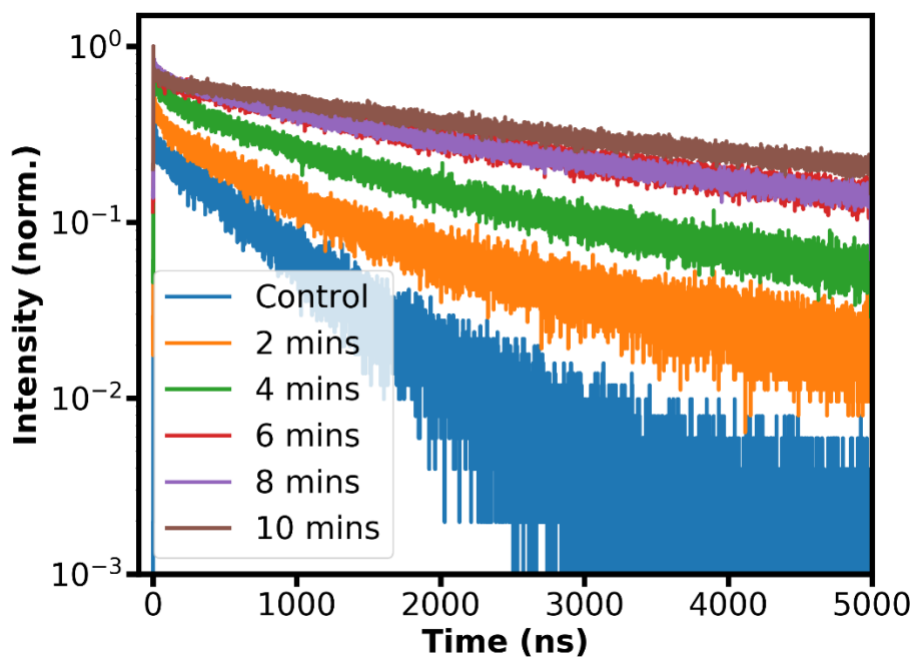


**Figure S10. Normalized time-resolved PL intensity for control and APTMS passivated Cs<sub>17</sub>Br<sub>15</sub> films as a function of exposure time to APTMS.**

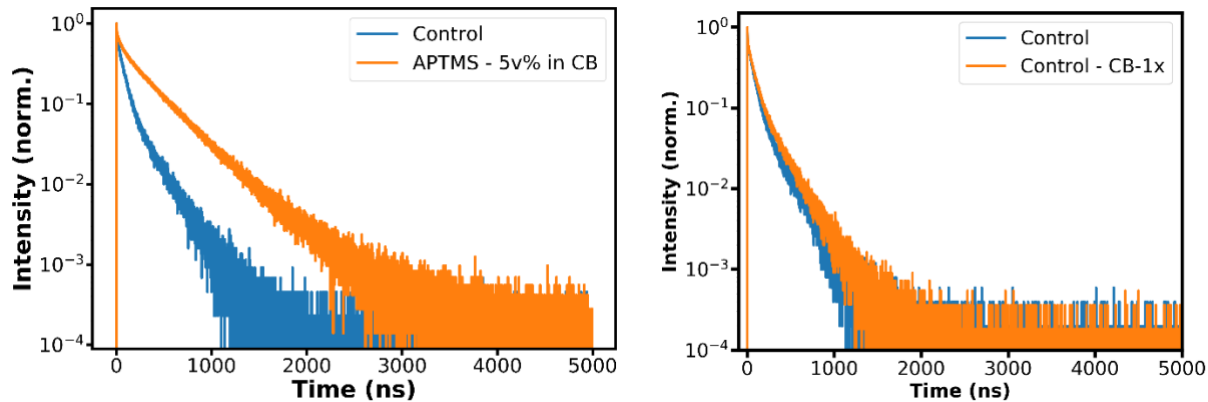


**Figure S11. Normalized time-resolved PL intensity for (left) control and APTMS passivated Cs<sub>17</sub>Br<sub>15</sub> films by spincoating 5v% APTMS in CB, and for (right) control and only CB spincoated Cs<sub>17</sub>Br<sub>15</sub> films. Together these figures demonstrate that the APTMS is acting as a surface modifier.**

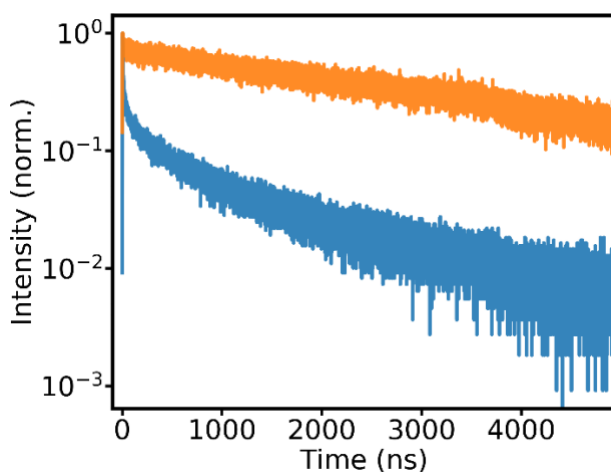


**Figure S12. Time-resolved PL decay for CH<sub>3</sub>NH<sub>3</sub>PbI<sub>3</sub> (MAPI) thin films (made acc to ref.<sup>25</sup>) before and after silane treatment. The average PL lifetime improves from 148 ns (control) to 3.4  $\mu$ s after silane passivation.**

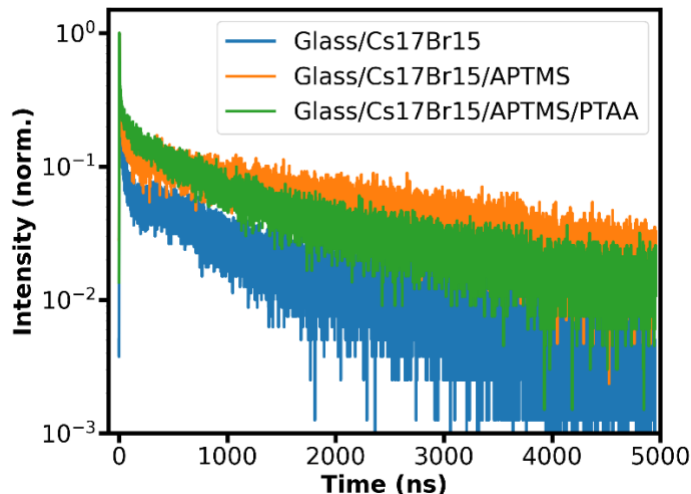


**Figure S13. Normalized time-resolved PL decay for control, APTMS passivated and PTAA treated Cs17Br15 films demonstrating PL improvements post APTMS passivation are retained after transport layer (PTAA) deposition.**

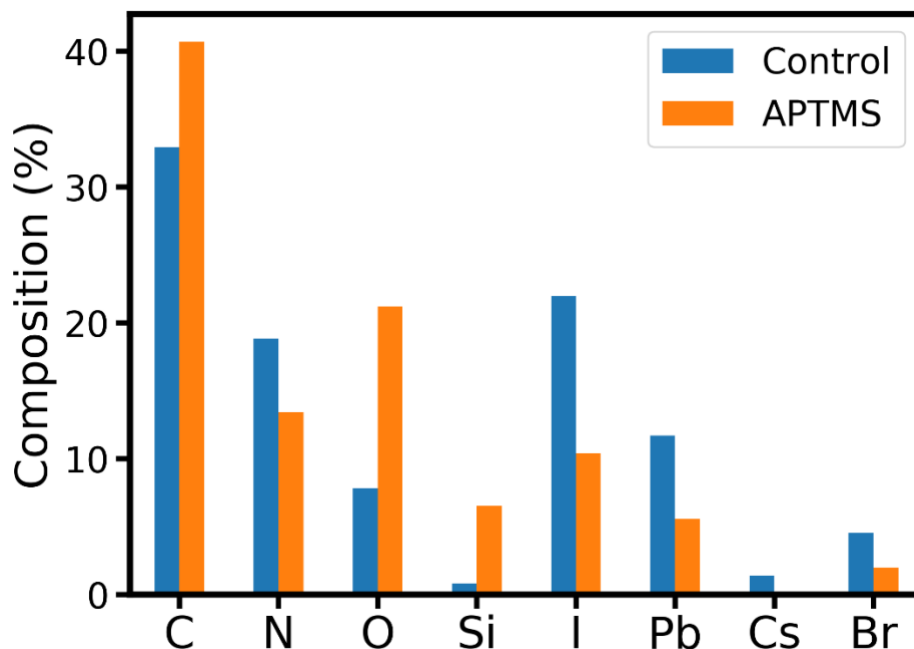


**Figure S14. Composition determined from XPS survey spectra for control and APTMS passivated Cs17Br15 films. The increase in Si and O concentration demonstrates the presence of APTMS on the perovskite surface. The O 1s signal observed in control samples is adventitious O likely adsorbed on the surface.**

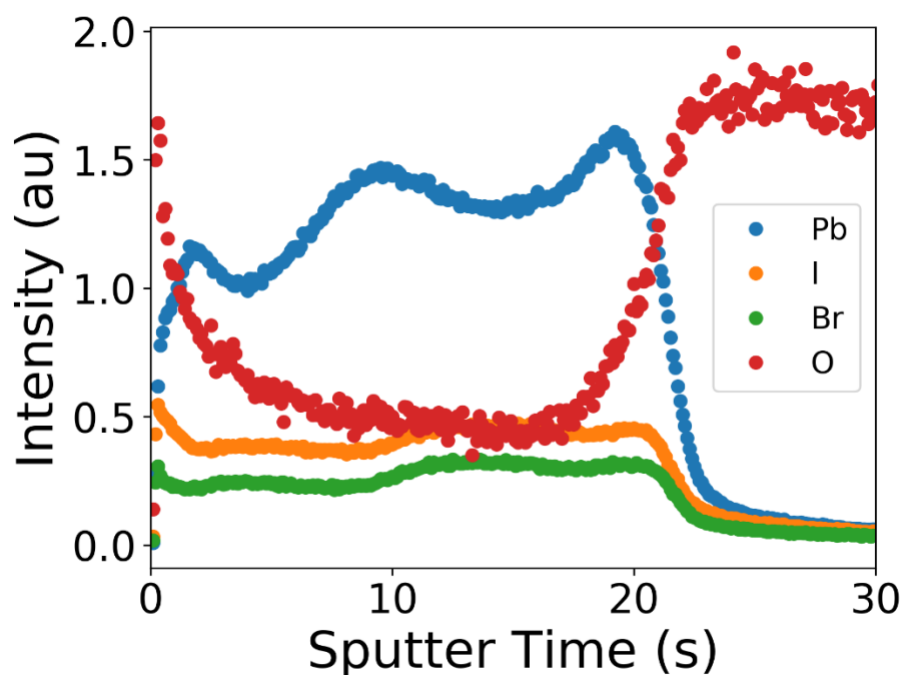


**Figure S15. Elemental depth profile of silane passivated Cs<sub>17</sub>Br<sub>15</sub> films acquired using GDOES (glow discharge optical emission spectroscopy) showing decreasing O signal and increasing perovskite signal (Pb, I, Br) as a function of depth (sputtering time). As the perovskite is completely etched away as determined from the decreasing Pb, I, Br signals, we see the O signal rise again, now from the glass substrate underneath the perovskite. Si signal intensity is much weaker compared to O (and other elements such as Pb, I, Br) and therefore, it wasn't included in the plot for clarity and brevity.**

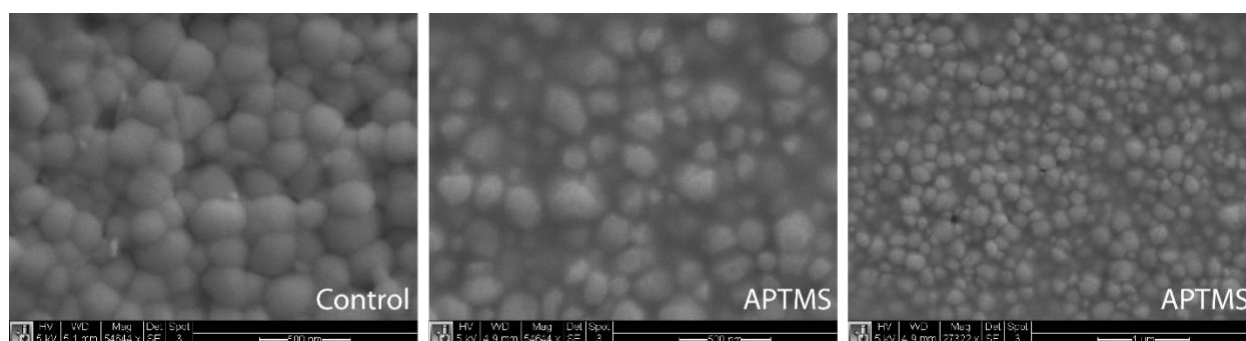


**Figure S16. SEM morphology of control and APTMS modified Cs<sub>17</sub>Br<sub>15</sub> thin films (on ITO) showing no morphology change of the underlying perovskite after APTMS modification.**

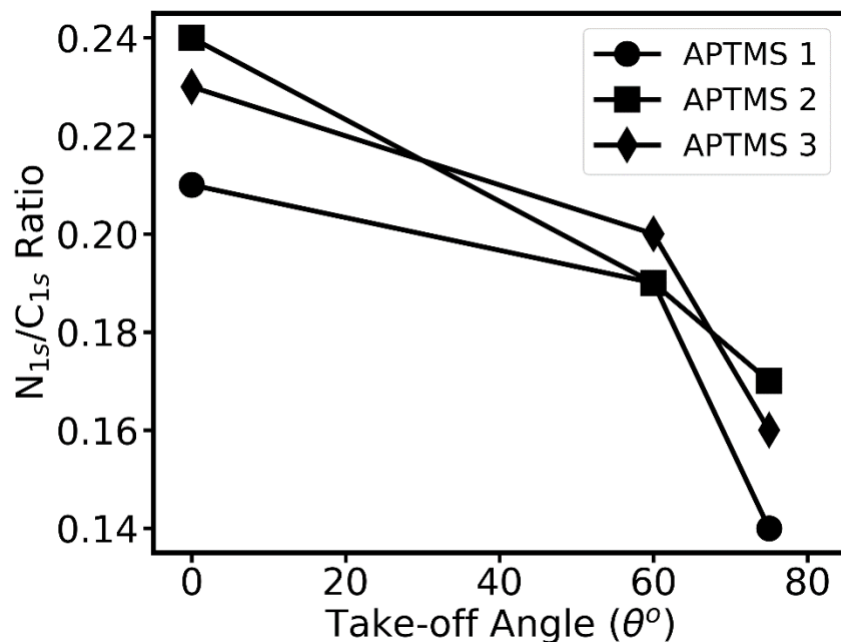


Figure S17. Angle-resolved XPS for APTMS passivated film. N 1s/C 1s signal as a function of photo-electron take-off angle. The decreasing N 1s/C 1s signal with increasing take-off angle (more surface sensitivity) indicates that the terminal amine in APTMS is oriented towards the perovskite surface.

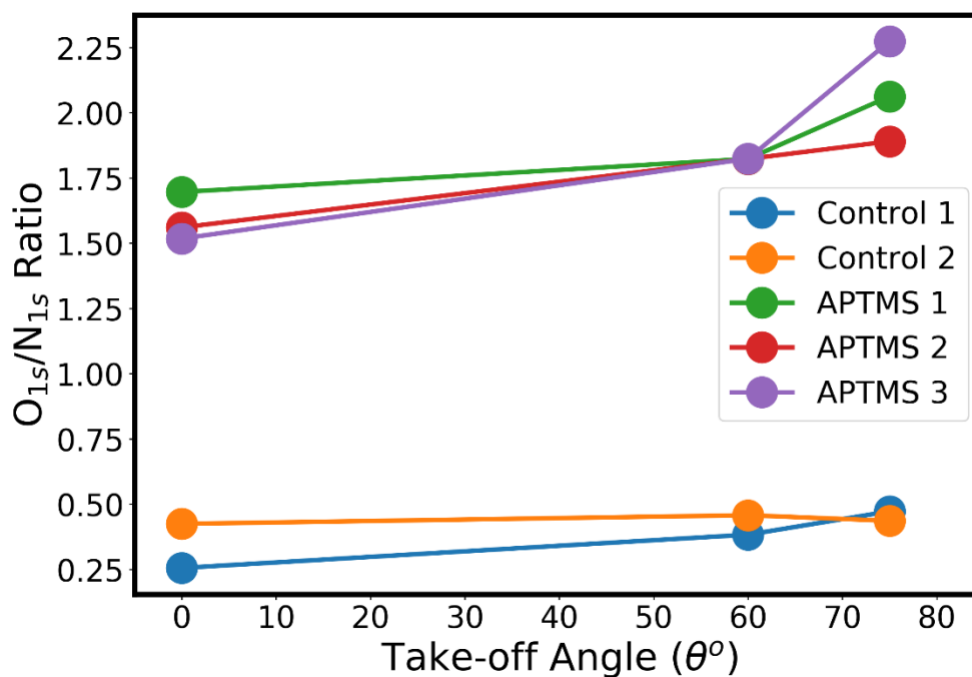


Figure S18. O 1s/N 1s signal ratio for control and APTMS passivated Cs17Br15 thin films as a function of photo-electron take-off angle. The APTMS samples show an increasing

trend of O 1s/N 1s ratio with increasing surface sensitivity, indicating that the methoxy groups on average are oriented away from the perovskite surface. The control samples show no distinct trend. The O 1s signal observed in control samples is adventitious O likely adsorbed on the surface.

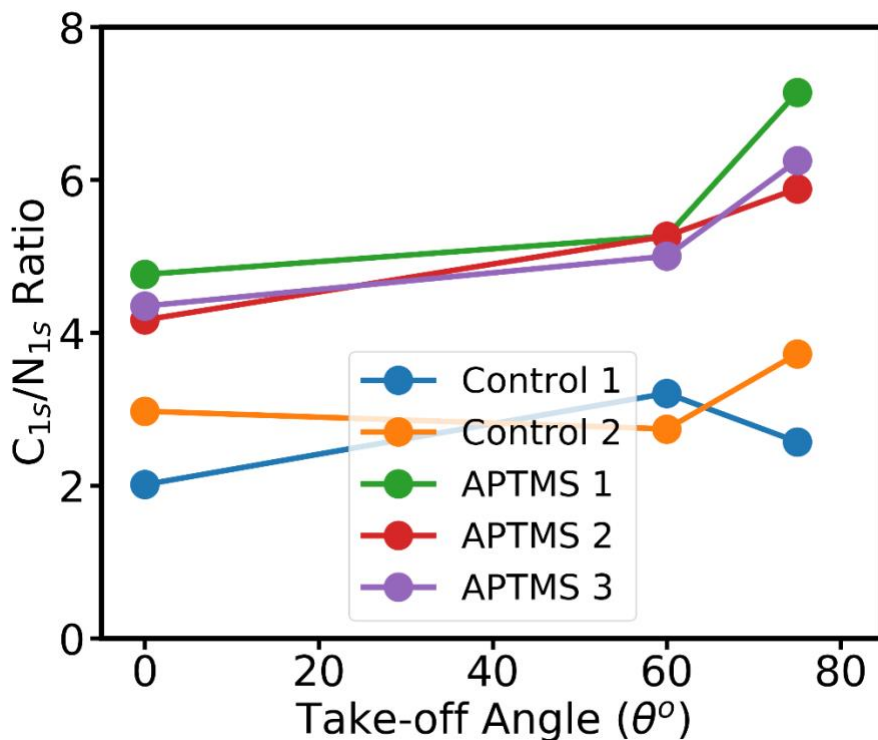


Figure S19. C 1s/N 1s signal ratio for control and APTMS passivated Cs<sub>17</sub>Br<sub>15</sub> thin films as a function of photo-electron take-off angle. The APTMS samples show a distinct trend with increasing C 1s/N 1s ratio with increasing surface sensitivity, indicating that the terminal amine is oriented towards the perovskite surface. The control samples show no distinct trend.

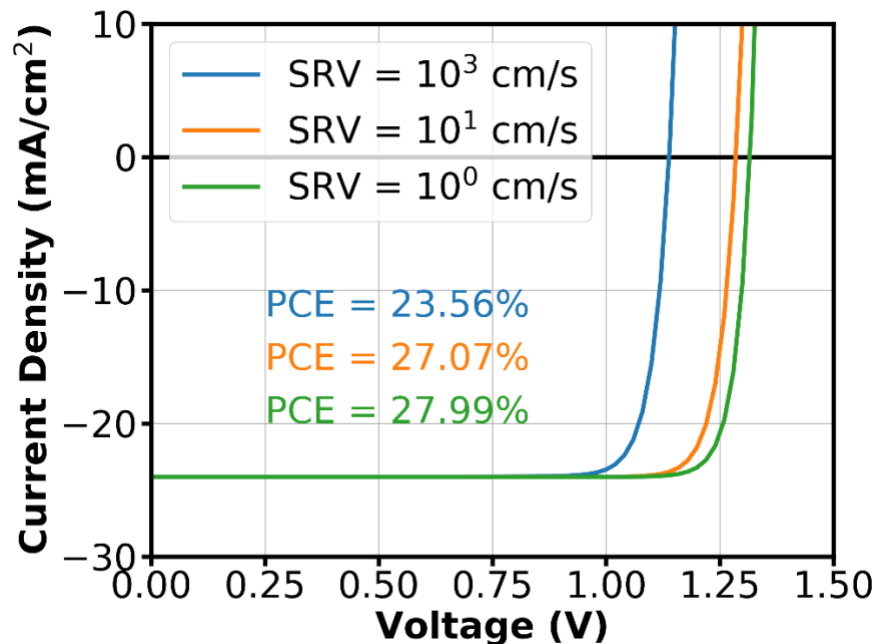


Figure S20. Simulated J-V curve (using SCAPS<sup>57</sup>) for metal/HTL/Cs17Br15/ETL/metal geometry with the same SRV at the perovskite/HTL and perovskite/ETL interface and perfect interface energy alignment of the transport layers with Cs17Br15 (HTL – hole transport layer, ETL – electron transport layer).

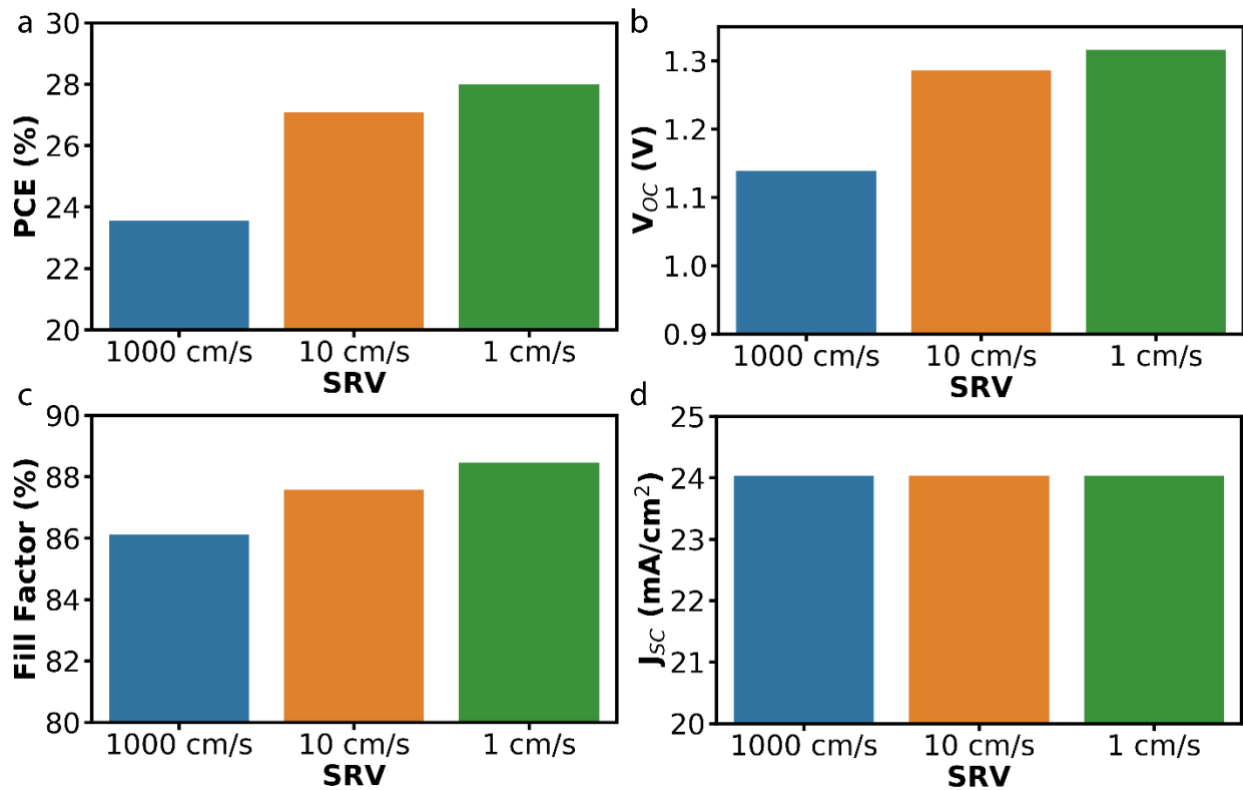


Figure S21. (a) Power conversion efficiency (PCE), (b) open circuit voltage ( $V_{OC}$ ), (c) fill factor and (d) short circuit current density ( $J_{SC}$ ) for J-V SCAPS<sup>11</sup> simulations shown in Figure 4 in the main manuscript.

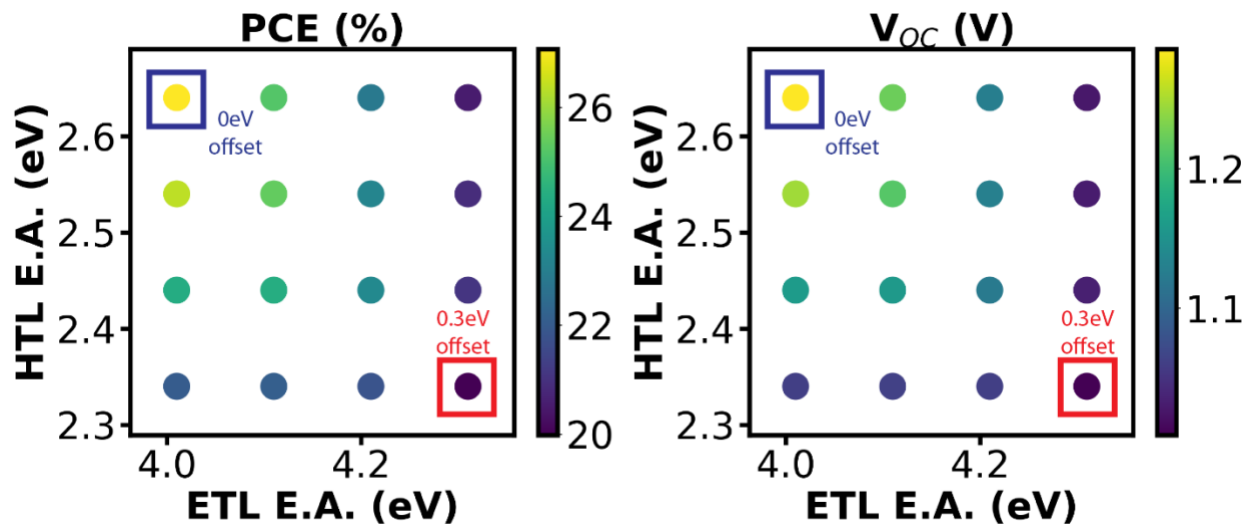


Figure S22. PCE and  $V_{OC}$  as a function of different transport layer energy alignments (SRV1=SRV2 = 10 cm/s). Increasing energy offsets decreases the highest achievable PCE and  $V_{OC}$ . The simulations were performed using SCAPS.<sup>11</sup>

## References

- (1) Saliba, M.; Matsui, T.; Seo, J. Y.; Domanski, K.; Correa-Baena, J. P.; Nazeeruddin, M. K.; Zakeeruddin, S. M.; Tress, W.; Abate, A.; Hagfeldt, A.; et al. Cesium-Containing Triple Cation Perovskite Solar Cells: Improved Stability, Reproducibility and High Efficiency. *Energy Environ. Sci.* **2016**, *9* (6), 1989–1997. <https://doi.org/10.1039/c5ee03874j>.
- (2) Ross, R. T. Some Thermodynamics of Photochemical Systems. *J. Chem. Phys.* **1967**, *46* (12), 4590–4593. <https://doi.org/10.1063/1.1840606>.
- (3) de Mello, J. C.; Wittmann, H. F.; Friend, R. H. An Improved Experimental Determination of External Photoluminescence Quantum Efficiency. *Adv. Mater.* **1997**, *9* (3), 230–232. <https://doi.org/10.1002/adma.19970090308>.
- (4) DeQuilettes, D. W.; Vorpahl, S. M.; Stranks, S. D.; Nagaoka, H.; Eperon, G. E.; Ziffer, M. E.; Snaith, H. J.; Ginger, D. S. Impact of Microstructure on Local Carrier Lifetime in Perovskite Solar Cells. *Science (80-. )*. **2015**, *348* (6235), 683–686. <https://doi.org/10.1126/science.aaa5333>.
- (5) deQuilettes, D. W.; Koch, S.; Burke, S.; Paranj, R.; Shropshire, A. J.; Ziffer, M. E.; Ginger, D. S. Photoluminescence Lifetimes Exceeding 8 Ms and Quantum Yields Exceeding 30% in Hybrid Perovskite Thin Films by Ligand Passivation. *ACS Energy Lett.* **2016**, *1* (2), 438–444. <https://doi.org/10.1021/acsenergylett.6b00236>.
- (6) DeQuilettes, D. W.; Jariwala, S.; Burke, S.; Ziffer, M. E.; Wang, J. T. W.; Snaith, H. J.; Ginger, D. S. Tracking Photoexcited Carriers in Hybrid Perovskite Semiconductors: Trap-Dominated Spatial Heterogeneity and Diffusion. *ACS Nano* **2017**, *11* (11), 11488–11496. <https://doi.org/10.1021/acsnano.7b06242>.
- (7) Jariwala, S.; Sun, H.; Adhyaksa, G. W. P.; Lof, A.; Muscarella, L. A.; Ehrler, B.; Garnett, E. C.; Ginger, D. S. Local Crystal Misorientation Influences Non-Radiative Recombination in Halide Perovskites. *Joule* **2019**, *3* (12), 3048–3060. <https://doi.org/10.1016/j.joule.2019.09.001>.
- (8) Munechika, K.; Chen, Y.; Tillack, A. F.; Kulkarni, A. P.; Plante, I. J. La; Munro, A. M.; Ginger, D. S. Spectral Control of Plasmonic Emission Enhancement from Quantum Dots near Single Silver Nanoprisms. *Nano Lett.* **2010**, *10* (7), 2598–2603. <https://doi.org/10.1021/nl101281a>.
- (9) Sproul, A. B. Dimensionless Solution of the Equation Describing the Effect of Surface Recombination on Carrier Decay in Semiconductors Contactless Determination of Current–Voltage Characteristics and Minority-Carrier Lifetimes in Semiconductors from Quasi-Steady-State. *J. Appl. Phys.* **1994**, *76* (10), 2851–2282. <https://doi.org/10.1063/1.361459>.
- (10) Rehman, W.; McMeekin, D. P.; Patel, J. B.; Milot, R. L.; Johnston, M. B.; Snaith, H. J.; Herz, L. M. Photovoltaic Mixed-Cation Lead Mixed-Halide Perovskites: Links between Crystallinity, Photo-Stability and Electronic Properties. *Energy Environ. Sci.* **2017**, *10* (1), 361–369. <https://doi.org/10.1039/c6ee03014a>.
- (11) Burgelman, M.; Nollet, P.; Degraeve, S. Modelling Polycrystalline Semiconductor Solar Cells. *Thin Solid Films* **2000**, *361*, 527–532. [https://doi.org/10.1016/S0040-6090\(99\)00825-1](https://doi.org/10.1016/S0040-6090(99)00825-1).
- (12) Burgelman, M.; Decock, K.; Khelifi, S.; Abass, A. Advanced Electrical Simulation of Thin Film Solar Cells. In *Thin Solid Films*; Elsevier, 2013; Vol. 535, pp 296–301. <https://doi.org/10.1016/j.tsf.2012.10.032>.

- (13) deQuilettes, D. W.; Koch, S.; Burke, S.; Paranj, R.; Shropshire, A. J.; Ziffer, M. E.; Ginger, D. S. Photoluminescence Lifetimes Exceeding 8 Ms and Quantum Yields Exceeding 30% in Hybrid Perovskite Thin Films by Ligand Passivation. *ACS Energy Lett.* **2016**, *1* (2), 438–444. <https://doi.org/10.1021/acsenergylett.6b00236>.
- (14) Wang, J.; Fu, W.; Jariwala, S.; Sinha, I.; Jen, A. K.-Y.; Ginger, D. S. Reducing Surface Recombination Velocities at the Electrical Contacts Will Improve Perovskite Photovoltaics. *ACS Energy Lett.* **2018**, *4*, 222–227. <https://doi.org/10.1021/acsenergylett.8b02058>.
- (15) Caswell, T. A.; Droettboom, M.; Lee, A.; Hunter, J.; Andrade, E. S. de; Firing, E.; Hoffmann, T.; Klymak, J.; Stansby, D.; Varoquaux, N.; et al. Matplotlib/Matplotlib: REL: V3.3.2. **2020**. <https://doi.org/10.5281/ZENODO.4030140>.
- (16) Reback, J.; McKinney, W.; Bossche, J. Van den; jbrockmendel; Augspurger, T.; Cloud, P.; gyoung; Sinhrks; Klein, A.; Tratner, J.; et al. Pandas-Dev/Pandas: V0.25.3. **2019**. <https://doi.org/10.5281/ZENODO.3524604>.
- (17) Waskom, M.; Botvinnik, O.; O’Kane, D.; Hobson, P.; Ostblom, J.; Lukauskas, S.; Gemperline, D. C.; Augspurger, T.; Halchenko, Y.; Cole, J. B.; et al. Mwaskom/Seaborn: V0.9.0 (July 2018). **2018**. <https://doi.org/10.5281/ZENODO.1313201>.
- (18) Perkins, C. L.; Hasoon, F. S. Surfactant-Assisted Growth of CdS Thin Films for Photovoltaic Applications. *J. Vac. Sci. Technol. A Vacuum, Surfaces, Film.* **2006**, *24* (3), 497–504. <https://doi.org/10.1116/1.2194929>.
- (19) Shallcross, R. C.; Olthof, S.; Meerholz, K.; Armstrong, N. R. Impact of Titanium Dioxide Surface Defects on the Interfacial Composition and Energetics of Evaporated Perovskite Active Layers. *ACS Appl. Mater. Interfaces* **2019**, *11* (35), 32500–32508. <https://doi.org/10.1021/acsami.9b09935>.
- (20) Tao, S.; Schmidt, I.; Brocks, G.; Jiang, J.; Tranca, I.; Meerholz, K.; Olthof, S. Absolute Energy Level Positions in Tin- and Lead-Based Halide Perovskites. *Nat. Commun.* **2019**, *10* (1), 1–10. <https://doi.org/10.1038/s41467-019-10468-7>.
- (21) Feldmann, S.; Macpherson, S.; Senanayak, S. P.; Abdi-Jalebi, M.; Rivett, J. P. H.; Nan, G.; Tainter, G. D.; Doherty, T. A. S.; Frohna, K.; Ringe, E.; et al. Photodoping through Local Charge Carrier Accumulation in Alloyed Hybrid Perovskites for Highly Efficient Luminescence. *Nat. Photonics* **2020**, *14* (2), 123–128. <https://doi.org/10.1038/s41566-019-0546-8>.
- (22) Shallcross, R. C.; Zheng, Y.; Saavedra, S. S.; Armstrong, N. R. Determining Band-Edge Energies and Morphology-Dependent Stability of Formamidinium Lead Perovskite Films Using Spectroelectrochemistry and Photoelectron Spectroscopy. *J. Am. Chem. Soc.* **2017**, *139* (13), 4866–4878. <https://doi.org/10.1021/jacs.7b00516>.
- (23) Chen, P.; Bai, Y.; Wang, S.; Lyu, M.; Yun, J.-H.; Wang, L. In Situ Growth of 2D Perovskite Capping Layer for Stable and Efficient Perovskite Solar Cells. *Adv. Funct. Mater.* **2018**, *28* (17), 1706923. <https://doi.org/10.1002/adfm.201706923>.
- (24) Acres, R. G.; Ellis, A. V.; Alvino, J.; Lenahan, C. E.; Khodakov, D. A.; Metha, G. F.; Andersson, G. G. Molecular Structure of 3-Aminopropyltriethoxysilane Layers Formed on Silanol-Terminated Silicon Surfaces. *J. Phys. Chem. C* **2012**, *116* (10), 6289–6297. <https://doi.org/10.1021/jp212056s>.
- (25) Zhang, W.; Saliba, M.; Moore, D. T.; Pathak, S. K.; Hörantner, M. T.; Stergiopoulos, T.; Stranks, S. D.; Eperon, G. E.; Alexander-Webber, J. A.; Abate, A.; et al. Ultrasoft Organic-Inorganic Perovskite Thin-Film Formation and Crystallization for Efficient

Planar Heterojunction Solar Cells. *Nat. Commun.* **2015**, *6*.  
<https://doi.org/10.1038/ncomms7142>.

# Curriculum Vitae

# SARTHAK JARIWALA

## EDUCATION

- Ph.D., Materials Science and Engineering** (Sep'16 – Jun'21)  
*University of Washington, Seattle*
- Visiting Student & Researcher** (Sep'15 - May'16)  
*Massachusetts Institute of Technology, Cambridge*
- B.Tech., Nanotechnology** (Aug'12 - May'16)  
*SRM Institute of Science and Technology, India*

## FELLOWSHIPS, SCHOLARSHIPS & AWARDS (*selected*)

- **Best Oral Presentation Award, NanoGE Fall Meeting - 2020**
- **Data Science Accelerator Award – 2018-2019**
- **Data Intensive Research Enabling Clean Technologies (DIRECT) Fellow – 2017-2018**
- **UW Clean Energy Institute Graduate Fellow, University of Washington – 2017-2018**
- **UW Clean Energy Institute Travel Grant – 2019, 2018, 2017**
- **John A. Schwager Endowed Fund for Excellence in Materials Science & Engineering, 2016**
- **SRM Semester Abroad Scholarship** for an academic year at MIT – May 2015
- **SRM University Merit Scholarship** for outstanding academic achievements – 2013-14 and 2014-15

## RESEARCH EXPERIENCE

### Graduate Research Assistant

*Ginger group, University of Washington, Seattle*  
(Sep'16 – Jun'21)

- Elucidated **local structure-property relationships** in organic-inorganic **halide perovskite solar cells** using **expertise in structural, chemical and optical characterization**.
- Investigated **photo-physics** and **bulk, surface and interface defect chemistry** in halide perovskite solar cells using **expertise in surface/interface characterization**.
- **Demonstrated methods to control the effects of defects** on radiative efficiency and solar cell performance using various **surface passivation and chemical treatment** schemes.

- **Led process development** for halide perovskite **thin film devices** to achieve record photoluminescence quantum efficiency and quasi-fermi level splitting - *97% of the theoretical limit*.
- **Coordinated multi-institution collaborations** to investigate and minimize the surface and interface recombination at **transport layer/perovskite interfaces**.
- **Developed a robust code base** in Python for interacting with various lab instruments to improve and **automate data acquisition as well as analysis** of outcoming data.
- **Advised and led experimental efforts of junior researchers**; trained them in various fabrication and characterization techniques.
- **Oversaw and managed the transition of a large internal LabView code base to Python** with interactive and intuitive user control.
- **Authored 9 peer-reviewed articles** in leading materials and energy focused journals and **presented at 7 international conferences**.

#### **Undergraduate Research Assistant**

*Baldo group, Massachusetts Institute of Technology*

*(Oct'15 - June'16)*

- **Successfully engineered and fabricated** novel hybrid organic-inorganic photovoltaic cells using *silicon and tetracene* with the help of deposition processes such as ALD and PVD. Performed **optical, electrical and magnetic characterization**.
- Used Nano-imprint lithography, PVD, CVD and RCA clean for a variety of processes ranging from depositing antireflective coatings on Si solar cells to making micro-fluidic devices to fabricating nano-cantilevers.

#### **SKILLS & COMPETENCES**

**Characterisation techniques:** SEM, EDX, EBSD, AFM, XRD, XPS, TOF-SIMS, Confocal & Hyperspectral Microscopy, Time Correlated Single Photon Counting Measurements, Ultrafast PL Spectroscopy, UV-Vis, FTIR, Glow Discharge Optical Emission Spectroscopy, Solar Cell Characterization.

**Deposition techniques:** Spin coating, ALD, PVD, CVD.

**Substrate patterning** using Contact and Projection Lithography and etching using Dry and Wet Etching techniques and general **wafer cleaning** protocols- RCA clean, Piranha clean. **Nanomaterial synthesis** using Hydrothermal Synthesis, Sol-gel Combustion method.

**Software:** Proficient in *Python, MATLAB, SCPAPS, SAM*.

## PUBLICATIONS

\* Undergraduate students mentored, ^ Graduate students mentored

- David A Valverde-Chávez, Esteban Rojas-Gatjens, Jacob Williamson, **Sarthak Jariwala**, Yangwei Shi<sup>^</sup>, *et al.* "[Nonlinear photocarrier dynamics and the role of shallow traps in mixed-halide mixed-cation hybrid perovskites](#)" **J. Mater. Chem. C. (2021)**. (*accepted*)
- **Sarthak Jariwala**, Sven Burke\*, Sean Dunfield, Clayton Shallcross, Margherita Taddei<sup>^</sup>, *et al.* "[Approaching the limits of optoelectronic performance in mixed cation mixed halide perovskites by controlling surface recombination](#)" **Chemistry of Materials (2021)**. (*accepted*)
- Yaeun Han, Sungbin Park, Jian Wang, **Sarthak Jariwala**, *et al.* "[Controlling Spatial Crystallization Uniformity and Phase Orientation of Quasi-2D Perovskite-Based Light-Emitting Diodes Using Lewis Bases](#)" **Advanced Materials Interfaces 7 (3), 1901860 (2020)**.
- **Sarthak Jariwala**, Hongyu Sun, Gede WP Adhyaksa, Andries Lof, Erik C Garnett, David S Ginger "[Local crystal misorientation influences non-radiative recombination in halide perovskites](#)" **Joule 3 (12), 3048-3060 (2019)**.
  - This article in *Joule* was highlighted in UW News, Tech Xplore and other news outlets.
- Rajiv Giridharagopal, Jake T Precht, **Sarthak Jariwala**, Liam Collins, Stephen Jesse, Sergei V Kalinin, David S Ginger "[Time-Resolved Electrical Scanning Probe Microscopy of Layered Perovskites Reveals Spatial Variations in Photoinduced Ionic and Electronic Carrier Motion](#)" **ACS Nano 13 (3), 2812-2821 (2019)**.
- Jian Wang, Weifei Fu, **Sarthak Jariwala**, Irika Sinha\*, Alex K-Y Jen, David S Ginger "[Reducing surface recombination velocities at the electrical contacts will improve perovskite photovoltaics](#)" **ACS Energy Letters 4(1), 222-227 (2018)**.
- Wolf-Alexander Quitsch, Dane W deQuilettes, Oliver Pflingsten, Alexander Schmitz, Stevan Ognjanovic, **Sarthak Jariwala**, Susanne Koch, Markus Winterer, David S Ginger, Gerd Bacher

[“The role of excitation energy in photobrightening and photodegradation of halide perovskite thin films”](#) **The Journal of Physical Chemistry Letters** **9(8)**, 2062-2069 (2017).

- Dane W. deQuilettes, **Sarthak Jariwala**, Sven Burke\*, *et al.* [“Tracking photoexcited carriers in hybrid perovskite semiconductors: trap-dominated spatial heterogeneity and diffusion”](#) **ACS Nano** **11(11)**, 11488-11496 (2017).
- L. Zuo, H. Guo, D.W. deQuilettes, **Sarthak Jariwala**, *et al.* [“Polymer-modified halide perovskite films for efficient and stable planar heterojunction solar cells”](#) **Science Advances** **3(8)** (2017).

### PRESENTATIONS *(selected)*

**Sarthak Jariwala**, Sven Burke, Sean Dunfield, Clayton Shallcross, Margherita Taddei, Jian Wang, Giles E Eperon, Neal R Armstrong, Joseph J Berry, David S Ginger. *Oral Presentation* “Approaching the limits of optoelectronic performance in mixed cation mixed halide perovskites by controlling surface recombination” **Materials Research Society (MRS) Fall Meeting (November 2020)**.

**Sarthak Jariwala**, Sven Burke, Sean Dunfield, Clayton Shallcross, Margherita Taddei, Jian Wang, Giles E Eperon, Neal R Armstrong, Joseph J Berry, David S Ginger. *Oral Presentation* “Approaching the limits of optoelectronic performance in mixed cation mixed halide perovskites by controlling surface recombination” **NanoGE Fall Meeting (October 2020)**.

*Awarded the Best Oral Presentation Award.*

**Sarthak Jariwala**, Hongyu Sun, Gede WP Adhyaksa, Andries Lof, Erik C Garnett, David S Ginger. *Oral Presentation* “Local crystal misorientation influences non-radiative recombination in halide perovskites” **NanoGE International Conference on Perovskite Thin Film Photovoltaics and Perovskite Photonics and Optoelectronics (NIPHO 2020) Seville, Spain (February 2020)**.

**Sarthak Jariwala**, Irika Sinha, Kathryn Guye, David Ginger. *Poster Presentation* “Mapping the Inter-Diffusion of A-Site Cations in Metal Halide Perovskites” **Materials Research Society (MRS) Fall Meeting, Boston, MA (November 2018)**.

**Sarthak Jariwala**, Dane W. deQuilettes, David S Ginger. *Poster Presentation* “Direct Recombination Behavior in Highly-Emissive CH<sub>3</sub>NH<sub>3</sub>PbI<sub>3</sub> Perovskite Films” **Materials Research Society (MRS) Fall Meeting, Boston, MA (November 2017)**.

## VOLUNTEER WORK *(selected)*

- **UW GRID (Global Renewable Infrastructure Development)** - <https://sites.uw.edu/grid/>
  - Performed techno-economic analysis for designing a *solar-powered school & community library* in rural Ghana.
  - Developing remote data tracking system for monitoring the health and performance of installed solar modules and microgrids.
- **Clean Energy Institute** at University of Washington
  - Hands-on activities for K-12 students on mini solar panels and solar car races.
  - UW Engineering Discovery Days
- Contributor to volunteer run open-source scientific software – <https://github.com/SarthakJariwala>

## TEACHING EXPERIENCE

Teaching assistant for MSE junior labs (2016-2017)